**Terms and Conditions of Use of Digitised Theses from Trinity College Library Dublin**

**Copyright statement**

All material supplied by Trinity College Library is protected by copyright (under the Copyright and Related Rights Act, 2000 as amended) and other relevant Intellectual Property Rights. By accessing and using a Digitised Thesis from Trinity College Library you acknowledge that all Intellectual Property Rights in any Works supplied are the sole and exclusive property of the copyright and/or other IPR holder. Specific copyright holders may not be explicitly identified. Use of materials from other sources within a thesis should not be construed as a claim over them.

A non-exclusive, non-transferable licence is hereby granted to those using or reproducing, in whole or in part, the material for valid purposes, providing the copyright owners are acknowledged using the normal conventions. Where specific permission to use material is required, this is identified and such permission must be sought from the copyright holder or agency cited.

**Liability statement**

By using a Digitised Thesis, I accept that Trinity College Dublin bears no legal responsibility for the accuracy, legality or comprehensiveness of materials contained within the thesis, and that Trinity College Dublin accepts no liability for indirect, consequential, or incidental, damages or losses arising from use of the thesis for whatever reason. Information located in a thesis may be subject to specific use constraints, details of which may not be explicitly described. It is the responsibility of potential and actual users to be aware of such constraints and to abide by them. By making use of material from a digitised thesis, you accept these copyright and disclaimer provisions. Where it is brought to the attention of Trinity College Library that there may be a breach of copyright or other restraint, it is the policy to withdraw or take down access to a thesis while the issue is being resolved.

**Access Agreement**

By using a Digitised Thesis from Trinity College Library you are bound by the following Terms & Conditions. Please read them carefully.

I have read and I understand the following statement: All material supplied via a Digitised Thesis from Trinity College Library is protected by copyright and other intellectual property rights, and duplication or sale of all or part of any of a thesis is not permitted, except that material may be duplicated by you for your research use or for educational purposes in electronic or print form providing the copyright owners are acknowledged using the normal conventions. You must obtain permission for any other use. Electronic or print copies may not be offered, whether for sale or otherwise to anyone. This copy has been supplied on the understanding that it is copyright material and that no quotation from the thesis may be published without proper acknowledgement.

# Interface properties of $Fe_3O_4/MgO$ and surface studies of $Fe_3O_4(110)$

A thesis submitted to the University of Dublin, Trinity College,

in application for the degree of Doctor in Philosophy

by

Giuseppe Manai

Physics Department
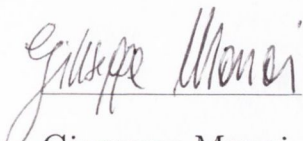
Trinity College Dublin

March 2006
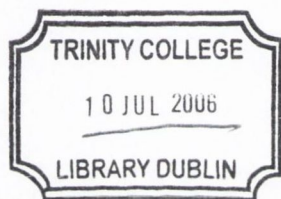
# Declaration

This thesis is submitted by the under signed for the degree of Doctor in Philosophy at the University of Dublin.

It has not been submitted as an exercise for a degree at any other university.

Apart from the advice, assistance and joint effort mantioned in the under signed and in the text, this thesis is entirely my own work.

I agree that the library may lend or copy this thesis freely on request.

Giuseppe Manai

March 2006

# Acknowledgments

Hard work is trying to thank, in only a few words, the numerous people that, in many ways, contributed to make these four years a "brilliant" experience.

I would first like to thank my supervisor, Prof. Igor V. Shvets, for the opportunity to do this Ph. D., for his help, for the enthusiasm and the support, which made this work possible.

Thanks to Dr. Shane Murphy, Dr. Guido Mariotto and Dr. Roman Kantor, who were always ready to answer to any scientific questions and help me for any sort of technical problem. Special mention goes to Dr. Sergio F. Ceballos, the first person I could understand when I set foot in Ireland, who, by traducing English into Spanish, gave me a hint of what everybody else was saying. Dr. Ken Jordan, responsible for a great contribution to this project, for all the useful discussions we had, often over lunch, coffee or in front of a good pint of porter. For the help and support he offered through the years, when he introduced me to UHV techniques, or when, with the excuse of correcting the English, I made him read and correct my thesis several times. Kevin Radican has also been of great support with his scientific but, more importantly, mechanical skills, when "Gigetta" (my moped) needed to be fixed! Particularly towards the end, he has been very supportive, while I was spending any possible minute in the lab writing, he kept asking me to go for a pint! I would also like to thank the other members of the group: Anselm, William, Victor, Alex, Bala, Jin and Yang, Ciarán, Floriano, Maina, Sumesh, Rafa, Vivienne, Dimitry, Frank, Louise, Marie, Sunil, Gops, Keith, Anthony and Barry.

Thanks also to Emma and Ronan, Greg, Eoin, James, Simon and Andy, for their great company over coffee, lunch and for all the nights out in pubs.

The group could not operate without the efforts and background support of other members of the Physics Department such as John Kelly, Mick Reilly, Ken

e Mamma, Nonna e la famiria tutta, Manai e Auneddu, pa la fozza chi m'ani daddu in chisthi anni, l'amori, la pazenzia e la fiduzia di lassammi andà, candu nemmancu eu sabbia undì era andendi!

# Summary

The research project described in this Ph. D. thesis can be divided into two parts. The first, consisting in the description of a new instrument, the low temperature tunneling device (LTTD), designed and built in order to measure the deformation of $Fe_3O_4$/MgO thin films when cooled down through the Verwey transition. In the second part, Auger electron spectroscopy (AES), low energy electron diffraction (LEED), scanning tunneling microscopy-spectroscopy (STM-STS) have been used to characterise the surface reconstruction of $Fe_3O_4$ (110) in the case of single crystal and of two thin films deposited on MgO substrate.

The first part, concentrates on the temperature dependent deformation of $Fe_3O_4$/MgO thin films due to the stress developed at the interface. Initially, a complete description of the LTTD is given. This instrument, based on the functioning of STMs, uses quantum mechanical tunneling to measure small deformations along one of the axis of the sample with a resolution of 0.25 Å. An adaptation of the cantilever bending technique was then implemented in the LTTD, in order to measure the deflection of the thin films with changing temperature. The main interest of this study was to measure the deformation of the films at the Verwey transition. This transformation consists in a structural rearrangement of the atoms at the Verwey transition temperature $T_V$, that affects the electric and magnetic properties of the crystal. It was found that, in $Fe_3O_4$ thin films, no signal was detected at $T_V$ with the LTTD. However, it was possible to formulate an hypothesis for the absence of a signal. This takes into account that the high density of antiphase boundaries (ABPs), a natural defect present in $Fe_3O_4$/MgO thin films, is responsible for the accommodation of the mismatch strain even for films thickness of 700 nm. As a consequence, the transition is inhibited in the in-plane directions and does only occur in the out-of-plane one. This explains why the Verwey transition was not detected with the cantilever bending technique

implemented in the LTTD.

The second part of the thesis describes the study of the (110) surface of magnetite. This was performed using several surface sensitive techniques, namely AES, LEED and STM-STS. The topography of a single crystal was characterised following different preparations involving annealing in oxygen or in ultra high vacuum (UHV). It was found that the surface reconstructs, generally, forming rows that run along the $[\bar{1}10]$ direction. The experiments described show that the reconstruction of the clean surface is more ordered after the annealing in oxygen and that annealing in UHV induces a breakdown of the reconstruction. Models are also proposed for the reconstruction in the different cases. Furthermore, two $Fe_3O_4/MgO(110)$ thin films of thickness equal to 50 nm were prepared using the same procedure as for the single crystal. The results obtained in these cases are very similar to those of the single crystal.

# Publications

**Oxygen-Induced p(3 x 1) Reconstruction of the W(100) Surface**

S. Murphy, G. Manai and I. V. Shvets

*Surface Science **579** (2005) 65-72*


**Towards Spin Polarised STM in Magnetite (110)**

G. Maris, L. Jdira, J. H. H. Hemrsen, S. Murphy, G. Manai, I. V. Shvets and S. Speller

*J. Phys. Soc. Jpn. **45** 3B,(2006)*


**An STS Study of Aspects of the Electronic Structure of Magnetite Surfaces**

K. Jordan and A. Cazacu and G. Manai and S. F. Ceballos and S. Murphy and I. V. Shvets"

*Submitted to Phys. Rev. B*


**Nano-Magnetic Probing on Magnetite (110)**

G. Maris, L. Jdira, J. H. H. Hemrsen, S. Murphy, G. Manai, I. V. Shvets and S. Speller

*submitted to the Intermag conference in San Diego, for the IEEE Transactions on Magnetics proceedings.*


**An ultra sensitive piezometer based on the tunnelling effect.**

G. Manai, M. Karsanova, I. V. Shvets

*in preparation*

# List of abbreviations

1D - one dimensional

2D - two dimensional

3D - three dimensional

AES - Auger electron spectroscopy

AF - antiferromagnetic

APB - antiphase boundaries

CMA - cylindrical mirror analyser

DFT - density functional theory

DOS - density of states

$e^-$-beam - electron beam

ECM - electron counting model

$E_F$ - Fermi energy

EM - electrostatic model

FWHM - full width at half maximum

GMR - giant magnetoresistance

HM - half metal

HOPG - highly oriented pyrolytic graphite

HR-XRD - high resolution X-ray diffraction

LDOS - local density of states

LEED - low energy electron diffraction

LEIS - low energy ion scattering

LSDA - local spin density approximation

LT - low temperature

LT-STM - low temperature scanning tunneling microscope

LTTD - low temperature tunneling device

MBE - molecular beam epitaxy

MR - magneto resistance

MRAM - magnetic random access memory

MTJ - magnetic tunneling junction

NEG - non evaporable getter

NMR - nuclear magnetic resonance

OFHC - oxygen free high purity copper

PTFE - poly-tetrafluoro ethylene (teflon)

PZT - lead zirconium titanate

RFA - retarding field analiser

RT - room temperature

RT-STM - room temperature scanning tunneling microscope

S/N - signal to noise ratio

SC - single crystal

SP - spin polarisation

SP-PES - spin polarised photoemission spectroscopy

SP-STM - spin polarised scanning tunneling microscopy

SPM - scanning probe microscopy

STM - scanning tunneling microscopy

STS - scanning tunneling spectroscopy

$T_C$ - Curie temperature

$T_V$ - Verwey temperature

TF - thin film

TMR - tunneling magneto resistance

TSP - titanium sublimation pump

UHV - ultra high vacuum

XPD - X-ray photoelectron diffraction

XPS - X-ray photoelectron spectroscopy

XRD - X-ray diffraction

# List of Figures

# List of Tables

# Contents

# Chapter 1

# Introduction

A large part of scientific interest is nowadays devoted to the understanding of the electronic and magnetic properties of materials at the nanoscale. This is driven by the necessity to develop new generations of electronic information processing and information storage devices. After the growth of spin valve giant magnetoresistive (GMR) devices [1, 2], which have allowed a significant increase in the storage capacity of magnetic hard drives, and the synthesis of magnetic tunneling junctions (MTJ), which have led to the development of high performance nonvolatile magnetic random access memory (MRAM), particular attention is concentrated nowadays to the fabrication and characterisation of half metals [3]. Studies on half metals constitute a very active area of research [4, 5, 6] for their potential as spin-polarised carrier source and easy integration into semiconductor devices [7, 8]. Due to its relatively high Curie temperature ($T_C$) and its electronic properties, magnetite, $Fe_3O_4$, represents one of the best candidate as a material for possible applications. In fact, $Fe_3O_4$ is predicted to be a half-metallic ferrimagnet, which means that the electrons at the Fermi level are 100% spin polarised [9, 10]. This makes magnetite a suitable material for future applications in magnetoelectronic devices [11]. It is possible that these applications will employ this material in the form of thin films. Thin films are widely used in many

applications, including microelectronics, optics, magnetic, hard and corrosion resistant coatings, micro-mechanics [12]. This technology requires control, often at the atomic level, of the film microstructure and microchemistry. Progress in this area depends upon the possibility of controlling mechanical stress, defects and stoichiometry, which is crucial for functioning and performance of these films in devices. It is clear, therefore, why a complete knowledge of the structural, electronic and magnetic properties of $Fe_3O_4$ is needed. The work presented here addresses the study of the structural properties of the $Fe_3O_4$/MgO interface and the topographic and electronic properties of the surface of $Fe_3O_4$(110). This work presents a study of the surfaces of both $Fe_3O_4$ single crystals and $Fe_3O_4$/MgO epitaxial thin films.

The first part of the thesis concentrates on the temperature dependent deformation of $Fe_3O_4$/MgO thin films due to the stress developed at the interface. Initially, a complete description of a new instrument built by the author, the low temperature tunneling device (LTTD), is given. This instrument uses quantum mechanical tunneling to measure small deformations along one of the axis of the sample with a resolution of 0.25 Å. An adaptation of the cantilever bending technique [13] was then implemented in the LTTD, in order to measure the deflection of the thin films with changing temperature. The main interest of this study was to measure the deformation of the films at the Verwey transition, a metal/insulator [1] transition that occurs in $Fe_3O_4$ at around 120 K [17]. This transformation consists of a structural rearrangement of the atoms at the Verwey transition temperature $T_V$, that affects the electric and magnetic properties of the crystal. It was found that, in $Fe_3O_4$ thin films, no signal was detected at the Verwey temperature with the LTTD. However, it was possible to formulate an hypothesis for the absence of a signal. This takes into account that the high

---

[1]Recent studies suggest that the Verwey transition is a semiconductor-semiconductor transition [14, 15, 16]. However, it will be indicated as a metal-insulator transition to avoid confusion.

density of antiphase boundaries (ABPs), a natural defect present in $Fe_3O_4/MgO$ thin films, is responsible for the accommodation of the mismatch strain even for films' thickness of 700 nm [18, 19]. As a consequence, the transition is inhibited in the in-plane directions and would only occur in the out-of-plane one. This would explain why the Verwey transition was not detected with the cantilever bending technique implemented in the LTTD.

The second part of the thesis describes the study of the (110) surface of $Fe_3O_4$. This was performed using several surface sensitive techniques such as Auger electron spectroscopy (AES), low energy electron diffraction (LEED), scanning tunneling microscopy-spectroscopy (STM-STS). The topography of a single crystal was characterised following different preparations involving annealing in oxygen or in ultra high vacuum (UHV). It was found that the surface reconstructs, in most of the cases, forming rows that run along the $[\bar{1}10]$ direction. The experiments described show that the reconstruction of the clean surface is more ordered after the annealing in oxygen and that annealing in UHV induces a breakdown of the reconstruction. Models are also proposed for the reconstruction in the different cases. Furthermore, two $Fe_3O_4/MgO(110)$ thin films of thickness equal to 50 nm were prepared using the same procedure as for the single crystal. The results obtained in these cases are very similar to those of the single crystal.

# Chapter 2

# Magnetite

## 2.1 Introduction

Magnetite, $Fe_3O_4$, is the only naturally occurring mineral with distinctly obvious magnetic properties. Only a few other minerals have any detectable magnetism [20]. Mainly because of this peculiar property, it has been studied extensively throughout history and still attracts a lot of interest from the scientific community. Today, it is of high technological relevance and finds a range of applications such as in microwave resonant circuits, in computer memory cores and in high density magnetic recording media. Magnetite is believed to be half metallic (HM) [9, 10], which means that the electron density of states shows only one spin-polarised sub-band at the Fermi energy. It is also a ferrimagnet, meaning that the crystallographic planes are antiferromagnetically arranged, but there is a different amount of spins in each plane, giving rise to a sizeable magnetic moment. HM are studied for the possibility of future applications as spin sources in spintronic devices in magnetic storage of information [1, 11], magnetic sensors applications [8] as well as in quantum computing [21], where the spin of the electron would represent a *qubit* of information. The studies in this field have led to the synthesis of high quality $Fe_3O_4$ crystals in different forms, such as thin films

supported on different substrates, particularly MgO [22, 23, 24, 25] or MgAl$_2$O$_4$ [26, 24, 27], or in the form of nanoparticles and nanoclusters [28, 29] and, recently, to the growth of Fe$_3$O$_4$ single crystal nanotubes [30]. In these different forms, Fe$_3$O$_4$ often shows new magnetic, electric and structural properties which are studied for possible future applications [31, 32, 33, 34].

## 2.2   The Crystallographic Structure of Fe$_3$O$_4$

Magnetite belongs to the iron oxide family and has chemical formula Fe$_3$O$_4$. Other iron oxides are haematite ($\alpha$-Fe$_2$O$_3$), maghemite ($\gamma$-Fe$_2$O$_3$) and wüstite (FeO). The different properties of these oxides are shown in table 2.1.

Since the early decades of the 20th century, with the X-ray diffraction (XRD) measurements performed by Bragg [35], Fe$_3$O$_4$ is known to crystallize in the inverse spinel structure. This consists of a cubic close packing of oxygen anions arranged in a face-centered lattice. Two kinds of interstices are available for the metal cations: tetrahedral, conventionally indicated as A-type, and octahedral, conventionally indicated as B-type. The unit cell of Fe$_3$O$_4$ is composed of 32 O$^{2-}$ that embrace 64 tetrahedral interstices, (A-type), and 32 octahedral interstices, (B-type). The lattice constant corresponds to $a = 8.3987$ Å. Normal spinels are formed when 1/8 of the A sites are occupied by 8 divalent ions and when 1/2 of the B sites are occupied by 16 trivalent ions. Instead, in Fe$_3$O$_4$, 8 of the 16 Fe$^{3+}$ in the unit cell, are placed in A sites, whereas the other 8, together with the 8 Fe$^{2+}$, occupy the B sites in the inverse spinel structure, see figure 2.1. This arrangement of the iron atoms gives rise to a particularly high electrical conductivity of about 200 $\Omega^{-1}$cm$^{-1}$ at room temperature, as compared to the low values for normal spinels of about $10^{-5}\Omega^{-1}$cm$^{-1}$. This is believed to be due to hopping of spin-polarized electrons between magnetically ordered Fe$^{3+}$ and Fe$^{2+}$ in B-type sites. Furthermore, below the Nèel temperature trivalent irons

| | Magnetite | Haematite | Maghemite | Wüstite |
|---|---|---|---|---|
| Formula | $Fe_3O_4$ | $\alpha$-$Fe_2O_3$ | $\gamma$-$Fe_2O_3$ | FeO |
| Structure | Inverse Spinel | Corundum | Defective Spinel | Defect NaCl |
| Crystal System | Cubic | Hexagonal | Cubic/Tetragonal | Cubic |
| Space group | $O_h^7$-Fd3m | $D_{2h}^{16}$-R3c | $O_h^7$-Fd3m / $P4_32_12$ | $O_h^5$-Fm3m |
| Cell Dimensions (nm) | $a$=0.84 | $a$=0.50 $c$=1.38 | $a$=0.84 / $a$=0.83 $c$=2.50 | $a$=0.43 |
| Colour | Black | Red | Brown | Black |
| Magnetic order | Ferri- | weakly Ferro- | Ferri- | Antiferro- |
| Curie/Nèel temperature (K) | 850 $T_V$120 | 956 | 820-986[1] | 203-211 |
| RT saturation Magnetisation ($JT^{-1}Kg^{-1}$) | 90-92 | 0.3 | 60-80 | - |
| Density ($gcm^{-3}$) | 5.18 | 5.26 | 4.87 | 5.9 |

**Table 2.1**. Some of the properties of the Iron Oxides, (Cornell [20]). [1]The $T_C$ of maghemite is uncertain because it transforms to haematite at ~713K.

in A- and B-sites ($Fe_A^{3+}$ and $Fe_B^{3+}$) are antiferromagnetically coupled, so that only spins form the divalent B-sites ($Fe_B^{2+}$) contribute to the residual magnetism. This ferrimagnetic structure is in agreement with the value of the saturation magnetisation found experimentally of 4 $\mu_B$ [36].

The very first studies on $Fe_3O_4$ performed by Verwey [37, 38], suggested that the high conductivity at room temperature was the consequence of a random distribution of the iron ions in the octahedral planes. According to the crystal field theory, it is possible to represent the state of the octahedral (B) sites of $Fe_3O_4$ as shown in figure 2.2a [39]. The five $d$ orbitals split in two levels, two $e_g$ levels
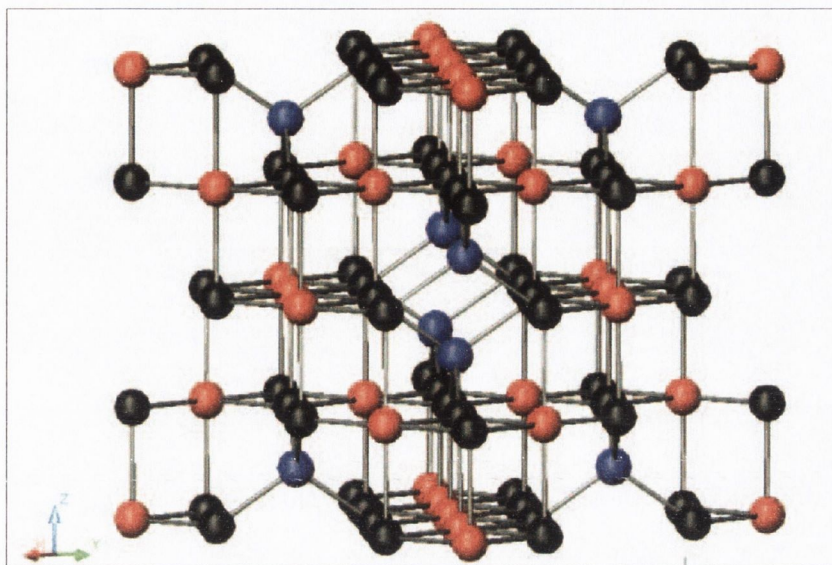
**Figure 2.1**. 3D view of the unit cell of $Fe_3O_4$, containing 32 oxygen anions (black), 16 octahedral iron ions (red) and 8 tetrahedral iron ions (blue).

and three $t_{2g}$ levels. The two different iron ions are present in the octahedral sites, $Fe^{2+}$ ($d^6$) and $Fe^{3+}$ ($d^5$). The $Fe^{3+}$ are in a high spin state, with the 5 electrons arranged in parallel, in accordance with Hund's rule. The antiferromagnetic alignment of the two consecutive crystallographic planes, causes the magnetic moment associated with these $Fe^{3+}$ ions in the B-sites to be canceled by the one of the $Fe^{3+}$ ions in the A-sites. There are three electronic configurations possible for a $Fe^{2+}$ ion, see figure 2.2b. The configuration with 4 unpaired electrons, is believed to be correct because it is in agreement with the value for the magnetisation measured experimentally of 4 $\mu_B$ per formula unit.

## 2.3 The Verwey Transition

At room temperature, the extra electron present in the $Fe^{2+}$ in a B-site is free to hop to a next $Fe^{3+}$ in a B-site, giving rise to the relatively high electrical conductivity. Below some 120 K temperature, the electrical resistivity of stoichiometric magnetite crystals suddenly increases by two orders of magnitude within
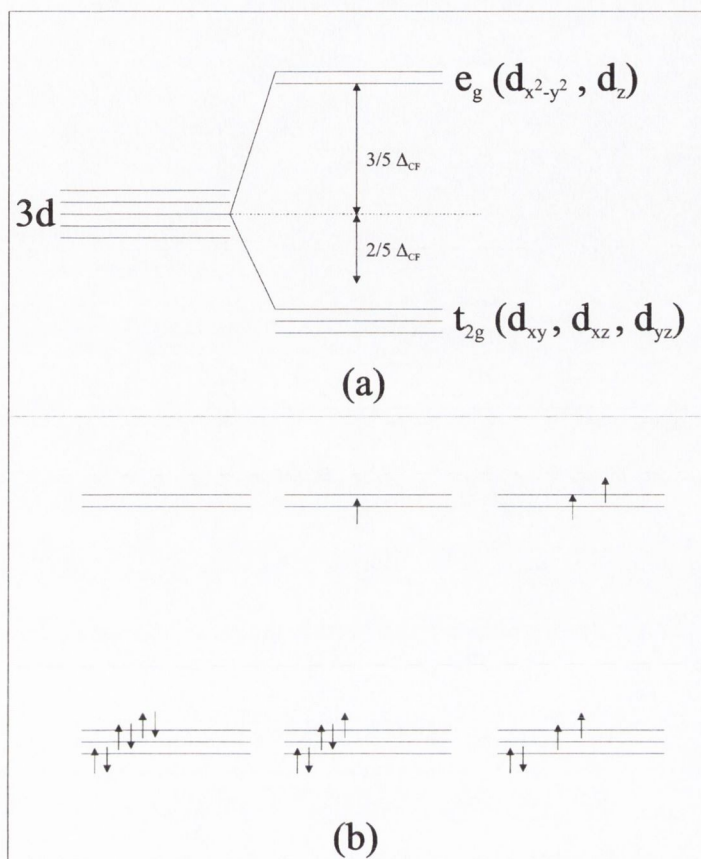
**Figure 2.2**. a) Schematic representation of the splitting of the 5 d electronic orbitals of an isolated iron ion in an octahedral crystal field. b) The three different possible electronic configurations of $Fe^{2+}$ in an octahedral site.

$\sim$5 K of range. This transition was discovered by means of heat capacity measurements in 1926 by Parks and Kelly [40] and belongs to the class of transitions, the Verwey transitions, that consist of a spontaneus sharp change in the lattice symmetry, and the electric conductivity, which occurs at a critical temperature $T_V$. Other properties of the crystal such as magnetization, magnetostriction, thermal expansion and heat capacitance, also exhibit a sudden variation at $T_V$ [41]. In $Fe_3O_4$, the crystallographic structure changes from cubic for the high temperature phase to monoclinic for the low temperature one [42]. The unit cell of the monoclinic phase, below $T_V$, is rotated by 45°, in the (001) plane, with respect to the cubic unit cell. Indicating the axes in the monoclinic phase as $a$,

$b$ and $c$, the $c$ axis is oriented along the $\langle 001 \rangle$ direction, while the $a$ and $b$ axes lie along the $\langle 110 \rangle$. Below the transition, the $c$ axis has an equal probability of lying along each of the three $\langle 001 \rangle$ directions. For each choice of $c$, there are two possible choices of $a$ and $b$. Therefore, cooling magnetite through the Verwey transition gives rise to a multiple twinned state, which can be removed by applying a magnetic field and a small stress along one of the [110] direction. The $c$ axis aligns to the magnetic field and the stress removes the degeneracy of the two directions for the $a$ and $b$ axes [43].

Originally, Verwey proposed [37, 38] a model for the transition in which the crystal transformation was from cubic to tetragonal symmetry and was accompanied by a freezing of the electron hopping. Bickford [44, 45] improved the model suggesting an orthorhombic symmetry for the low temperature phase. This model was accepted for a long time because it was supported by numerous measurements of magnetisation, conductivity, XRD and neutron diffraction [41, 46, 43, 17]. Afterwards, in 1968, neutron diffraction measurements performed on samples of better quality, revealed half-integer peaks consistent with a doubling of the lattice cell along the c axes [47, 48]. Such a superlattice was incompatible with the accepted Verwey model. The low-temperature phase was identified as monoclinic, and the original Verwey model was finally abandoned.

A lot of controversy also surrounded the kinetic mechanism of the transition. Multi-stage transformations were often reported by both experiments [49, 50, 51] and numerical simulations [52]. The confusion was generated by the poor quality of the samples that easily showed multi-stage transitions in experiments such as heat-capacitance measurements. In 1977, Matsui *et al.* finally addressed the problem and concluded that stressed released, stoichiometric magnetite is always characterized by a single stage, first order Verwey transition [53].

Despite the fact that the Verwey transition has been first detected 80 years ago, and extensively studied since the late 1940s, its mechanism is still matter

of discussion and controversy [17, 54, 55]. There are mainly two different mechanisms supported in the literature. The first one proposes the charge ordering of $Fe^{2+}$ and $Fe^{3+}$ on the same octahedral planes and is supported by nuclear magnetic resonance (NMR) [56, 57], high energy transmission electron diffraction [58] and high resolution neutron and synchrotron X-ray diffraction [59] experiments. The second hypothesis suggests the ordering of electrons in the Fe$_B$ sites in terms of condensation of phonons, and is supported by X-ray resonant scattering [60, 61] and more recent NMR [62] experiments. As both hypothesis do not bring enough evidence to give a conclusive description of the mechanism of the Verwey transition, more work and experiments are needed.

## 2.4 Half Metallic Fe$_3$O$_4$

As already mentioned, the most important property of Fe$_3$O$_4$ today, lies in the fact that it is a half metal (HM). This makes Fe$_3$O$_4$ a good candidate for applications in spintronics devices as a source of spin polarised carriers [7]. Furthermore, magnetite has a negative spin polarisation, a rare nevertheless necessary property in applications, which require both positive and negative spin polarisation. Figure 2.3 shows the schematic of a hypothetical HM showing the co-existence of metallic characteristics in the minority density of states (DOS) and insulating characteristics in the majority DOS. Band structure calculations were performed by Zhang and Satpathy in 1991 [10] using the local-spin-density approximation (LSDA) to the density functional theory (DFT). The self-consistent linear muffin-tin orbitals method in the atomic spheres approximation was employed. The lattice parameter and the net magnetic moment per formula unit are in agreement with experimental values. It was found that at the Fermi energy the electron bands are dominated by Fe(d) orbitals and that the O(p) orbitals lie well below $E_F$. More importantly, these results show that the spin-up bands are semiconducting while
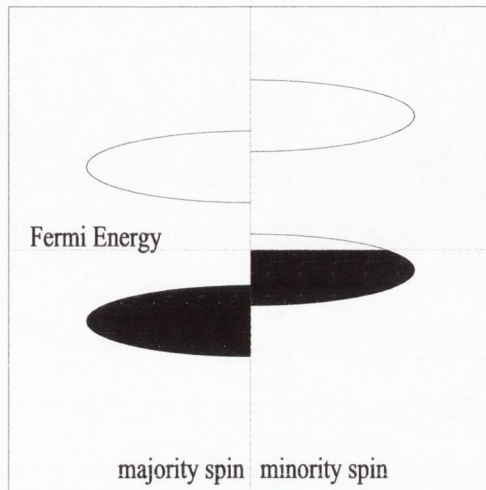
**Figure 2.3**. Schematic of an hypothetical HM with negative spin polarisation.

the spin-down band are metallic. Only spin-down electrons are present at the Fermi energy and, moreover, these electrons have a strong $Fe_B$ character. This is in agreement with some augmented plane wave calculations performed previously by Yanase and Siratori [9], as well as with spin polarised photoemission experiments of Alvarado [63] and Lad [64]. Although calculations have predicted the presence of only spin-down electrons at the Fermi energy, spin polarised photoemission spectroscopy (SP-PES) measurements were able to detect SP of -80±5% [65], -60±5% [66] and -55±10% [67]. Only recently, SP-PES experiments on $Fe_3O_4$/MgO(100) thin films performed by Morton *et al.* [68] showed a 100% SP. The authors suggest that the loss in the SP, that can be as high as 70%, is probably due to the cleaning process of the film by ion sputtering that alters the surface. Moreover, epitaxial trilayer junctions composed of $Fe_3O_4$ and doped manganite ($La_{0.7}Sr_{0.3}MnO_3$) have shown a negative magneto resistance (MR) as large as -25% in a low magnetic field of 4 Oe and -33% in 7 T [69]. A SP of about -34% was deduced from the experimental data.

## 2.5   Fe$_3$O$_4$/MgO Thin Films

Epitaxial Fe$_3$O$_4$ films are candidate materials for magnetic planar device applications [11, 27, 70, 71]. Interestingly, they exhibit physical properties that deviate from those of the bulk, such as magneto resistance (MR) [32, 34], larger electrical resistivity [33] and a magnetisation which does not saturate in high magnetic fields [31]. These differences are due to the presence of antiphase boundaries (APBs), which are natural defects occurring during growth of Fe$_3$O$_4$/MgO thin films [31, 72]. MgO crystallises in the rocksalt structure with a lattice constant equal to $a_{MgO}$= 4.212 Å [22]. This is close to half the lattice parameter of Fe$_3$O$_4$, ($a_{magn}$= 8.3987 Å), giving a mismatch of just -0.30%. One of the two reasons for the formation of APBs is that the lattice parameter of MgO is half that of Fe$_3$O$_4$. It is possible that during growth, two adjacent Fe$_3$O$_4$ islands can be shifted by $1/4\langle 110\rangle$ or $1/2\langle 100\rangle$, as shown schematically in figure 2.4. The second reason leading to the formation of APBs, is that the Fe$_3$O$_4$ islands can be rotated with respect to each other by 90°. It is worth noticing here that the oxygen sublattice is continuous and it is not disturbed across the APB. Only the cations sublattice is shifted at an APB.

Eerenstein *et al.* have reported that the domain size in Fe$_3$O$_4$ films grown using molecular beam epitaxy (MBE) decreases with decreasing thickness [74]. The domain size depends, not only on the film thickness, but also from the growth conditions. Higher growth or postannealing temperature favours larger domains, due to the annealing out of the APBs via a diffusive mechanism [74].

High resolution X-ray diffraction (HR-XRD) and transmission electron microscopy (TEM) strain relaxation studies on epitaxial Fe$_3$O$_4$/MgO(001) thin films grown by MBE [19] and magnetron sputtering [18], have shown that the films remain in a fully strained state up to ∼700 nm thickness. The critical thickness for strain relaxation, in this case, is estimated to be about 70 nm [19]. The anomalous strain relaxation behaviour has been attributed to the presence of APBs which,

- ● Mg
- ○ O in the MgO
- ● Fe$_{oct}$
- ● Fe$_{tet}$
- ○ O in the Fe$_3$O$_4$
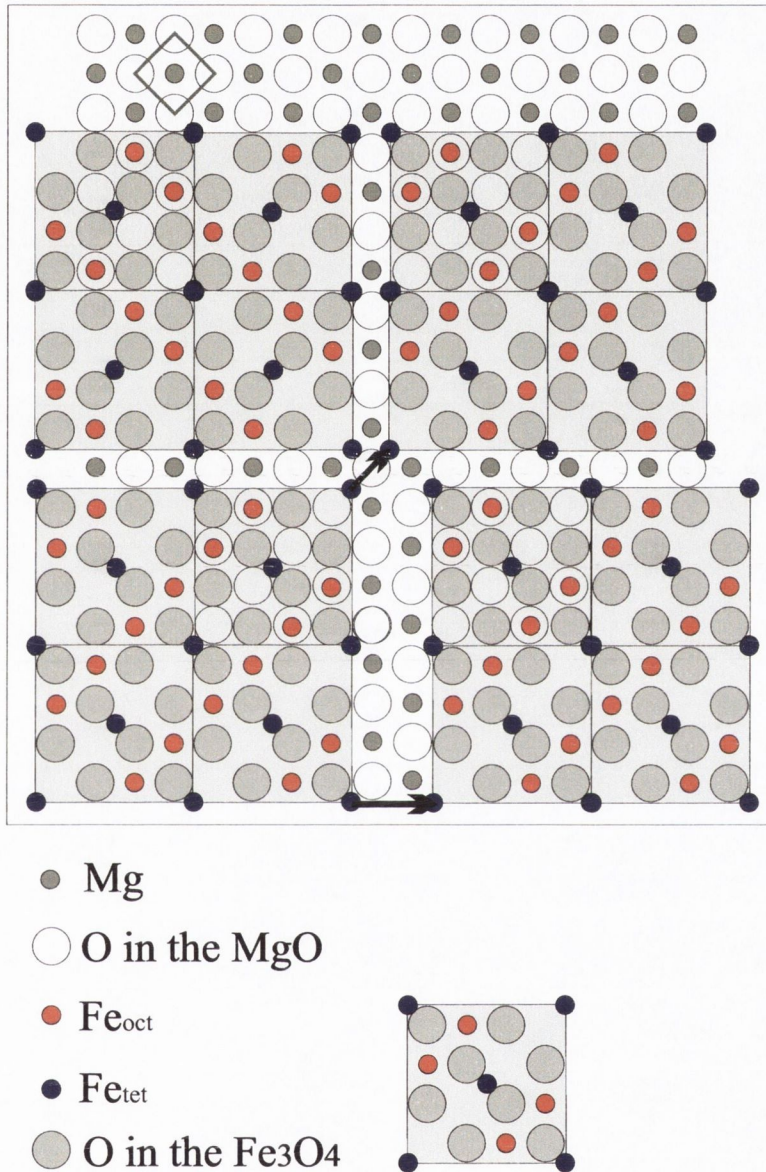


**Figure 2.4.** Shematic of the antiphase boundaries (APBs) that can be found in Fe$_3$O$_4$/MgO thin films. B corresponds to a shift of 1/2[100] of A. C corresponds to a shift of 1/4[110] of A and D corresponds to a 90° rotation of the monolayer unit cell in A. Reproduced from [73]

by alternating tensile and compressive strains developed within the growth islands and the APBs respectively, account for the anomalous accommodation of the strain in the films [19].

# Chapter 3

# The low temperature tunneling device (LTTD) for measurements of the deformation of $Fe_3O_4$

## 3.1 Introduction

In this chapter the low temperature tunneling device (LTTD) together with the experiments performed with it is introduced. The LTTD uses quantum tunneling to measure axial deformations of samples due to crystallographic changes as a result of phase transitions and charge transport. The LTTD works in the nanometer range with an accuracy of 0.25 Å, in low vacuum and at low temperature. It was employed to measure the deformation of a $Fe_3O_4$ single crystal rod and two thin film samples at the Verwey transition. In the case of the thin film samples, the transition was not detected even though a substantial signal was expected. The absence of the deformation at the transition was attributed to the fact that $Fe_3O_4$/MgO thin films are unrelaxed up to a thickness of $\sim$700 nm. This is due to the high density of antiphase boundaries (APBs) which are formed in the films during the heteroepitaxial growth [18, 19].

## 3.2   Theory of Tunneling Effect

The LTTD is based on the principle of operation of a STM, i. e. the quantum tunneling effect. Consider an electron with energy E moving in a potential U(z). In classical mechanics, it is described by the equation [75, 76]:

$$\frac{p_z{}^2}{2m} + U(z) = E \tag{3.1}$$

where $m$ is the mass of the electron and p its momentum. In quantum mechanics, the state of the same electron is described by the equation:

$$-\frac{\hbar^2}{2m}\frac{d^2}{dz^2}\psi(z) + U(z)\psi(z) = E\psi(z) \tag{3.2}$$

In the classical case, it is possible to distinguish 2 situations: ($i$) The allowed region, where $E > U(z)$ and the electron has a nonzero momentum $p_z$ and ($ii$) the forbidden region, with $E < U(z)$ which the electron cannot penetrate. In the quantum mechanics case in the region where $E > U(z)$, equation 3.2 has solutions:

$$\psi(z) = \psi(0)e^{\pm ikz} \tag{3.3}$$

where $k$ is the wave vector and is equal to $k = \sqrt{2m(E-U)}/\hbar$. In the region where $E < U(z)$, i.e. the tunneling region, the equation 3.2 has solutions:

$$\psi(z) = \psi(0)e^{-\kappa z} \tag{3.4}$$

where $\kappa$ is a decay constant and is equal to: $\kappa = \sqrt{2m(U-E)}/\hbar$. The probability density of finding an electron near a point $+z$ is proportional to $|\psi(0)|^2 e^{-2\kappa z}$, which has a nonzero value in the barrier region and thus a nonzero probability to penetrate the barrier. An analogous solution describes an electron state in the $-z$ direction $\psi(z) = \psi(0)e^{\kappa z}$.

This simple model explains some basic features of the one-dimensional metal-vacuum-metal tunneling effect (a more detailed treatment can be found in [77]),
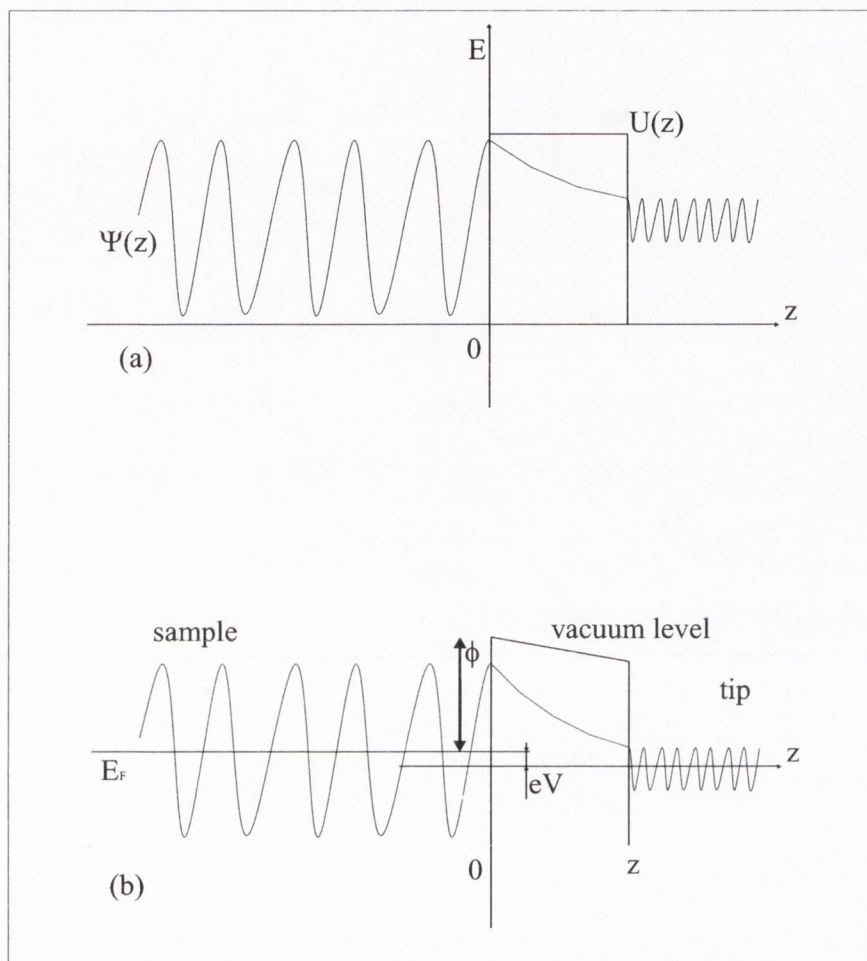
**Figure 3.1**. a)General tunneling barrier for an electron described by the wavefunction $\psi(z)$ in a one-dimensional potential U(z). b) Schematic of a STM tunneling junction under the applied bias voltage V.

shown in figure 3.1. Let us consider a metal surface and a sharp metal tip placed within a few angstroms of it. The *work function* $\phi$ of the metal surface is the minimum energy required to remove an electron from the sample/tip to the vacuum level and the *Fermi level* $E_F$ is the upper limit of the occupied states in the metal if thermal excitation is neglected. If the vacuum level is considered as the reference point of energy, then $E_F = -\phi$. Considering the simple case in which the work functions of sample and tip are equal, an electron can tunnel between them. Nevertheless, a bias voltage $V_b$ is necessary to have a net tunneling cur-

rent $I_t$. Applying $V_b$ to the tip, a sample state $\psi_n$ with energy $E_n$ lying between $E_F - eV_b$ and $E_F$, has a probability to tunnel into the tip. Assuming that $eV_b \ll \phi$ the energy level of all the sample states of interest are very close to the Fermi level, $E_n \approx -\phi$. The probability $w$ to find an electron at the tip surface $z = W$, is given by:

$$w \propto |\psi_n(0)|^2 e^{-2\kappa W} \tag{3.5}$$

where the decay constant $\kappa$ is now given by $\kappa = \sqrt{2m\phi}/\hbar$. The states on the sample surface within the energy interval given by $eV_b$ are responsible for the tunnel current $I_t$ and determine $I_t$ as follows:

$$I_t \propto \sum_{E_n=E_F-eV_b}^{E_F} |\psi_n(0)|^2 e^{-2\kappa W} \tag{3.6}$$

For small $V_b$, the sum in equation 3.6 can be written using the local density of states (LDOS) at the Fermi level. At a location $z$, the LDOS $\rho_S(z, E)$ of the sample is defined as $\rho_S(z, E) \equiv \frac{1}{\epsilon} \sum_{E_F-\epsilon}^{E_F} |\psi_n(z)|^2$ for a sufficiently small $\epsilon$. The value of the LDOS near the Fermi level is an indicator of whether the surface is metallic or not. The $I_t$ can be conveniently written in terms of the LDOS of the sample:

$$I_t \propto V_b \rho_S(0, E_F) e^{-2\kappa W} \tag{3.7}$$

The dependence of the logarithm of $I_t$ with respect to distance $W$ is a measure of the work function $\phi$, or the tunneling barrier height. It is also clear that $I_t$ is very sensitive to small variations in the distance between tip and sample.

## 3.3 The Low Temperature Tunneling Device

The low temperature tunneling device (LTTD), schematically presented in figure 3.2, consists of a cryostat equipped with a 15 litre dewar for liquid nitrogen or liquid helium and a superconducting magnet capable of producing a magnetic

field of up to 5 Tesla. The field is directed vertically, along the axis of the cryostat. The schematic of the system is shown in figure 3.2a. The cryostat
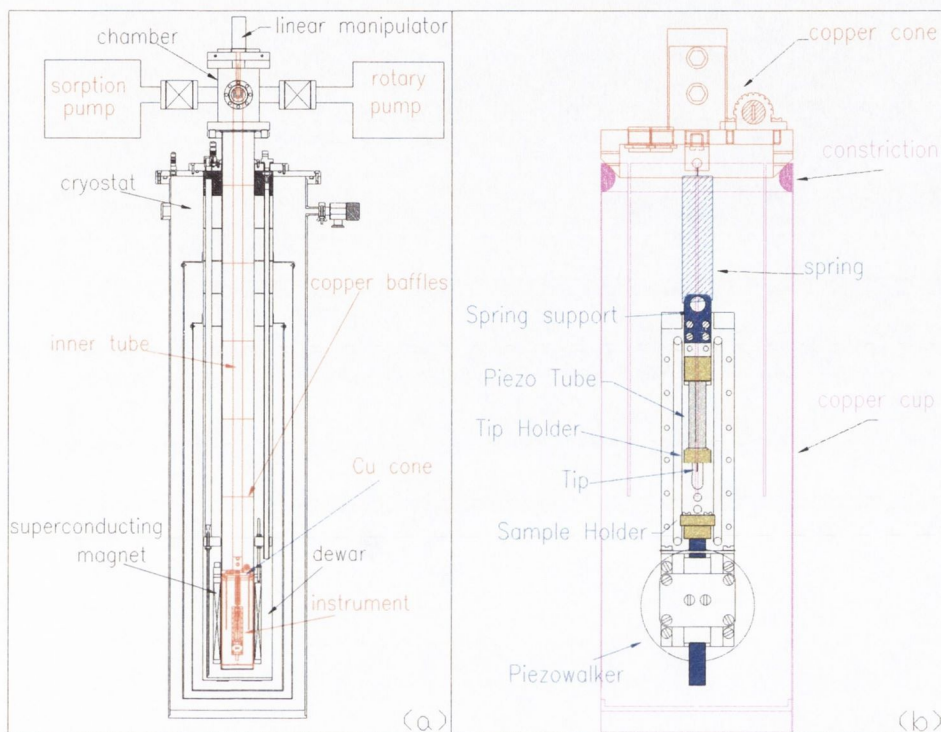


**Figure 3.2**. a)Schematic diagram of the low temperature tunneling device b)Detail schematic of the copper cone, constriction and instrument.

contains a vacuum insert which is connected to a small vacuum chamber at the top of the system. The pumping is achieved by a rotary pump and a sorption pump, and a thermocouple sensor monitors the pressure. A rotary vane pump is used to evacuate the system to $10^{-3}$ mbar before the experiments while a sorption pump, is operated at $10^{-3}$ mbar during the experiments because it is vibration free. Both pumps have a base pressure of $10^{-2} - 10^{-3}$ mbar. Helium gas can be introduced into the vacuum insert to reduce the cooling time. It is important to know the breakdown voltage of the gas in order to avoid discharge or sparking into the cryostat chamber due to the high voltage applied to the piezo elements [78, 79]. In the case of He at a pressure of $10^{-3}$ mbar, this values correspond to circa 40 kV·m, well above the voltage applied inside the system. The vacuum

chamber houses all the feedthroughs for the wires going to the instrument. It also contains a manipulator attached to a support tube at the end of which there is the copper cone that supports the instrument, see figure 3.2a. Several copper radiation baffles are arranged on the inner tube in order to decrease the boiling off of the coolant. The copper cone at the bottom of the inner tube rests on a purpose made OFHC copper cup inside the cryostat vacuum insert, as shown in figure 3.2b. The linear manipulator on the top flange is used to apply a force, so that the cone presses against the constriction in order to increase the heat transfer from the instrument to the wall of the cryostat insert. The heat transfer is directly proportional to the force applied [80, 81]. The instrument figure 3.2b is hooked to the copper cone by a copper-beryllium (CuBe) spring, in order to minimize high frequency vibrations and 3 copper braids with a cross section of 1 mm$^2$ and about 160 mm long, go from the instrument to the copper cone in order to enhance the heat transfer.

### 3.3.1    The instrument head

The instrument head comprises a piezowalker for coarse positioning of the sample with respect to the tip, and a piezo tube for fine positioning and z-measurement. A Cu electrode is affixed on top of the sample and connected to the bias voltage $V_b$. The electrode is isolated and shielded from the sample, if the sample is electrically conducting. The tunnel current between the tip and this electrode, which is biased, is maintained constant by a feedback loop that controls the piezotube. Any contraction or expansion of the sample underneath the electrode is therefore registered as a change in the voltage applied to the piezo tube, see figure 3.3. It should be noted that all parts of the head are made from non-magnetic materials so that the instrument may be used with the superconducting magnet.
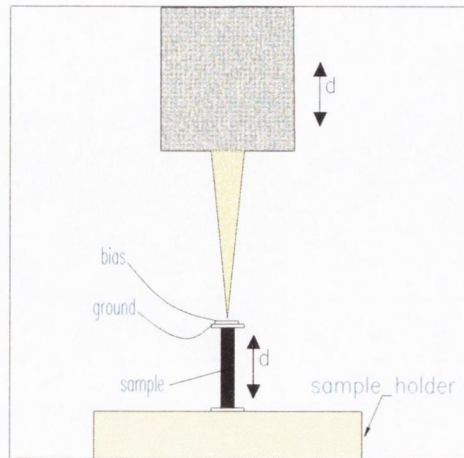
**Figure 3.3**. Schematic diagram of the operation of the LTTD. A generic sample expansion along its main axis is detected as a change in the voltage across the piezo tube.

### 3.3.1.1   Piezowalker

Piezowalkers are generally based on the concept of inertial slip-stick motion [82] and are capable of displacing objects over distances of several centimeters in submicrometer steps. The piezowalker employed in the LTTD consists of six
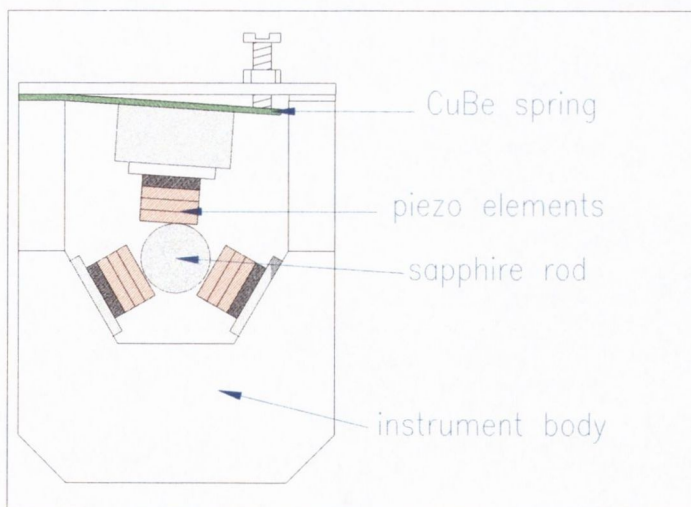


**Figure 3.4**. Schematic of the piezowalker. The CuBe spring presses the piezo stacks against the sapphire rod. Applying a sawtooth high voltage to the stacks results in the slip-stick motion of the rod.

piezo stacks arranged in a triangular fashion on two levels, compressed by a

spring against a sapphire rod, on top of which the sample holder is positioned, see figure 3.2b and figure 3.4. Simultaneously applying a high voltage sawtooth signal to all the piezo stacks results in the step-like motion of the sapphire rod. Although based on a simple principle, several features can be optimized in order to find the best solution for the desired case. For example, the sensitivity of the shearing mode piezo elements varies with temperature, decreasing significantly at low temperature. Under this condition, more piezo elements are needed in each stack to achieve a practical rate of movement. The voltage applied to the piezos must not exceed the depoling voltage, which varies with the thickness of the elements. Not only the amplitude but also the shape of the voltage is critical for the piezowalker to work under cryogenic conditions. The voltage must change very quickly; the rate of change used, or *slew rate*, is of the order of 120 $V/\mu s$. The size of the steps depends on the amplitude of the voltage applied to the piezos, which can be varied in order to bring the sample from a distance of a few centimeters to one or two millimeters distance from the tip. The precision *auto-approach*, is performed by the control electronics, which brings the sample to within a few Ångstrom range of the tip without crashing. The control unit also has a feedback loop which keeps the tunneling current or the sample-tip distance constant during the experiments. The possibility to rotate the sample has been implemented in the LTTD. This has been done by rotating one of the piezo elements by 90 degrees in each shearing stack in the piezowalker. Several basic tests were performed in order to characterize the piezowalker.

One of the most critical features of a piezo walker, particularly at low temperature, is the size of the steps as it determines the duration of the auto-approach procedure [83]. The piezowalker implemented in the LTTD moves the sapphire rod vertically and therefore, because of the action of gravity, the step size upward is smaller than the downward. This defines a step size ratio, that is the ratio between the size of the steps upward over the size of the steps downward. The step's

size as well as the step size ratio are very sensitive to the spring load. Typically, optimum performances are obtained when the step size ratio falls between 0.6 and 0.8. The procedure to measure the step size was as follows:

1. Bring the tip into tunneling with a sample. Adjust the position of the sample with the piezowalker (retracting the tip before each movement) until the Z voltage, $V_0$, is close to zero. The voltage sent to the piezo tube was measured with an oscilloscope before amplification.

2. Withdraw the tip and retract the sample by 10 steps using the piezowalker (depending on the voltage applied, the tip could still be within tunneling range even after taking 10 steps), bring the tip forward again and measure the value of the new Z voltage, $V_b$. Note that this value will change over time due to creep in the piezo tube and thermal drift, therefore it is only useful to take the initial value after each change in the piezo tube extension.

3. Withdraw the tip and bring the sample 10 steps closer to the tip. Bring the tip forward again and note the Z voltage, $V_f$. Note that in general $V_f$ will not be the same as $V_0$ because the step size in opposite directions are not equal.

The ratio of forward ($S_f$) to backward step size ($S_b$) is then given by the difference in the voltages as shown in equation 3.8:

$$\frac{S_f}{S_b} = \frac{V_b - V_f}{V_b - V_0} \tag{3.8}$$

Knowing the sensitivity of the piezo tube it is possible to evaluate the size of the steps in both forward and backward directions. Table 3.1 shows the results for the walker implemented in the LTTD.

### 3.3.1.2 Piezo Tube

The piezo tube is the other main part of the instrument because it keeps the tip in tunneling with the sample and is used to measure the sample deforma-

| Applied voltage | Step size forward | Step size backward | Step size ratio |
|:---:|:---:|:---:|:---:|
| 230 V | 0.77 nm | 1.11 nm | 0.69 |

**Table 3.1**. Parameters characteristic of the piezowalker implemented in the LTTD.

tions. It consists of a piezoelectric tube, with silver electrodes deposited onto the internal and external surfaces of it. In STMs, the outer electrode is divided into four quadrants, and different voltages are applied to each quadrant, in order to scan the surface of the sample. However, for the LTTD, the four parts have been shortcut, in order to allow only a one-dimensional z movement of the tube. Scanning features can easily be implemented in the device by disconnecting the 4 quadrants. In order to perform quantitative measurements, the piezo tube has been calibrated, using a thickness mode piezo, purchased from Stavely Sensors
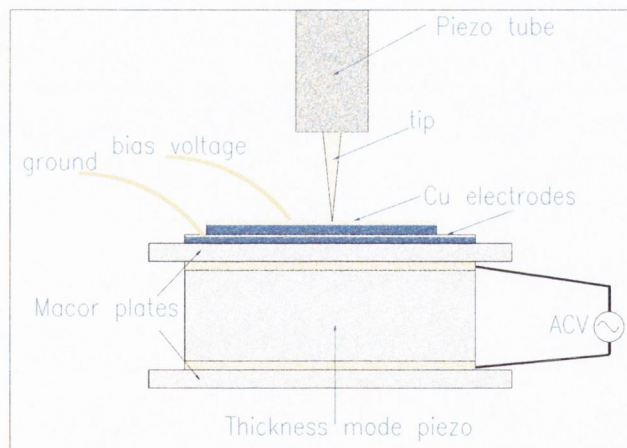


**Figure 3.5**. Schematic diagram of the experiment performed for the calibration of the LTTD piezo rube. A small AC voltage is applied to the thickness mode piezo while the tube scanner is kept into tunneling with the electrode on top of it. The amplitude of the oscillation is the same for the two piezo elements.

Ltd. [84]. A schematic of the calibration experiment is shown in figure 3.5. The thickness mode piezo was sandwiched between two copper plates connected to a voltage source. A gold coated glass plate was glued on top of the upper plate and connected to the ground, in order to shield the bias voltage from the voltage applied to the thickness mode piezo. The bias wire was electrically connected to

another gold coated glass plate glued on top of the first glass plate. Applying an AC voltage to the piezo results in an oscillation of its thickness along the vertical direction at the frequency of the applied voltage. When an adequately low frequency signal is chosen, the instrumental feedback keeps the tip in tunneling and the current constant. In this situation, the piezo tube oscillates with the same amplitude and frequency as the thickness mode piezo. Knowing the sensitivity of the thickness mode piezo, it is possible to determine the amplitude of the oscillations and therefore possible to calculate the sensitivity of the tube. Table 3.2 shows the parameters used during the experiment. The sensitivity of the piezo tube has been evaluated as follows. Applying a certain voltage $V_p$, the thickness mode piezo oscillates with a certain amplitude $A$, given by:

$$A = V_p \cdot d_{33} \tag{3.9}$$

where $d_{33}$ is the sensitivity of the thickness mode piezo. The same displacement occurs on the piezo tube due to the fact that the tunneling current is constant and the two piezos oscillate coherently. Then:

$$A = \frac{d_{31} \cdot L}{h} \cdot V_t = d_t \cdot V_t \tag{3.10}$$

where $V_t$ is the voltage across the two electrodes of the piezo tube, $d_{31}$ is the sensitivity of the piezo tube and h the thickness of the piezo tube. It is possible

| | | |
|---|---|---|
| sensitivity of thickness piezo | $d_{33}$ | 0.380 nm/V |
| sensitivity of piezo tube | $d_{31}$ | -0.173 nm/V |
| length of piezo tube | L | 0.018 m |
| thickness of piezo tube | h | 0.0005 m |
| frequency of the signal | $\nu$ | 2 Hz |
| bias voltage | $V_b$ | 0.050 V |
| current | $I_t$ | 1 nA |

**Table 3.2**. Parameters used during the calibration of the LTTD

then to equalize the two equations and to arrange them in order to relate the two voltages as follows:

$$V_t = \frac{d_{33}}{d_t} V_p \qquad (3.11)$$

Plotting $V_t$ against $V_p$ a linear relation is obtained, as shown in figure 3.6, and a value for $d_{33}/d_t$ is found from the graph equal to -0.12. The sensitivity of the
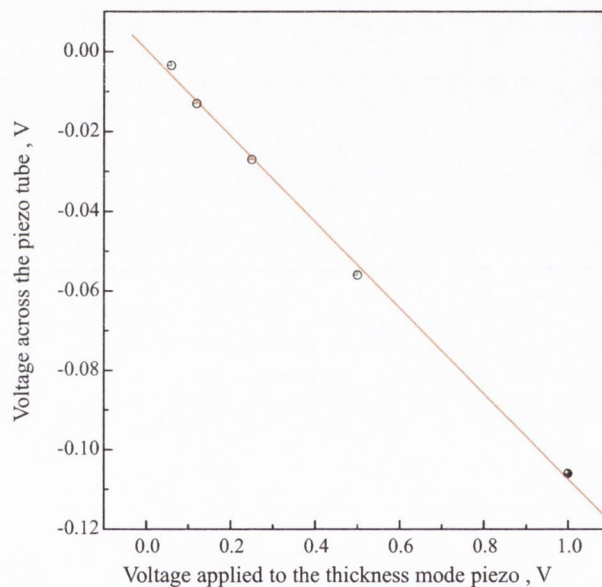


**Figure 3.6**. Piezo tube calibration curve.

thickness mode piezo $d_{33}$ has been given by the company [84] and is equal to 0.380 nm/V. Then $d_t$ is equal to 3.16 nm/V. Similar curves were obtained at different extension of the piezo tube. The same sensitivity was found in all regions except in the case when the piezo tube was almost fully contracted or fully extended. In these region the tube showed a highly non-linear deformation. Therefore, these regions will be avoided during experiments.

The reason why the piezo tube implemented in the LTTD was calibrated is because it was cut from a long tube and the sensitivity of piezo tubes are not as reliable, in general, as the one of piezo elements that operate in thickness mode

[84]. Nonetheless, it is possible to determine the value of $d_{31}$, which corresponds to -0.087 nm/V, half of the value declared by the supplier [84]. The lowest signal detectable at RT was equal to 8.0 mV. This determines the sensitivity of the instrument, which is therefore 25 pm.

## 3.4   Structural deformations of $Fe_3O_4$ at the Verwey transition

In this section, measurements of the deformations at the Verwey transition of a $Fe_3O_4$ single crystal and $Fe_3O_4$/MgO thin films are reported. The measurements were carried out with the LTTD. The films were grown on the (001) and the (111) crystallographic directions. The motivation for this study was to investigate the mechanism of the Verwey transition in strained layers of $Fe_3O_4$ deposited on MgO. The measurements on the single crystal were carried out firstly, to show that the LTTD works at low temperature and it is capable to measure the Verwey transition. Then, using the cantilever technique, measurements were carried out on the two thin film samples. Surprisingly no effect was detected. However, it was possible to formulate a possible explanation for this behavior.

### 3.4.1   Deformation of a single crystal rod of $Fe_3O_4$

The single crystal used for this experiment was grown using the floating zone technique by Prof. Y. M. Mukovskii [85]. The ingots were cut along the (001) direction and a rod of 1.10±0.02 mm was prepared. A measurement of the resistivity versus temperature showed the presence of the Verwey transition at 120 K, (figure 3.7) indicating good stoichiometry.

The $Fe_3O_4$ rod was glued with silver non-conducting paste onto the sample holder, as illustrated in figure 3.8. A gold coated glass plate was glued on top of the $Fe_3O_4$ rod and a Cu extrafine wire (diameter 0.125$\mu$m) was attached to the
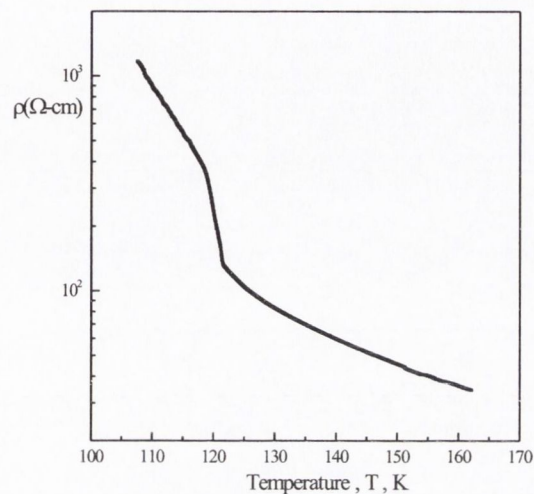
**Figure 3.7**. Resistivity versus temperature measurement of the single crystal sample used for the experiment. A Verwey temperature of 120 K was measured.

plate to provide the bias voltage. A K-type thermocouple (diameter 3 $\mu$m) was secured at the top of the rod with a high thermal conducting G-E varnish, for the measurement of the temperature, see figure 3.8. The rod was wrapped with a tungsten heating wire (diameter 0.15 mm), which was used to heat the sample locally.
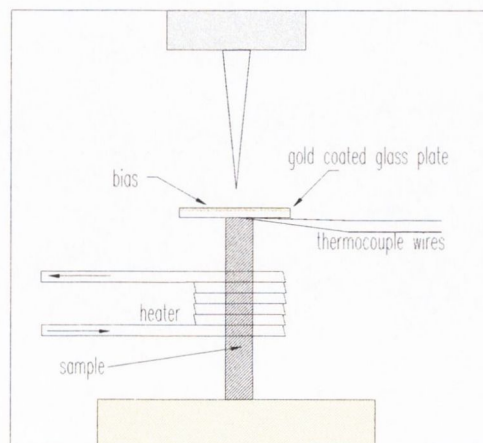


**Figure 3.8**. Schematic of the experimental configuration adopted for the measurement of the deformation of the $Fe_3O_4$ single crystal.
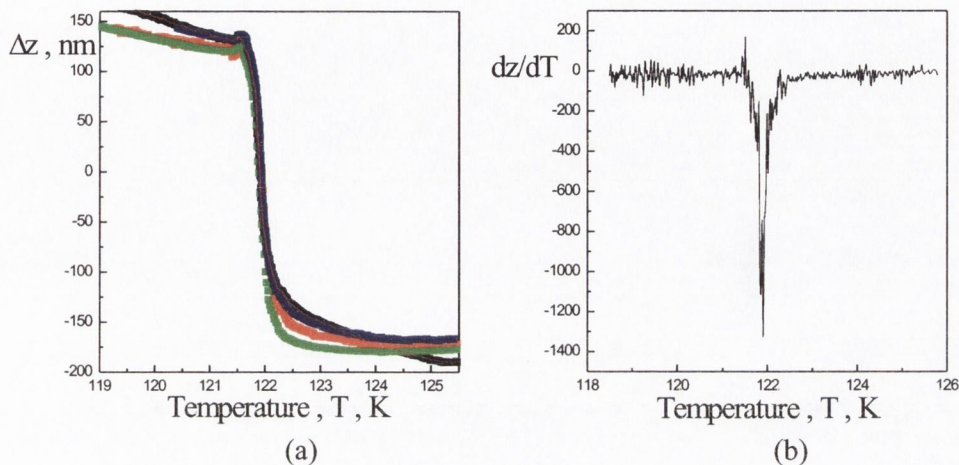
**Figure 3.9**. a) Deformation of the single crystal Fe$_3$O$_4$ rod oriented along the (001) direction. From the graph is possible to see that the transition is reproducible and that a Verwey temperature of 122 K is found. b) Derivative of the average deformation curve that highlights the occurrence of the Verwey transition.

After the sample was prepared in this way, the insert was placed inside the cryostat. The cryostat was then cooled down to near 105 K and the temperature stabilised with the Lakeshore 331 temperature controller [86].

Then, tunneling was established between the tip and the Cu plate and the temperature was slowly risen with a heating speed of ∼1 K/min. As the temperature was increased, the rod expanded linearly along the vertical direction. Upon reaching of the Vervey temperature at 122 K, it was possible to observe a sharp jump in the dimension of the rod, as shown in figure 3.9. A few temperature cycles were carried out, all showing high reproducibility. From the data it was possible to measure an average deformation of 283±5 nm along the (001) direction, which gives a relative expansion of the rod $\Delta L/L = 2.57 \times 10^{-4}$.

This data confirms that the LTTD can be used to measure the deformation of the Fe$_3$O$_4$ single crystal at the Verwey transition. It has to be noted here, that for these measurements, the Fe$_3$O$_4$ single crystal has to be free from stress [53] and a magnetic field needs to be applied along the c-axis [44], which is the

long axis of the rod in this case, to inhibit twinning. Nevertheless, the shape and reproducibility of the curve suggest that the sample is stress free and that the measurements are accurate enough in consideration of the purposes of this experiment. Second and multiple order transitions are expected for stressed samples, which were not observed in this case.

### 3.4.2 The cantilever bending technique

The deformation of the $Fe_3O_4/MgO$ thin films with temperature, was indirectly evaluated measuring the bending of the thin films with the cantilever bending technique. This technique is based on the measurement of the bending of a thin film sample, due, for example, to the stress developed during deposition of a thin film on a substrate, by means of interferometric methods [87, 88] or capacitance methods [13]. The technique can be used to measure stress in thin films during growth [13, 87], or the coefficient of thermal expansion of thin films [88, 89].

In the case of a thin film on a thick substrate, the stress in the thin film $\sigma_f$ is related to the radius of curvature $R$ by the well known Stoney formula [90, 91, 92, 93]:

$$\sigma_f = \frac{Y_s t_s^2}{6 t_f (1 - \nu_s) R} \tag{3.12}$$

In this formula, $Y_s$ is the Young modulus of the substrate, $t_s$ the thickness of the substrate, $t_f$ the thickness of the film and $\nu_s$ the Poisson ratio of the substrate [92]. This formula relates the stress in a thin film $\sigma_f$, generated from the mismatch strain $\varepsilon$, to the radius of curvature $R$ of the bilayer.

The average stress $\sigma_f$ in the thin film is proportional, in first approximation, to the strain of the film $\varepsilon_f$, multiplied by the biaxial modulus of the film $\frac{Y_f}{(1-\nu)}$ [92, 93]:

$$\sigma_f = \frac{Y_f}{(1 - \nu_f)} \varepsilon_f \tag{3.13}$$

where $Y_f$ is the Young modulus, the term $(1\text{-}\nu_f)$ takes into account the bidimensionality of the film, $\nu_f$ being the Poisson ratio of the film. The mismatch strain $\varepsilon_f$ is defined by [12]:

$$\varepsilon_f = \frac{a_f - a_s}{a_f} \tag{3.14}$$

where $a_f$ is the Fe$_3$O$_4$ lattice constant and $a_s$ corresponds to twice the MgO lattice constant. Combining the three equations, it is possible to find a relation between the curvature radius $R$ and the lattice parameters:

$$R = \frac{Y t_s^2 a_s}{t_f(a_f - a_s)} \tag{3.15}$$

where

$$Y = \frac{(1 - \nu_f)Y_s}{6(1 - \nu_s)Y_f} \tag{3.16}$$

In the cantilever configuration implemented in the LTTD, the deformation of the sample is measured as a change in the vertical direction $z$, see figure 3.10,
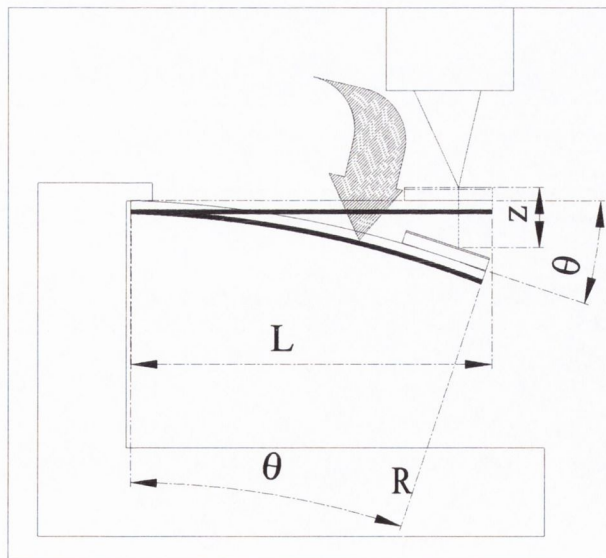


**Figure 3.10**. Experimental configuration. The thin film is considered as a heterogeneous bilayer that bends if exposed to a temperature change. In the case of a thin film on a thick substrate, a measure of this bending z is possible to evaluate the stress developed in the film.

**Table 3.3**. Parameters used for the calculation of the bending of the film.

| Length of sample | L | 10.00 mm |
|---|---|---|
| thickness of film | $t_f$ | 700 nm |
| thickness of substrate | $t_s$ | 0.5 mm |
| Young modulus of film | $Y_f$ | 144 GPa |
| Young modulus of substrate | $Y_s$ | 250 GPa |
| Poisson Ratio of film | $\nu_f$ | 0.33 |
| Poisson Ratio of substrate | $\nu_s$ | 0.171 |

which is equal to the ratio of the square of the length $L$ of the sample, divided by the radius of curvature $R$:

$$z = \frac{L^2}{R} \tag{3.17}$$

so, substituting in the equation 3.15 we obtain:

$$z = \frac{L^2(a_f(T) - a_s(T))t_f}{Y a_f(T) t_s^2} \tag{3.18}$$

where the (T) is to emphasize that the lattice constants depend on temperature.

The other parameters, i. e. Y and $\nu$, are assumed to be constant in the temperature range analysed. Rearranging this equation, it is possible to emphasise that the mismatch strain is related to the sample bending, by:

$$\epsilon = \frac{a_f(T) - a_s(T)}{a_f(T)} = \frac{Y t_s^2}{L^2 t_f} z \tag{3.19}$$

therefore direct measurements of $z$ give the strain at different temperatures. Knowing the cell parameters of MgO and Fe$_3$O$_4$ in the temperature range of interest it is possible to predict the bending expected in the same range. Considering the single crystal parameters, in the temperature range from room temperature to 100 K, it is possible to predict a bending, for the 700 nm Fe$_3$O$_4$/MgO(001) thin film, of about 400 nm in correspondence of the Verwey transition, see figure
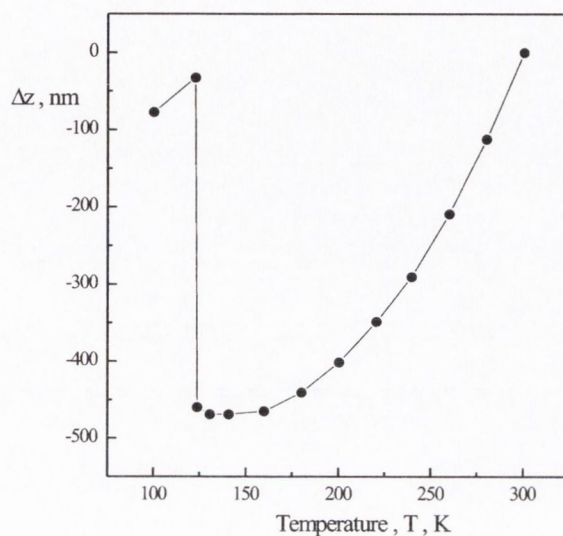
**Figure 3.11**. Calculation of the bending of the magnetite thin film based on bulk parameters. A deformation of about 400 nm is expected for the Fe$_3$O$_4$/MgO(001) 700 nm film.

3.11. This value is for a single crystal and does not take into account the stress developed in the thin film sample. However, it can be considered as an indication that the signal expected could be measurable using the LTTD.

### 3.4.3 Deformation of the Fe$_3$O$_4$/MgO thin films.

Two Fe$_3$O$_4$ films analysed were epitaxially grown on MgO(001) and MgO(111) single crystal substrates using oxygen plasma-assisted molecular beam epitaxy (MBE).
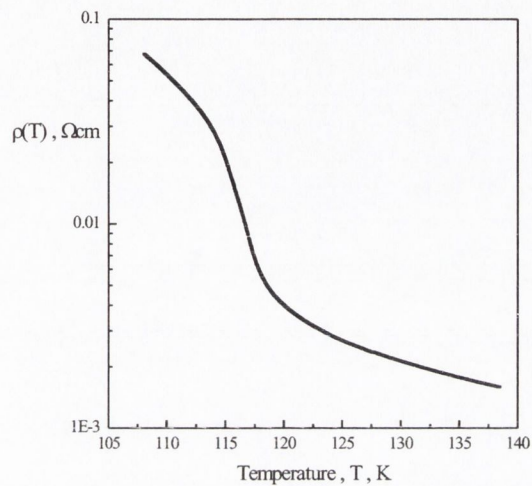
**Figure 3.12**. Resistivity measurement of the (001) thin film sample used for the experiment. A Verwey temperature of 116 K was measured.
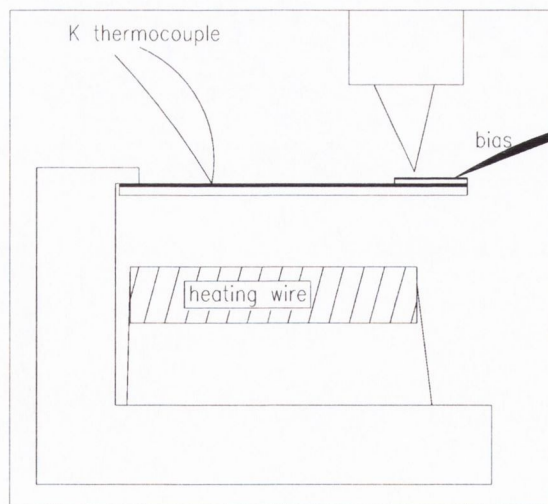


**Figure 3.13**. Schematic configuration of the experiment for the measurement of the bending of the thin films.

The $Fe_3O_4/MgO(001)$ film was 700 nm thick while the $Fe_3O_4/MgO(111)$ film was 400 nm thick. They were characterised by means of resistivity measurements, which confirmed the occurrence of a Verwey transition at 116 K and 123 K for the (001) and the (111) film respectively, see figure 3.12. The samples were secured with non conducting paste to an L-shaped sample holder as shown in figure 3.13. The $Fe_3O_4$ side of the sample was facing up. A gold coated glass plate was secured on this side with non-conducting paste and the wire for the bias voltage was attached. The sample was locally heated with a short W wire (diameter 0.15 mm) placed at the bottom of the sample. A K-type thermocouple was secured on the top side with G-E varnish. The sample was cooled down slowly (1 K/min) to 100 K. Then, it was subsequently heated via the W heating wire and the deformation recorded versus the temperature. Figure 3.14 shows a typical graph. It is possible to see that a linear deformation is measured, even if no transition is detected at $T_V$. The trend can be related to a linear expansion of the sample. It should be noted that some hysteresis was often observed in the heating-cooling
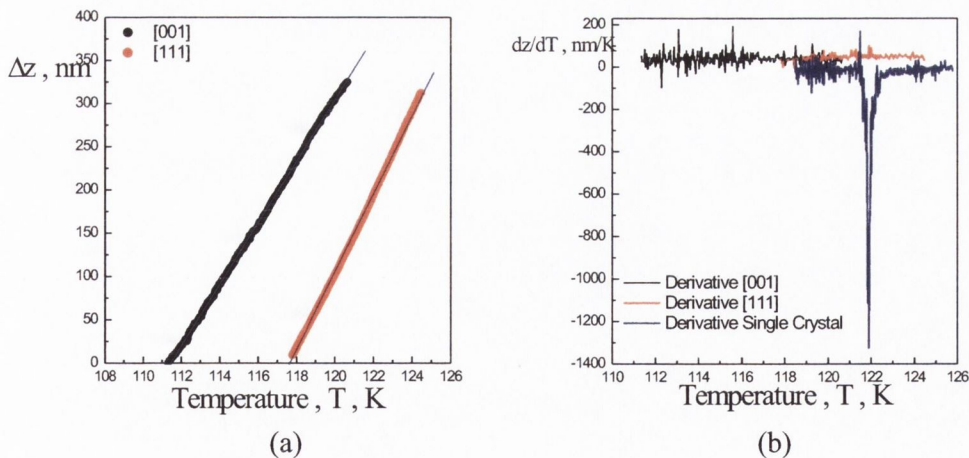


**Figure 3.14.** a) Deformation $\Delta z$ of the 2 thin films in the temperature range where the Verwey transition is expected. b) Derivative of the two curves, which show that no change in the deformation is detected. The derivative of the deformation of the single crystal is also reported for comparison.
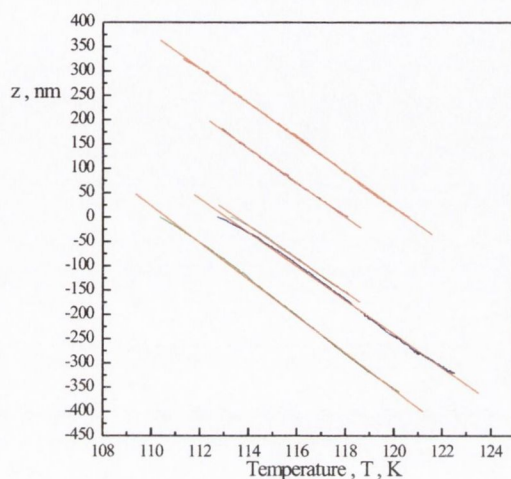
**Figure 3.15**. Deformation of the $Fe_3O_4/MgO(100)$ film around the Verwey temperature. The Verwey transition is not detected.

cycles. This is probably due to the fact that the temperature of the sample is not uniform. Several different experiments were carried out in slightly different conditions, changing the orientation of the sample, using different experimental configurations, such as with the heater coiled around the sample, or depositing an Al film on the MgO side of the sample. This was done in order to heat it in a more uniform way. However, no Verwey transition was detected for the two samples, even though a relatively high signal was expected at $T_V$. All the measurements produced a linear trend for the deformation of the sample. More experiments were carried out in a wider temperature range going from some 100 K to room temperature, however no transition was detected, see figure 3.15.

A possible reason for the absence of a signal in the LTTD, at $T_V$, could be given considering the presence of a high density of antiphase boundaries (APB) (see section 2.5) in the thin film [72, 33]. As already introduced in section 2.5, the presence of tensile and compressive strains in the films, generated within the grown islands and the APBs respectively, accounts for anomalous strain accom-

modation up to a thickness of $\sim$700 nm [18, 19]. The substrate applies a stress on the films which is tensile in the in-plane and compressive in the out-of-plane directions. Considering now, the occurrence of the Verwey transition in the films, the fact that they are in-plane stretched suggests that the deformation at the $T_V$ occurs only in the out-of-plane direction. In this case, no deformation would occur in the in-plane directions and this would result in the absence of the sample bending due to the transition. In this case no signal could be detected with the LTTD.

# Chapter 4

# Description of the Experimental Techniques and the Ultra High Vacuum System

## 4.1 Auger Electron Spectroscopy

Auger electron spectroscopy (AES) is one of the most important surface sensitive techniques for determining the chemical composition of the surface layers of conducting or semiconducting samples [94, 95]. The technique is based on the excitation of the so-called "Auger electrons", by bombardment with electrons of energy between 2 and 30 keV. In figure 4.1, an electron in the primary energy beam has sufficient energy to ionise a core level K of the sample with energy $E_K$. The empty electron position is filled by an electron from the level $L_1$, with energy $E_{L_1}$. This transition generates an energy equal to $E_K - E_{L_1}$, which can either be emitted as a X-ray photon (X-ray fluorescence) or transferred to a third electron, the "Auger electron", at a level $E_{L_{2,3}}$ in the example. This electron is emitted with a kinetic energy $E_{KL_1L_{2,3}}$ equal to the energy difference between the three

levels involved minus the sample work function $\phi$, as reported in equation 4.1.

$$E_{KL_1L_{2,3}} = E_K - E_{L_1} - E_{L_{2,3}} - \phi \qquad (4.1)$$

Auger spectroscopy is based upon the measurement of the kinetic energies of the emitted electrons. These are characteristic of each element and allow the qualitative and quantitative identification of the elements present in the first 2-10 atomic layers.
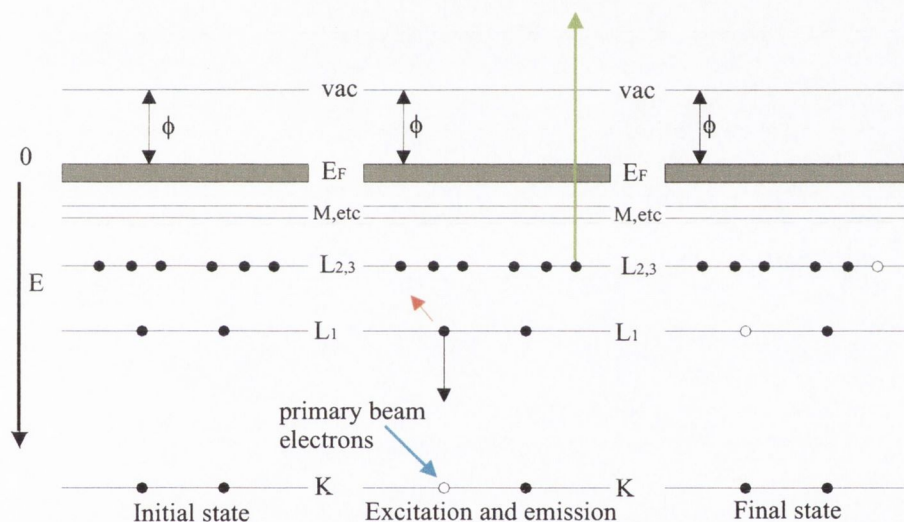


**Figure 4.1**. Schematic of the Auger emission process. The ground state is shown on the left. Centre: an incident electron from the primary energy beam creates a hole in the core level, K, by ionisation, blue arrow. Relaxation occurs and an electron from the $L_1$ levels fills the core level hole, releasing an energy, $E_K-E_{L_1}$. This energy can be emitted as a photon (red arrow), or can be given to a secondary electron, which is then emitted from the crystal, green arrow. The state following emission is shown on the right.

## 4.2 Low Energy Electron Diffraction

Low energy electron diffraction (LEED) is one of the principal techniques for the determination of the surface structure of solids [96]. A sample with a well ordered crystalline surface structure is hit by a monochromatic beam of low energy

electrons normal to it. The impinging electrons are back-scattered by the atoms in the surface layer of the crystal onto a fluorescent screen, which displays the diffraction pattern of the surface. Information regarding surface structure may be obtained by both the position and the intensity of the spots. The spots' positions yields information on the size, symmetry and rotational alignment of the surface layers with respect to the symmetry of the bulk crystal. The intensities of the various diffracted beams, recorded as a function of the incident electron beam energy, generate the so-called I-V curves which, by comparison with theoretical curves, may provide accurate information on atomic positions. The simple production of a LEED photograph, without the analysis of the spots intensity, is sufficient to give information of the symmetry of the surface reconstruction, or about imperfections in the surface, such as steps or islands, or to determine whether any molecules adsorbed on the surface, are arranged in an ordered way.

Consider the electron beam as a plane wave incident on the crystalline sample with wavelength $\lambda$. The atoms of the crystal will scatter these electrons, as they are areas of high electron density. Considering the atoms as point particles, the incident plane wave will be scattered in all directions. For an ordered crystal surface, interference will restrict the net flux to those directions where the scattered waves are in phase. This condition is met only when the scattered waves from neighbouring unit cells differ by an integral number of wavelengths $\lambda$. For the simple case of a one-dimensional lattice, this in-phase condition for constructive interference is illustrated in figure 4.2, where the sample is normal to the incoming beam. Considering two rays of the backscattering of a wavefront from two adjacent atoms at an angle $\theta$, it is clear that there is a path difference $d$ between the scattered rays. This path difference is equal to $d = a sin\theta$. In order to have complete constructive interference, $d$ must be equal to an integer number $n$ of wavelengths $\lambda$, $d = n\lambda$. This results in the condition expressed in equation 4.2:

$$n\lambda = a sin\theta \qquad (4.2)$$
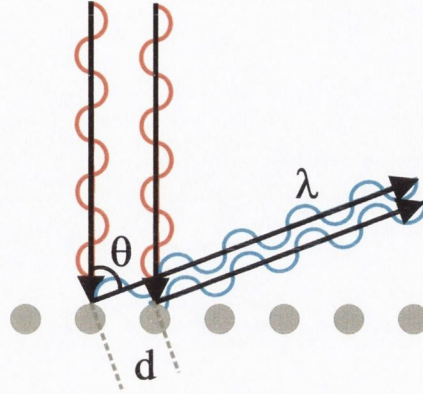
**Figure 4.2.** Schematic of the Bragg condition for a 1D lattice. Only in the case of coherent interference between the scattered rays, it is possible to detect a diffracted beam.

This condition is known as the Bragg law. The LEED pattern consists of spots in agreement with the Bragg law, that appear on the screen giving an image of the reciprocal lattice of the surface. The real space lattice parameter $\vec{a}$ is related to the reciprocal space lattice parameter $\vec{a^*}$ by $\vec{a^*}=1/\vec{a}$.

For surface diffraction to occur in a 2D system, with translational vectors $\vec{h}$ and $\vec{l}$, the incoming electron beam must conserve both its energy and the component of its momentum parallel to the surface:

$$\vec{k_\parallel^2} + \vec{k_\perp^2} = \vec{k'^2_\parallel} + \vec{k'^2_\perp} \quad , \quad \vec{k'}_\parallel = \vec{k}_\parallel + \vec{g_{hl}} \tag{4.3}$$

where $\vec{k}_\parallel$ and $\vec{k}_\perp$ are the parallel and perpendicular momentum components of the incident beam, while $\vec{k'}_\parallel$ and $\vec{k'}_\perp$ are those of the diffracted beam. The reciprocal lattice vector, now labelled $\vec{g_{hl}}$, is related to the beam energy $E_{eV}$, the electron mass $m_e$, and the diffraction angle $\theta$ by:

$$|\vec{g_{hl}}| = |h\vec{a^*} + l\vec{b^*}| = |\vec{k}|sin\theta| = \frac{\sqrt{2m_e E_{eV}}}{\hbar}sin\theta \tag{4.4}$$

where $\vec{a^*}$ and $\vec{b^*}$ are the reciprocal lattice primitive net vectors. These are related to the real space vector $\vec{a}$ and $\vec{b}$ by [96]:

$$\vec{a} \cdot \vec{a^*} = \vec{b} \cdot \vec{b^*} = 2\pi \quad \vec{a} \cdot \vec{b^*} = \vec{b} \cdot \vec{a^*} = 0 \tag{4.5}$$

This shows the direct correspondence between the observed diffraction pattern and the reciprocal lattice of the surface. The reciprocal lattice vector $\vec{g}_{hl}$ lies in a direction that is orthogonal to the plane of the real space lattice that is denoted by the Miller indices $h$ and $l$. The Miller indices of the diffracting planes are used to index the diffraction spots of the LEED pattern.

In general for LEED experiments, the sample is normal to the incoming beam. This means that $\vec{k}_{\parallel} = 0$ for the incident electrons. Therefore the observed diffraction pattern will be an image of the reciprocal lattice of the surface. LEED patterns of surfaces are taken at energies ranges between 20 and 500 eV. In this energy range, the de Broglie wavelength of electrons have the same order of magnitude as the interatomic distances of the crystals. The electron mean free path is of the order of $\sim$5-10 Å, meaning that this technique is sensitive only to the surface layers.

## 4.3   Scanning Tunneling Microscopy

The scanning tunneling microscope STM invented by Binning and Rohrer in 1981 [97], is without doubt the most important instrument developed in surface science, in recent years. The possibility to image the atomic structure of conducting and semiconducting materials has revolutionised the field, allowing the possibility of studying the properties of material surfaces in direct space. In reality, the technique probes the electronic structure of the atoms at the surface and topographic information is derived from that.

STMs are based on the principle of quantum mechanical tunneling. The theory of the tunneling effect has been described in detail in section 3.2. An atomic sharp metal tip is brought to within 1 nm from the surface of a conducting or semiconducting sample. A voltage is applied across the two electrodes, tunneling is established and a tunneling current is detected. As demonstrated in section

3.2, the tunneling current $I_t$ can be expressed as follows:

$$I_t \propto V_b \rho_S(0, E_F) e^{-2\kappa W} \tag{4.6}$$

where $V_b$ is the bias voltage applied to the surface electrode, $\rho_S(0, E_F)$ is the local density of states (LDOS) of the sample, $E_F$ the Fermi energy, $\kappa$ is a decay constant given by $\kappa = \sqrt{2m\phi}/\hbar$ and $W$ the barrier height. In reality the tunneling current is also dependent on the LDOS of the tunneling tip. The significance of the tip contribution can be accounted for through a time dependent perturbation model of a metal-insulator-metal tunneling, proposed by Bardeen [98]. In this approach a transfer hamiltonian $H_T$ is used to describe the tunneling of an electron, from a sample state $\psi$, to a tip state $\chi$. The tunnel current is a convolution of the sample LDOS $\rho_S$ and the tip LDOS $\rho_T$.

$$I_t = \frac{4\pi e}{\hbar} \int_0^{eV} \rho_S(E_F - eV + E)\rho_T(E_F - E)|M|^2 dE \tag{4.7}$$

The tunneling current $I_t$ also includes a tunneling matrix element $M$, which describes the amplitude of electron transfer across the tunneling barrier, as a function of the overlap between sample states ($\psi$) and tip states ($\chi$).

$$M = \frac{\hbar}{2m} \int (\chi^* \frac{\partial \psi}{\partial z} - \frac{\partial \chi^*}{\partial z}) dS \tag{4.8}$$

It is determined by a surface integral on the medium separating the two electrodes. If $M$ is constant over the voltage range probed, the tunnel current is determined by a convolution of the LDOS of the two electrodes, the tip and the sample.

Once tunneling is established, the tip is scanned mechanically across the surface. There are two basic modes for the scanning process, namely, constant current or constant height. The most commonly used is the constant current mode, where the tunneling current is kept constant, in the range from a few pA to 1-2 nA, by a feedback control unit that changes the tip-sample separation in response to a change in the tunneling current. However, in the constant height mode, the barrier height is kept constant and the tunneling current recorded as a

function of the tip position. In this thesis, the STM was operated in the constant current mode for all the measurements performed.

### 4.3.1 Scanning Tunneling Spectroscopy

Since tunneling involves transfer of charge from occupied states of one electrode to unoccupied states of the other electrode, by varying the magnitude and direction of the bias voltage, it is possible to perform scanning tunneling spectroscopy. In the limit of low bias ($\sim$mV), the tunneling current is linearly proportional to the applied voltage. However, for higher bias the tunnel current generally does not exhibit ohmic behaviour, and the image obtained with STM can vary greatly with junction bias. This is particularly true for semiconducting surfaces. Scanning tunneling spectroscopy (STS) allows one to examine how the tunnel current varies with voltage by acquiring I(V) curves of the tip-sample tunnel junction [76]. In general, the feedback loop is interrupted for a few hundred microseconds so that the tip sample distance remains constant during the curve acquisition. There is a delay in the sample-tip distance to stabilise. Due to the exponential dependence of the tip-sample distance on the tunnel current, it is vital that this distance remains constant during the curve acquisition. The bias voltage is then ramped through the desired range and the I(V) characteristic of the junction measured. The feedback loop is then re-engaged and scanning continues. Curves can be taken at a single point, or a grid I(V) map of the surface can be obtained. As the tunneling current is a convolution of the tip and the sample DOS, the measurements will only contain meaningful information about the sample DOS if the tip DOS is constant over the voltage range used:

$$\rho_T(E) = const \tag{4.9}$$

and again using the assumption that the tunneling matrix element $M$ is constant over the voltage range probed, then from equation 4.7:

$$\frac{dI}{dV} \propto \rho_S(E_F - E_V + E) \tag{4.10}$$

this equation essentially means that, assuming the validity of the above assumptions, a measure of the sample DOS can be obtained from the derivative of the I(V) curve. However, it must be borne in mind that, in reality, the assumption of a constant $M$ does not hold. The tunneling current is always highest for states at the Fermi level. Therefore when tunneling from the tip to the sample, most of the tunneling electrons will come from the Fermi level of the tip and will probe the empty states of the sample. However, when tunneling from the sample to the tip, most of the tunneling electrons will come from the Fermi level of the sample, therefore offering limited information on the occupied states of the sample. A data normalization process, first proposed by J. Stroscio *et al.* [99] and N. D. Lang [100], can help solve this problem. From equation 4.7

$$I_t \propto \int_0^{eV} \rho(E)D(E)dE \tag{4.11}$$

where D(E) is the transmission probability for an electron.

$$\frac{dI/dV}{I/V} \approx \frac{dlnI}{dlnV} \approx \frac{\rho(eV)D(eV)}{\frac{1}{eV}\int_0^{eV} \rho(E)D(E)dE} + ... \tag{4.12}$$

Then, to a first order approximation, the transmission probability cancels and the normalised conductivity is approximately proportional to the DOS;

$$\frac{dI/dV}{i/V} \approx \frac{\rho(eV)}{\frac{1}{eV}\int_0^{eV} \rho(E)D(E)dE} \tag{4.13}$$

The inherent weakness of STS as a spectroscopic technique is that it only maps the electronic states that protrude from the sample and significantly overlap with the tip wavefunction, essentially resulting in a negative penetration depth [76].

## 4.4  The UHV System

The Ultra High Vacuum (UHV) system in which these sample were characterised and analysed consists of three main chambers: the preparation chamber, the Room Temperature STM (RT-STM) chamber and the Low Temperature STM (LT-STM) chamber. The layout of the system is shown in figure 4.3.

A detailed description of the different chambers has been given elsewhere [101, 102, 103] and only a brief introduction of the RT-STM chamber and the Preparation Chamber will be given in the following section. Every chamber can be valved off and independently brought to atmospheric pressure without breaking the vacuum in the other chambers. This is done via a series of UHV gate valves [104]. A fast entry loadlock allows the transfer of tips and samples in and out of the preparation chamber without breaking the vacuum [105]. A differential 20 $\ell \cdot s^{-1}$ ion pump [105] keeps the vacuum of the order of $10^{-8}$ Torr. The transferring of samples and tips inside the UHV system is done by means of wobblesticks and magnetically coupled linear drives [106] with access to each sample stage. The pressure in each chamber is monitored by nude Bayard-Alpert type ionisation gauges [105]. The whole system is supported on a stainless steel frame which can be floated on pneumatic dampers to minimise vibration during STM measurements.

## 4.5  The Preparation Chamber

Several different pumps can be operated to reach and maintain the system in UHV ($10^{-10} - 10^{-11}$ Torr). A 260 $\ell \cdot s^{-1}$ turbomolecular pump [107] backed by a 0.7 $\ell \cdot s^{-1}$ two-stage rotary vane pump, generates the vacuum in the chamber. Then, a double-ended 240 $\ell \cdot s^{-1}$ differential ion pump [105] maintains the system in UHV conditions. A liquid nitrogen cryoshroud, together with a titanium sublimation pump (TSP), is inserted in the base flange of the ion pump and a non-evaporable

getter (NEG) pump [108] is positioned mid way along the chamber. Inside the chamber, different facilities are present that allow tip and sample preparation. A resistive heater, an $Ar^+$ gun, precision leak valves for the introduction of high purity gases, a triple evaporator with integral flux monitor [109] and a quartz crystal deposition monitor [110] are present for routine cleaning and treatment of samples and tips. The preparation chamber also contains a cylindrical mirror analyser (CMA) based Auger electron spectroscopy subsystem [105].
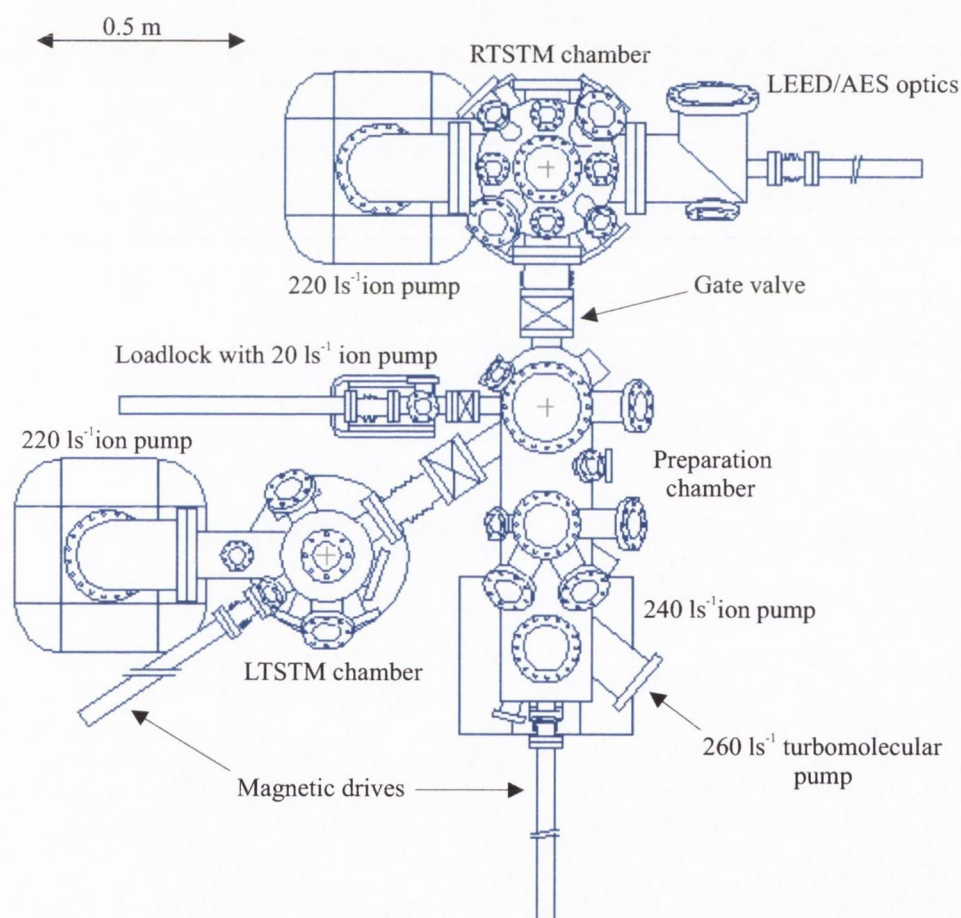


**Figure 4.3**. Top view schematic of the ultra high vacuum (UHV) system.

### 4.5.1 The resistive heater

The resistive heater was designed by C. Kempf and its schematic is shown in figure 4.4. It consists of an alumina crucible with a spiral groove machined
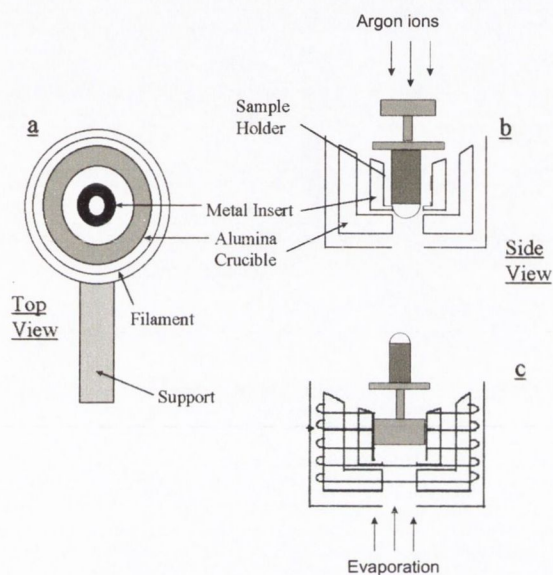


**Figure 4.4.** Shematic illustration of the resistive heater. a) top view. b) Lateral view. The sample, or tip, is inserted face-up for ion etching. c) Lateral view. The sample can sit face-down in the heater for evaporation experiments. Reproduced from [111]

along its circumference, along which a 0.2 mm thick tungsten wire is wrapped. It also acts as a sample stage for the $Ar^+$ etching and thin film deposition. The sample holder sits inside a tantalum insert fitted inside the crucible. The sample holder consists of a tantalum cap that screws onto a molybdenum body. Both the crucible and the tantalum insert have concentric apertures in their bases to allow deposition of thin films from the evaporator, positioned below the resistive heater. Therefore, the sample is positioned face-down for film deposition and face-up for $Ar^+$ ion bombardment. The crucible is supported by a stainless steel can, which is attached to a feedthrough for the quartz crystal monitor. The feedthrough comprises two water cooling pipes and a BNC feedthrough to carry the signal

from the in-situ quartz crystal to the ex-situ monitor. A separate feedthrough carries the connections to the heater filament and a K-type thermocouple spot-welded to the tantalum insert. The thermocouple enables the calibration of the resistive heater each time the filament is replaced, obtaining a temperature (K) versus power (W) calibration curve. The temperature range of the resistive heater is 350 K to 900 K.

## 4.5.2 The e⁻-beam heater

The electron beam heater was designed and build by Dr. J. Osing [102] and its schematic is shown in figure 4.5. This heater is used for annealing at high
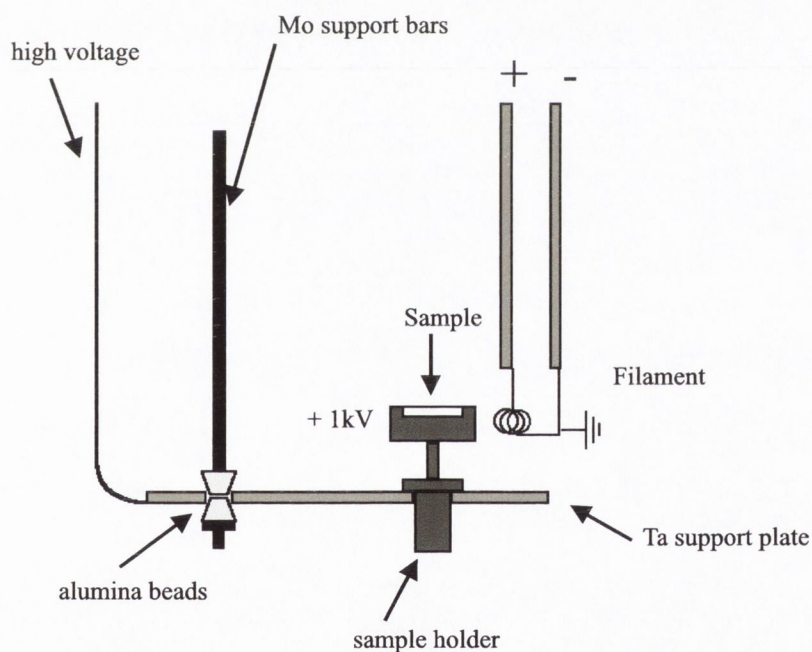


**Figure 4.5**. Schematic illustration of the e⁻-beam heater. Reproduced from [102]

temperatures up to 2500 K. The sample holder is inserted into a tantalum stage kept at +1 kV. A DC current is driven through a grounded thoriated tungsten filament (diameter 0.15 mm, 1% thorium), which generates thermionic emission of electrons. The filament is positioned very close to one of the side of the

sample cap so that the electrons, accelerated from the positive bias, collide with it transferring their kinetic energy to the sample as heat. A temperature gradient is therefore present across the sample due to the position of the filament. The temperature of the surface is measured with an infra-red pyrometer (Altimex UX-20/600 [112]) from a viewport.

### 4.5.3   The Ar$^+$ ion gun

For the in-situ cleaning of the samples surface and STM tips, the system is equipped with an inert sputter ion source [113] for Ar$^+$ etching. This is fitted with two tungsten filaments through which a current of 2.6 A is driven during routine operation. The Ar gas is introduced by means of a leak valve directly into the gas cell of the ion gun and ionised by electron bombardment. Upon discharge, the Ar$^+$ ions are accelerated by a negative voltage of value between -0.2 and 2.0 kV, applied to the sample or tip to be sputtered. Discharge currents are typically 30-40 mA. The diameter of the target is taken as 11 mm, i.e. the diameter of the circular tantalum insert in the resistive heater that accommodates the sample or tip. This is electrically isolated by the ceramic crucible. The target current $I$ passing through the sample or tip is measured via the thermocouple spot-welded to the tantalum insert. This reach values comprises between $7.0 \leq I \geq \mu A$ when the conditions are 0.5-2.0 keV beam energy and Ar pressure of $5 \times 10^{-6}$ Torr.

### 4.5.4   The triple evaporator

The deposition of thin films is carried out using a three cell electron beam evaporator, the Omicron EFM3T UHV triple evaporator, with integrated flux monitor [109]. The evaporant can be an ultrapure metal rod or small chips of the desired material placed in a crucible. The evaporation is realised by an electron beam that heats the source inducing evaporation. The instrument allows high precision sub-monolayer and multi-layer depositions. The flux monitor consists of

an ion collector at the beam exit column. At a given electron emission current and $e^-$-beam energy, the ion flux is directly proportional to the flux of the evaporated atoms. A shutter at the beam outlet, allows the simultaneous evaporations of one, two or three evaporants as well as precise control of evaporation times. The evaporation cell is fitted with a water cooled copper cylinder which, together with a highly localised heating of the evaporant, reduces changes in the pressure during evaporation.

## 4.6 Auger Electron Spectroscopy Set-Up

The Auger analyser is a cylindrical mirror analyser (CMA, model 10-155A Physical Electronics [114]). A schematic of the Auger analyser is seen in figure 4.6. The primary electron beam is generated from a hot filament source, and
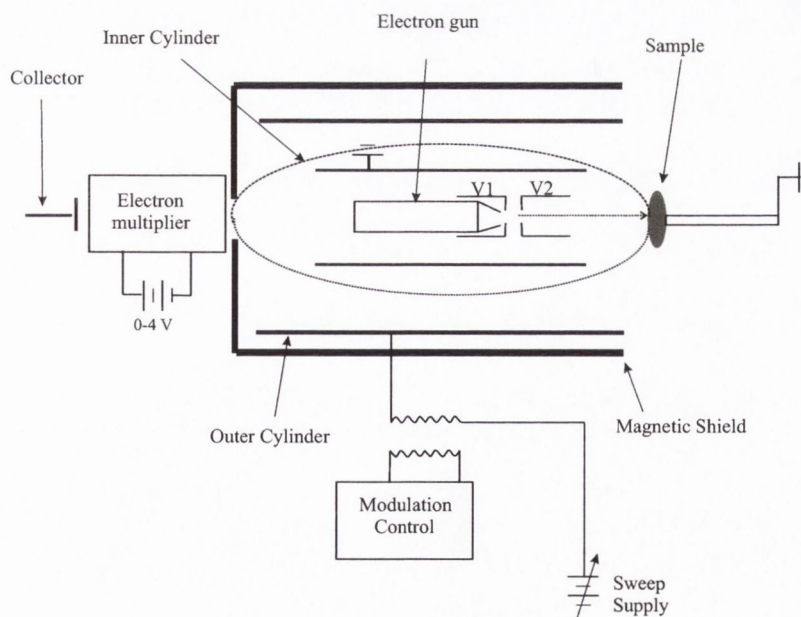
**Figure 4.6.** Schematic of the cylindrical mirror Auger analyser

accelerated through a potential $V_2$. The beam current can be varied by changing the extraction potential $V_1$. The electron gun is within two concentric cylinders. The inner cylinder is grounded, while a deflecting potential is applied to the outer cylinder. The deflecting potential is chosen such that only electrons of a particular energy will pass through the exit aperture. The analyser current is given by the number of electrons that pass through this aperture. Between the exit aperture and the collector an electron multiplier is used to amplify the analyser current. Primary electrons of known energy, which are reflected from the sample surface, are used to optimise the signal intensity to find the anlaysed spot, and calibrate the analyser. A full description of the operation of the Auger analyser can be found in [115]. A beam of energy of 3 keV was used for all measurements. The filament and emission currents were 3.2 A and 0.4 mA respectively, giving a target current of ∼8 $\mu$A. A SR 850 DSP lock-in amplifier from Stanford Research Systems [116] was used to output a 0.5 $V_{rms}$ sinusoidal signal of frequency 12 kHz to modulate the deflecting voltage applied to the outer cylinder. A lock-in sensitivity of 100 $\mu$V was then used to detect the Auger signal. The scan speed was always set to 1 eV/s.

## 4.7 Low Energy Electron Diffraction

The RVLO 900 four-grid reverse view optics view optics used in the experiments described here were manufactured by VG Microtech [117]. The optics mounted on a O.D. 200 mm CF custom elbow which is tilted at an angle of 30° to the horizontal. The sample sits in the transfer fork of a magnetic drive, which is grounded by a stainless steel braid to an OFHC copper block at the bottom of the LEED annex. The sample is rotated in this drive so that its surface faces the electron gun. Scattered electrons are collected by the grids and screen located behind the gun.
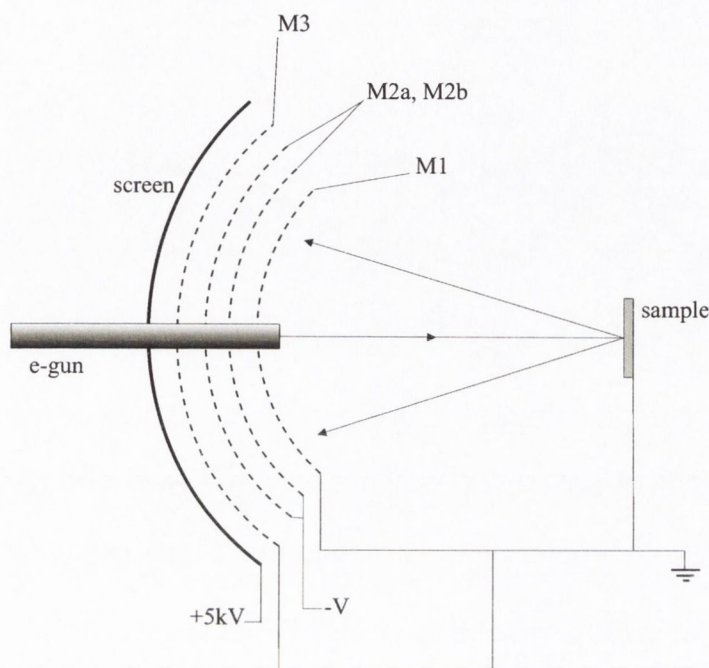
**Figure 4.7**. Schematic of the four-grid optics operating in LEED mode [96].

A schematic illustration of a four-grid LEED apparatus is shown in figure 4.7. It consists of an electron gun, providing a collimated beam of electrons, and a hemi-spherical fluorescent screen of which the diffracted electrons are observed. The grid nearest the sample, M1, is earthed, so that electrons scattered by the sample initially travel in field-free space. A negative potential is applied to the two centre grids, M2a and M2b, to suppress inelastically scattered electrons, while elastically scattered electrons are accelerated towards the phosphorescent screen by its +5 keV potential. The fourth mesh M3 is also grounded to reduce the field penetration of the suppressing grids by the screen.

## 4.8 The Room Temperature STM

The room temperature STM head is constructed of macor and comprises of a piezo tube scanner and a fine approach piezowalker, see figure 4.8. It is

based upon the system developed by Dr. S. H. Pan at the University of Basel, Switzerland [118]. In this design the sample is mounted on tip of a cylindrical
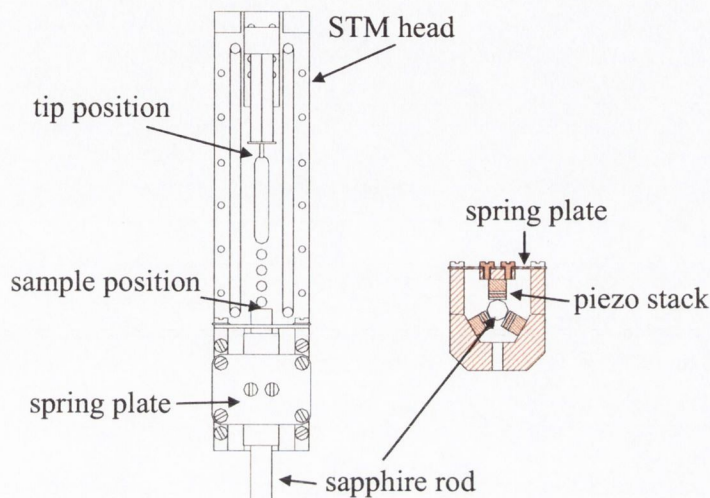


**Figure 4.8**. Schematic of a STM head similar to the RT-STM. A front view and a cross-section of the fine approach walker are shown.

polished sapphire rod. The rod is clamped between a set of of six piezo stacks, mounted in a triangular fashion. One pair of piezo stacks is spring-loaded against the sapphire rod. The motion of the sapphire rod occurs in two steps. First the stacks rapidly shear simultaneously so that the rod remains fixed as the stacks slip along the rod. All six piezo stacks are then allowed to relax simultaneously, such that the rod is dragged in the direction opposite to the original shear direction.

The piezoelectric tube scanner has four electrodes, of equal area, parallel to the axis of the tube. The inner electrode is grounded, so that when a voltage is applied to one of the outer electrodes the tube scanner bends away from that electrode. The scanner has a dynamic range of $\pm 13000$ Å in the z-direction and 20600 Å in the x- and y- directions. These directions were calibrated on Cu (100) monoatomic steps and HOPG atomic resolution images respectively. The STM head is isolated from vibrations by a two-stage spring system [101], which works in conjunction with the pneumatic dampers on the system frame.

The STM controller used for these experiments is a SCALA system by Omicron [109]. This controller allows the user to compensate for the thermal drift using a topographic feature of the STM image as a reference point. The accompanying software provides functions for data analysis. Data were also analysed using commercial software from Nanotech Electra S. L. [119].

### 4.8.1 STM Tips

Atomically sharp and stable tips are vital in order to obtain atomic scale resolution using STM. For this reason tungsten is the most widely used material for tip preparation. It is relatively hard, making is a stable probe material, and it can be electrochemically etched, allowing the preparation of atomically sharp tips [76].
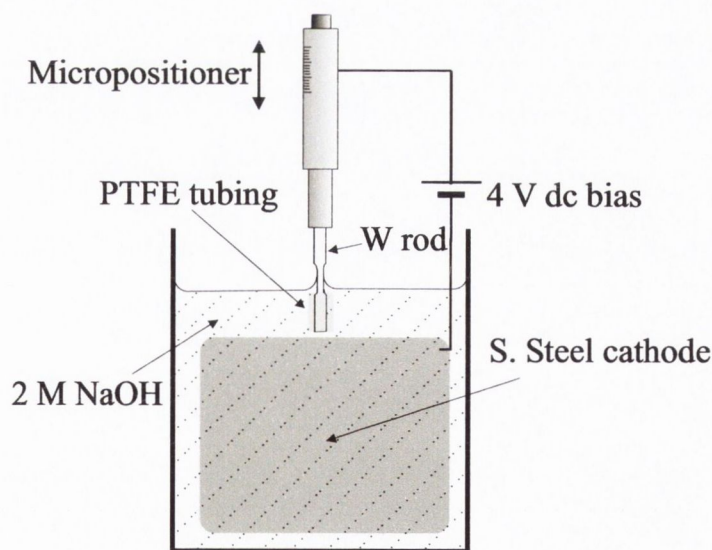


**Figure 4.9**. Electrochemical etching set-up used to prepare STM the W and MnNi tips.

For spin polarised SP-STM experiments it is necessary to use a material with a spin split DOS. Initial studies used bulk ferromagnetic tips [120]. However, the stray magnetic field of these materials can alter the magnetic properties of the sample one is attempting to characterise. One method to prevent this is

the evaporation of thin films of magnetic material onto W tips. However, this does not generally result in atomically sharp probes. The other is the use of antiferromagnetic materials, such as Cr or MnNi, which do not have a stray field [121].

STM images in this thesis were obtained with W and MnNi tips, which were usually prepared using a chemical etching procedure described in detail in [122].

W tips are prepared from 0.5 mm thick wire. The wire is cut into small rods and a small insulating PTFE tube is placed on the end of the rod. The rod is then clamped into a modified micrometer screw, which allows precise positioning of the rod in a beaker of 2.0 M NaOH solution. The W wire acts as the anode while a submerged metal foil acts as the cathode. Under an applied 4 V dc bias, chemical etching occurs at the air/electrolyte interface. The W oxidises to form soluble $WO_4^{2-}$, which flows away from the active etching region. This leads to a thinning of the wire at the interface region and eventually the submerged section of the wire falls off under its own weight. During the etching process the PTFE acts to physically restrict the active region [123] and also protects the tip that falls into the beaker. This tip etching setup is shown in figure 4.9. The tips are then rinsed with propan-2-ol, placed in tips holders and inserted into UHV. The tips are then etched with $Ar^+$ ions to remove the $WO_4^{2-}$ present from the chemical etching process. This process produces stable, atomically sharp tips.

MnNi tips are prepared in a similar manner to what described for the W tips. Cylindrical rods, of $\sim$ 0.5 mm, are prepared from an ingot. They are then chemically etched, again using the PTFE tubing, in 0.5 M HCl solution. Following chemical etching they are inserted into UHV are subjected to $Ar^+$ ion etching. These tips are again very sharp and stable. MnNi has a very high Néel temperature of $\sim$900 K, meaning it is suitable for room temperature SP-STM. The main problem that arises with the use of MnNi tips is that the composition of the apex is uncertain [20]. For example, the electrochemical etching could be

preferential to one of the elements, resulting in a Mn or Ni rich apex. Magnetic contrast has been achieved using these tips on the well characterised Mn/Fe(001) system [20].

# Chapter 5

# The $Fe_3O_4(110)$ Surface

## 5.1 Introduction

The low Miller index (001), (111) and (110) orientations of the magnetite surface have all been characterised by means of surface sensitive techniques such as AES [124], XPS [63], spin resolved PES [65] and angle-resolved PES [125]. The (001) and (111) orientations have also been extensively studied and characterised using STM-STS and DFT calculations [120, 126, 127, 128, 129, 130]. However, the (110) surface has been studied to a more limited extent even though it is, in principle, suitable for spin polarised STM measurements. That is because one of the two possible (110) planes contains both octahedrally and tetrahedrally coordinated irons, which are antiferromagnetically coupled.

In this chapter, the crystallographic structure of the $Fe_3O_4(110)$ surface is described, together with a description of the available literature.

## 5.2 The Surface of $Fe_3O_4(110)$

Magnetite crystals can be considered to be constructed by two different alternating planes perpendicular to the $\langle 110 \rangle$ directions, plane A and B, as shown in figure 5.1. The surface unit cell of the A-plane contains 4 oxygen atoms, 2
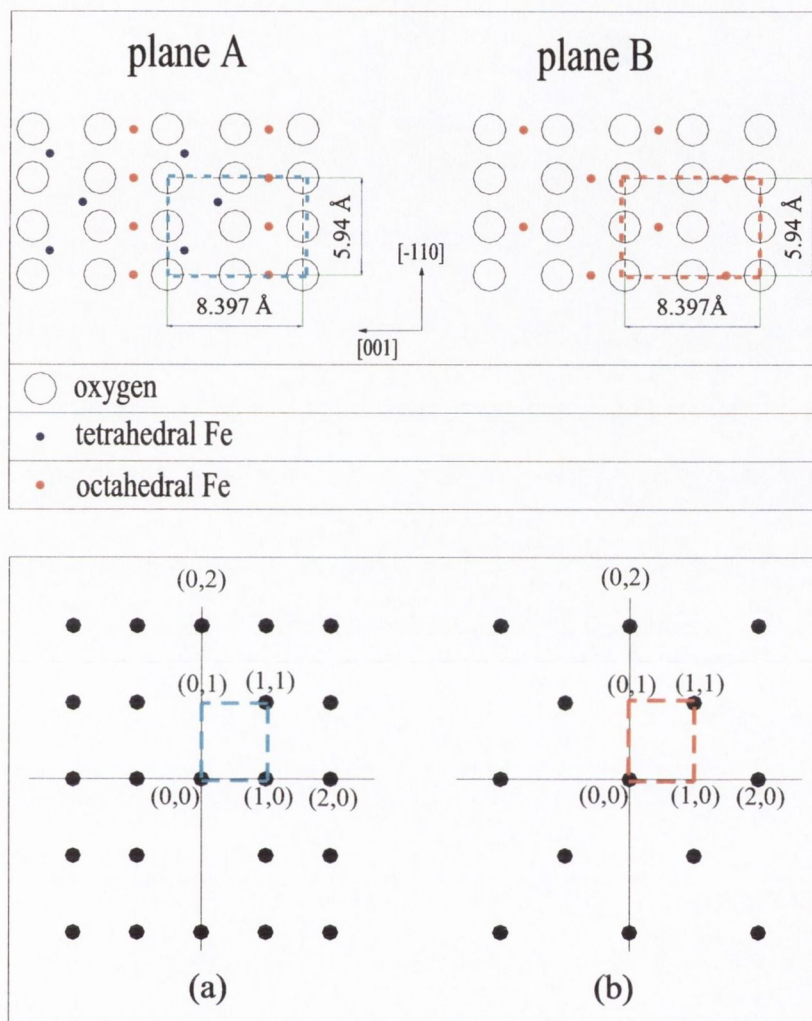
**Figure 5.1**. The two planes parallel to the $Fe_3O_4(110)$ surface. Dashed lines highlight the two surface unit cells. The two planes alternate along the $\langle 110 \rangle$ direction with a distance of 1.484 Å and are shifted by 1/4 of the unit cell lattice parameters along both the [001] and the [$\bar{1}$10] directions. The bottom part of the figure shows the expected LEED patterns for the A-plane (a), and the B-plane (b).

tetrahedral ($Fe_{tet}$) and 2 octahedral ($Fe_{oct}$) irons, while the one of the B-plane contains 4 oxygen atoms and 2 $Fe_{oct}$. These two planes alternate in the crystal with ABAB stacking sequence with lateral shift of 1/4 of the unit cell along both the [001] and the [$\bar{1}$10] directions, and are separated by 1.484 Å.

The A-plane has a mirror plane parallel to the [001] direction and a glide plane perpendicular to it. The B-plane has two perpendicular mirror planes along the

[001] and [$\bar{1}$10] directions. The LEED patterns expected for the two terminations are presented in the bottom part of figure 5.1, according to Oda [131]. The LEED mesh in (a) corresponds to the A-plane, it has the features of glide plane symmetry and there are missing spots in ($\pm$1,0) and ($\pm$3,0). A combination of the two planes on the surface would correspond to the pattern in (a) without consideration of intensity.

The two bulk terminations of the $Fe_3O_4$(110) surface are unstable. Two different models can explain why this surface must reconstruct: the electrostatic model (EM) and the electron counting model (ECM). The first, accounts for the electrostatic properties of solids and considers them as ionic surfaces. The second, determines the stability of a surface by redistributing the electrons between the dangling bonds in the surface atoms considering their electronegativity. They will be both described in the following sections.

## 5.2.1 The Electrostatic Model for Polar Surfaces

The electrostatic model (EM) of polar surfaces, proposed by Tasker [132], provides a classification of crystal surfaces which allows one to determine whether or not they will reconstruct. This model applies to ionic and partially ionic crystals, which can be classified in three categories, as shown in figure 5.2. Type I surfaces are neutral, since they contain cations and anions in stoichiometric ratio. The repeat units have zero charge Q and zero dipole moment $\mu$. Type II surfaces are charged, however, the repeat unit consists of three planes in a symmetrical configuration and, hence, there is no net dipole moment $\mu$ perpendicular to the surface. Type III surfaces have a non zero charge and a non zero dipole moment in each repeat unit of the crystal, which results in a diverging electrostatic energy at the surface. These type of surfaces are defined as polar surfaces, they are not stable and cannot exist as bulk terminations. In these cases the surface must reconstruct. The reconstruction can be obtained by an ordered arrangement of

vacancies, in such a way that the charge of the surface plane is halved. This results in the cancellation of the electrostatic energy due to the surface layers. Also the presence of contaminants or a compensation by a redistribution of the electrons in the surface atoms, can result in the cancellation of the electrostatic surface energy [133].
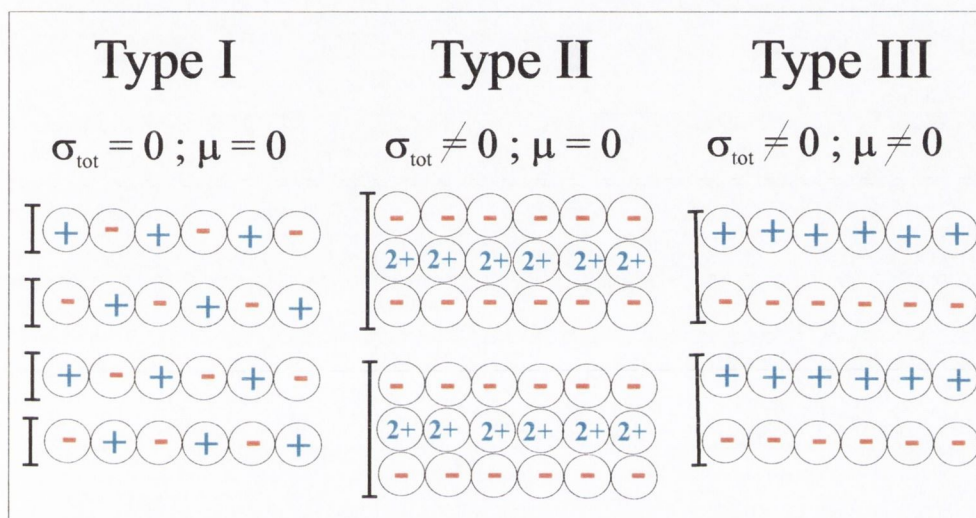


**Figure 5.2.** The electrostatic model of polar surfaces. Repeat unit of each denoted by a bracket. Type I: repeat unit contains equal numbers of anions and cations in a single plane, each plane has zero charge. Type II: planes are charged, however, the dipole moment perpendicular to the planes because the planes are in a symmetrical configuration. Type III: planes are charged and the repeat unit is not symmetrical. Each repeat unit has a net dipole moment perpendicular to the surface.

The $Fe_3O_4(110)$ surface can be described as a type III, and therefore as a polar surface [134]. Both the A and B planes are charged. The oxidation state of the different atoms are $Fe_{oct}$ = +2.5, $Fe_{tet}$ = +3 and O = -2. Considering the surface unit cells it is possible to evaluate a +3 charge for the type A and a -3 charge for the B. Therefore there is a net dipole moment in the repetitive unit perpendicular to the (110) directions formed by the two planes. As the crystal is built up, the dipole moment of the crystal increases and the electrostatic energy of the surface becomes infinite. In order to minimise it, the surface layers only must reduce their charge to +1.5 for a A-plane and -1.5 for a B-plane. In order

to do that, the surface must reconstruct.

## 5.2.2 The Electron Counting Model and the Autocompensation Principle

The electron counting model (ECM) was developed by Pashley in the case of semiconductors GaAs and ZnSe [135] and was extended to oxides by LaFemina [136]. This model considers the dangling bonds of the atoms at the surface and is based on the autocompensation principle. This states that the lowest surface energy is reached when the dangling bonds of the electronegative elements are full and the dangling bonds of the electropositive elements are empty. The ECM does not determine the final reconstruction, but any successful structural model must satisfy the ECM.

The two Fe$_3$O$_4$(110) terminations have 3 types of atoms, i.e. Fe$_{oct}$, Fe$_{tet}$ and O, engaged in 4 different bond configurations, see table 5.1. The Fe$_{oct}$ atoms have 6 bonds to the surrounding O atoms and carry a formal oxidation state of +2.5, which results in $2.5/6 = 5/12$ e$^-$ per bond. The Fe$_{tet}$ atoms have 4 bonds with the surrounding O and a formal oxidation state of +3, which results in $3/4$ e$^-$/bond. The O atoms are bound with either Fe$_{oct}$ and Fe$_{tet}$, and a formal oxidation state equal to -2. To fill the bond with a Fe$_{oct}$, an O shares $(2 - 5/12) = 19/12$ e$^-$/bond. To fill the bond with a Fe$_{tet}$, an O shares $(2 - 3/4) = 5/4$ e$^-$/bond.

| atomic specie | oxid. state | bonds | e$^-$/bond |
|---|---|---|---|
| Fe$_{oct}$ | +2.5 | 6 | $2.5/6 = 5/12$ |
| Fe$_{tet}$ | +3 | 4 | $3/4$ |
| O$_{oct}$ | -2 | - | $2 - 5/12 = 19/12$ |
| O$_{tet}$ | -2 | - | $2 - 3/4 = 5/4$ |

Table 5.1. The 3 different type of atoms and 4 different types of bonds occurring on the Fe$_3$O$_4$(110) surface, according to the electron counting model. The number of electrons per bond are calculated for the different cases.

In the A-plane, there are 4 $O_{oct}$ dangling bond with $Fe_{oct}$, for a total of (4 x 19/12)= $6.\bar{3}$ $e^-$, (where in the case of O, $_{oct}$ and $_{tet}$ mean that the O is bonded with a $Fe_{oct}$ or $Fe_{tet}$). There are also 2 $Fe_{oct}$ with 4 dangling bonds, for a total of (4 x 5/12)= $1.\bar{6}$ $e^-$, and 2 $Fe_{tet}$ with 2 dangling bonds, for a total of (2 x 3/4)= 1.5 $e^-$. This results in $(6.\bar{3} + 1.\bar{6} + 1.5)$= 9.5 $e^-$. Since there are 4 oxygen's orbitals to be filled with 8 electrons, there is an excess of 1.5 $e^-$ on this surface termination.

In the B-plane, there are 4 $O_{oct}$ and 2 $O_{tet}$ dangling bonds, for a total of (4 x 19/12)+(2 x 5/4)= $8.8\bar{3}$ $e^-$, and 4 $Fe_{oct}$ dangling bonds, for a total of $1.\bar{6}$ $e^-$. This results in $(8.8\bar{3} + 1.\bar{6})$= 10.5 $e^-$. Since there are 6 oxygen's orbitals to be filled with 12 electrons, therefore there is a deficit of 1.5 $e^-$ on this surface termination.

Both models agree on the fact that the two bulk terminations of the $Fe_3O_4(110)$ surface are not stable. The A-plane unit cell is found positively charged +3 within the EM and cannot place 1.5 electrons in the oxygen's dangling bonds, according to the ECM. These electrons correspond to the charge that the surface needs to gain in order to be stable in the EM. Similar conclusions, but with the sign inverted, can be drawn for the B-plane. In this case the unit cell is described as -3 charge within the EM and has a vacancy of 1.5 electrons in the oxygen's dangling bonds, according to the ECM.

## 5.3   Previous Studies of the $Fe_3O_4(110)$ Surface

Comparatively few papers have been published in relation to surface studies of the $Fe_3O_4(110)$. The papers by Jansen *et al.* [137, 138, 139] present AES, LEED and STM results, along with some STS measurements at room temperature of $Fe_3O_4$ single crystal and thin films. After cleaning the surface with repetitive $Ar^+$ etching and UHV annealing cycles, the surface was annealed in $1x10^{-6}$ mbar of $O_2$ at 850-1200 K. Regular rows were imaged running along the $[\bar{1}10]$ direction with

rows separated by ~25 Å. This result is in agreement with the reported LEED patterns, showing a p(1x3) reconstruction and a periodicity of 3 Å along the rows. They were also able to image some areas where the width of the rows was different than 25 Å, either 17 Å or 34 Å. They proposed a model for the reconstruction that contains $\alpha - Fe_2O_3 - like$ layers, which also explains the conductivity gap found in the STS spectra. However, they also stated that their model should be treated with some reserve. Oda *et al.* [131] annealed their samples at a lower temperature of 840 K and performed a LEED study of the surface, finding a p(3x1) reconstruction, in disagreement with Jansen. It has to be emphasised that Oda claims their crystal to be purer, having a higher Verwey temperature, which allows them to obtain a clean surface at lower annealing temperature. They suggested that this could be the reason for the different reconstruction observed. They also proposed a possible model based on the LEED patterns, which includes $Fe_{tet}$ and $Fe_{oct}$ on the topmost surface layer. However, this represents only one of the possible structures which would agree with the experimental evidence. Better STM images were obtained by Maris *et al.* [140], who annealed $Fe_3O_4$/MgO thin films at 1000 K for a short time, either in UHV, or in $2x10^{-6}$ mbar of $O_2$. Imaging the surface with a clean blunt W tip, they measured a periodicity of 3 Å along the rows and 2.1 Å in the [001] direction and concluded that they were imaging a bulk termination, precisely the A-plane. They claimed to image not only iron atoms, but also oxygen atoms. Although this contradicts previous experimental [63, 64] and theoretical studies[9, 10], which show that the $p$ states of the oxygen atoms lie well below the Fermi energy (see also section 2.4), the presence of $Mg^{2+}$ ions, diffusing from the substrate to the surface during annealing, can influence the position of the O(3s), which can then be probed by STM. This agrees with electronic structure calculations performed by Boer *et al.* [141], who suggested that the conduction band of MgO has predominantly O(3s) character. By means of AES Maris *et al.* detected a high concentration of Mg which was not observed

on top of the surface by STM. They therefore suggested a model where the bulk A-termination is stabilised at the surface by the presence of Mg atoms placed below the topmost surface layer. Since working on the same topic, a collaboration has been established between our group and Maris' group. The mutual exchange of, not only thin film samples, but also STM tips, data, ideas and opinions, has been abundant and still continues in the hope that the joint effort will help to conclusively characterise the surface of Fe$_3$O$_4$(110).

# Chapter 6

# Study of the (110) Surface of Fe$_3$O$_4$ Single Crystal

## 6.1   Introduction

In this chapter experiments carried out on a single crystal sample of magnetite are described. First, the characterisation of the sample by means of X-ray diffraction and measurement of the Verwey temperature is presented. Then, AES, LEED and STM-STS experimental results are described for the clean (110) surface and for different preparations of the surface consisting of high temperature annealing of the sample in oxygen atmosphere, and high temperature annealing of the sample in UHV. Models of the surface termination for the different cases are put forward, based on the experimental evidence.

## 6.2   Sample Characterisation

The magnetite single crystal sample used for these measurements was grown using the floating zone technique by Prof. Y. M. Mukovskii [85]. The ingots were cut perpendicular to the ⟨110⟩ direction and aligned to an accuracy of ±0.5°. The
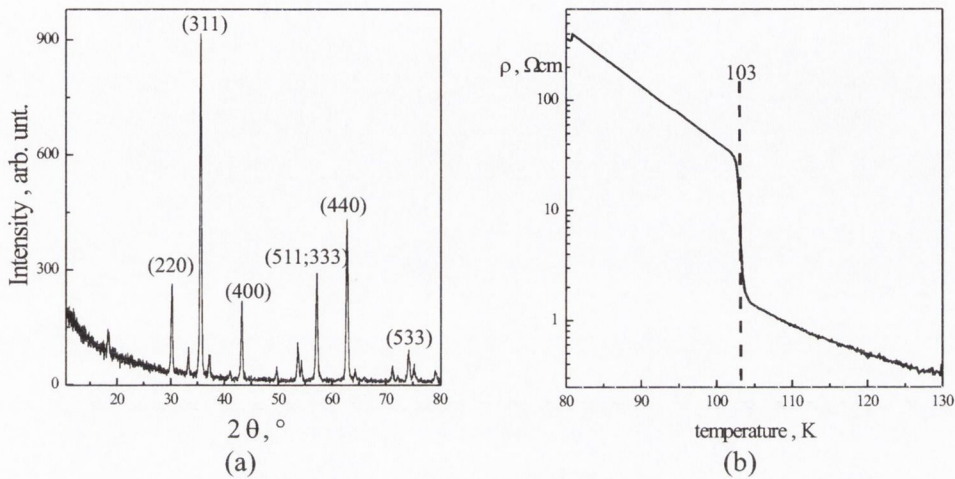
**Figure 6.1.** a) X-ray diffractogram of the single crystal sample used for the experiments. The pattern is found to be in good agreement with the expected crystallographic structure of magnetite. b) Resistivity versus temperature curve for the magnetite single crystal sample showing a Verwey transition of 103 K.

X-ray diffraction pattern of the sample was taken using a powder diffractometer. A Cu K$\alpha$ wavelength was used, corresponding to $\lambda$=1.541 Å. The diffractogram obtained, shown in figure 6.1a, shows the diffraction peaks characteristic of the crystallographic structure of magnetite [129].

The resistivity versus temperature measurements carried out on this sample yielded a Verwey temperature of 103 K, as shown in figure 6.1b. For non-contaminated, stoichiometric magnetite crystals, a Verwey temperature of $\sim$120 K is expected. If the crystal is cation deficient or contaminated, there is a change in the stoichiometry that pushes the Verwey temperature to lower values and, eventually, it disappears completely [142]. Therefore, the detection of the Verwey transition is the best test to confirm that the crystal is good quality magnetite.

## 6.3 Annealing of the Surface at 850 K

### 6.3.1 AES and LEED Analysis

The (110) surface of the $Fe_3O_4$ sample was hand polished with diamond paste of decreasing grain size down to a grain size of 0.25 $\mu$m. The sample was cleaned with ethanol using an ultrasonic bath and then clamped in a Ta/Mo sample holder before being introduced in to the UHV system. AES analysis of the sample showed a high concentration of contaminants such as C, S, Ca and K. In order to remove them, the surface was $Ar^+$ etched with 500 eV ions for 15 minutes and annealed in UHV in the resistive heater at 850$\pm$50 K for 150 minutes. After



(a)                                   (b)
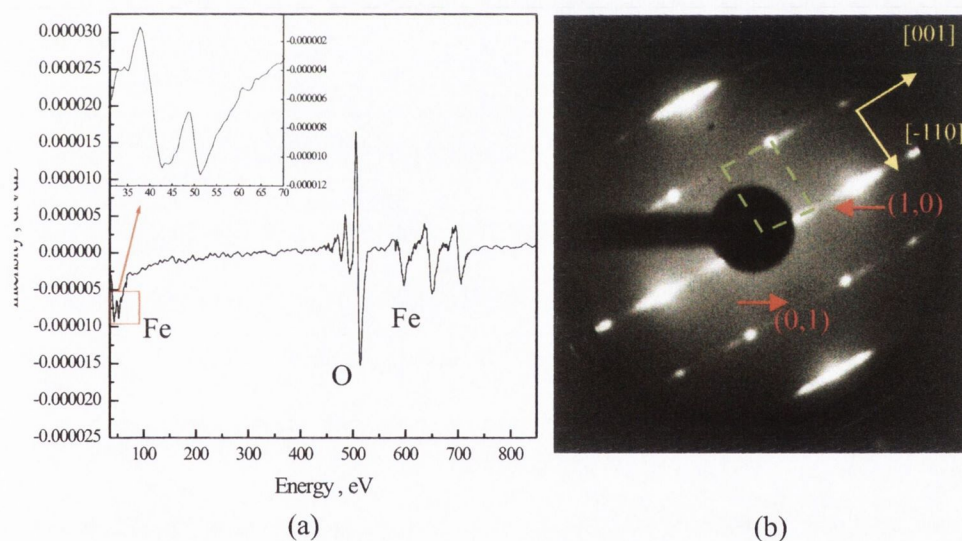
**Figure 6.2.** a) Typical AES spectrum of the $Fe_3O_4$ single crystal obtained after the cleaning procedure. It shows the oxygen peaks at 509 eV, the iron peaks centred around 650 eV, and, in the inbox, the low energy iron peaks at 43 eV and 52 eV. These peaks are indicative of an iron oxide b) LEED pattern of the $Fe_3O_4$ single crystal obtained with an energy of the primary beam of 45 eV after the cleaning procedure. The unit cell is indicated in green while the crystallographic directions are shown in yellow. Also indicated are the positions of the missing spots in (1,0) and (0,1).

several etching and annealing cycles, a clean surface was obtained, as confirmed by AES analysis. Annealing in oxygen was carried out at $2.0x10^{-6}$ mbar at 850$\pm$50

K for 15 minutes prior to the final UHV cleaning cycle, in order to re-establish the O/Fe ratio of the surface to that expected for magnetite, i. e. 1.5-1.7 [143]. A typical AES spectrum is shown in figure 6.2a. It shows the oxygen peak at 509 eV, the iron peaks centred around 650 eV, as well as the low energy iron peaks at 43 eV and 52 eV. These peaks are indicative of an iron oxide [124, 144, 145, 146]. The concentrations of the contaminants were determined to be lower than 1.4%±0.5, and mainly comprised Ca at 1.0%±0.5. The O/Fe ratio is 1.5. Repetitive etching and annealing cycles were performed in order to completely eliminate the contaminants, with no success. However, the contaminants found by the AES spectra are present in very low concentrations (less than 1.5%) and a surface reconstruction due to their presence is not considered likely.

A typical LEED pattern obtained for this surface is presented in figure 6.2b. The unit cell corresponding to the 8.4x6 $\text{Å}^2$ surface net of the $Fe_3O_4(110)$ surface, is highlighted in green. The pattern was taken using a primary beam energy of 45 eV and is comparable to the pattern expected for a B-plane termination, which has been described in section 5.2. In particular, the absence of the diffraction spots in (±1,0) and (0,±1), as indicated in the figure by the red arrows, is a strong indication that the surface retains the symmetry of the B-plane.

### 6.3.2 STM Measurements

STM measurements of the surface were always performed using a W tip unless otherwise specified. Terraces elongated along the $[\bar{1}10]$ direction were found on the surface, as illustrated in figure 6.3. The corrugation of the surface was very high, with consecutive terraces often separated in height by 1-2 nm. A zoom in on one of the terraces shows steps equal to, or multiple of 3 Å, which corresponds to twice the minimum separation between two consecutive planes in the bulk. This suggests that, following this preparation procedure, a surface comprising one of the bulk terminations is dominant on the surface. Small area scans show

the presence of rows on the surface running along the [$\bar{1}$10] direction, see figure 6.4. These rows exhibit a periodicity of 35 Å along the [001] direction, as shown in the line profile in figure 6.4b.



(a)                                          (b)
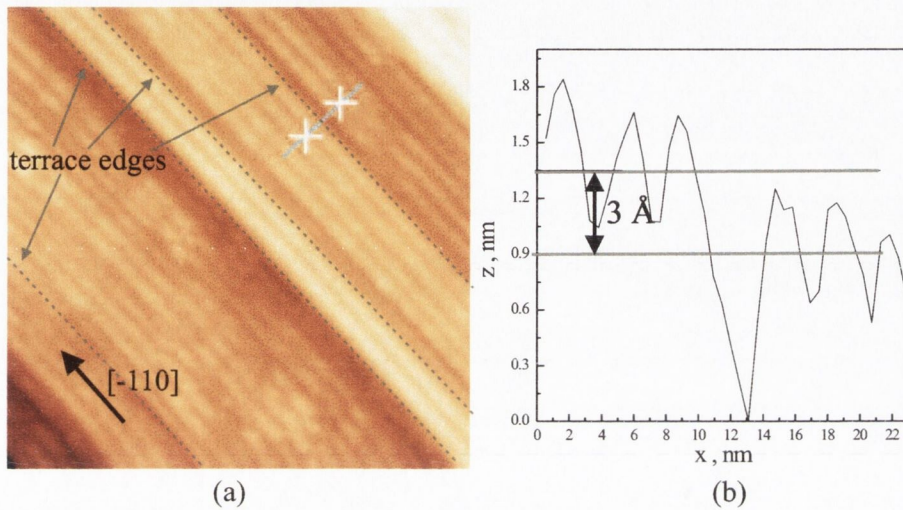
**Figure 6.3**.  a) STM image 100x100 nm$^2$ taken with a W tip of the single crystal sample taken at I$_t$=0.10nA and V$_b$=-1.0V. The image shows the presence of terraces elongated along the [$\bar{1}$10] direction. b) Line profile that shows two terraces separated by a step of 3 Å.



(a)                                          (b)
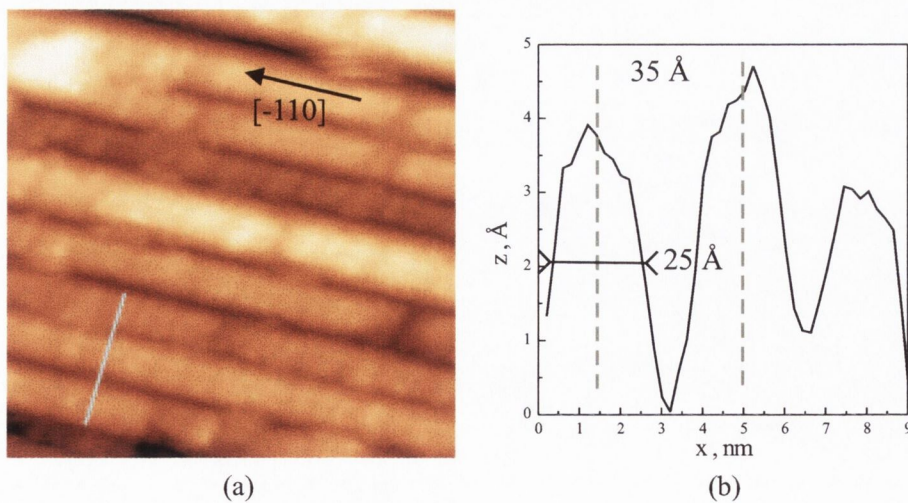
**Figure 6.4**.  a) STM image 25x25 nm$^2$ obtained with a I$_t$ = 0.050 nA and a V$_b$ = -1.0 V. The image shows the rows running along the [$\bar{1}$10] direction. b) Line profile of the rows that shows a periodicity of 25 Å.
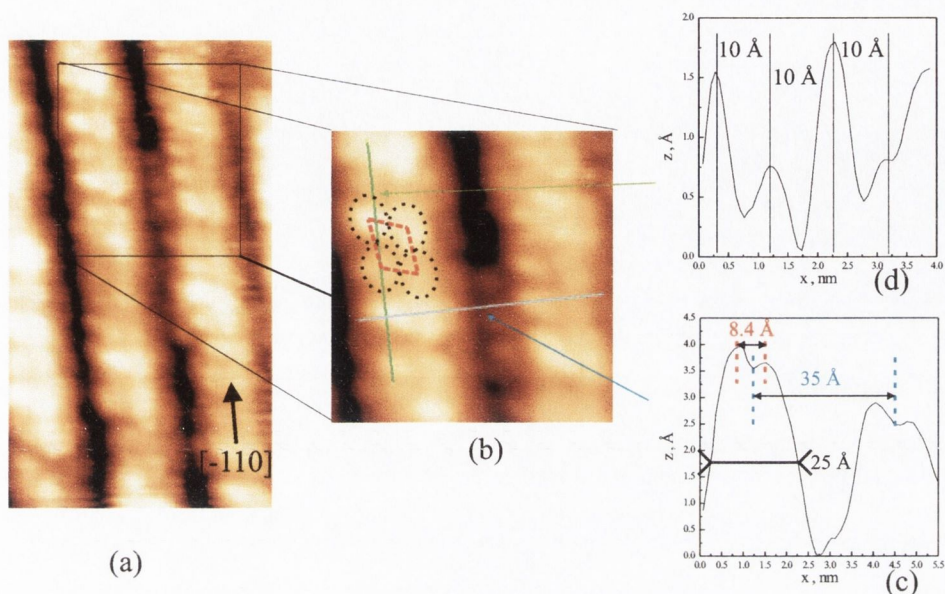
**Figure 6.5**. a) STM image 8.0x14 nm$^2$ obtained with a I$_t$ = 0.05 nA and a V$_b$ = -1.5 V. The rows running along the [$\bar{1}$10] direction are visible. b) Zoom in on the image that shows that some structure is resolved on top of the rows. These features are too large to be atoms, as indicated by the ovals. The repeat unit is indicated in red. c)A line profile that shows the splitting of the 35 Å rows along the [001] direction. d) Atomic corrugation along the [$\bar{1}$10] direction.

Some structure was resolved on top of the 25 Å rows, as shown in figure 6.5. These features exhibit a periodicity of 10±0.5 Å along the rows and 8.4±0.5 Å in the direction perpendicular to the rows. Unfortunately, it was not possible to resolve these features with atomic resolution.

Using the available information, a model of the surface reconstruction is proposed in the next section.

### 6.3.3    A Model of the Surface Reconstruction

It is reasonable to assume, in consideration of the LEED results, that the reconstruction is derived from a B-plane. A B-plane is described within the ionic model as -3 charged and a reduction of the charge to -1.5 is required for the surface reconstruction to be stable (as previously explained in section 5.2). This

could be simply achieved by desorption of oxygen atoms, which would lead to a reduction of the surface and could result to a rearrangement of the iron atoms on the surface. The desorption of oxygen would be favoured by the annealing of the sample in UHV.

The simplest model that can be proposed, which would agree with the experimental results, consists of a reconstruction stabilised by a missing rows structure. In the model, the 25 Å rows parallel to the $[\bar{1}10]$ direction are composed of two layers, see figure 6.6b. The bottom layer contains three unit cells aligned along the $[001]$ direction, belonging to the A-plane, that gives the 35 Å periodicity measured with the STM. The topmost layer consists of two B-plane unit cells, which are shifted by either 1/4 or 3/4 of the cell parameter in the $[001]$ direction. This is in agreement with the presence of a glide plane for the B-termination and is also evident from the experimental STM images, see figure 6.6a, where in some areas a wave-like arrangement of the structure is found. These rows are separated by some missing rows composed by 1 A-type unit cell and by 2 B-type unit cells on top, as shown schematically in figure 6.6b.

In figure 6.6c the schematic model of the surface reconstruction is shown. In the figure, the irons belonging to the A-plane in the second surface layer are indicated in light blue, while the irons in the topmost layer are indicated in red. The small circles are oxygen in the second layer (hollow) and in the topmost layer (filled). Within this model, the structures resolved on the surface are formed by 7 near $Fe_{oct}$, as indicated in the figure 6.6c by the red ovals. These structures are shifted by 1/2 along the $[\bar{1}10]$ direction and by 1/2 along the $[001]$ direction, relative to one another, in agreement with what was found in the STM measurements. This is indicated in the image by the 1/4 or 3/4 shift with respect to the second layer. The distance between $Fe_{oct}$ in the top layer along the $[001]$ direction corresponds to the distance of the $Fe_{oct}$ in the B-plane and is 8.4 Å. Along the $[\bar{1}10]$ direction, the direction of the rows, the periodicity

(a)

(b)

(c)

3/4 shift

1/4 shift

missing row

25 A

O top layer

Fe$_{oct}$ top layer

O second layer

Fe$_{oct}$ second layer

Fe$_{tet}$ second layer

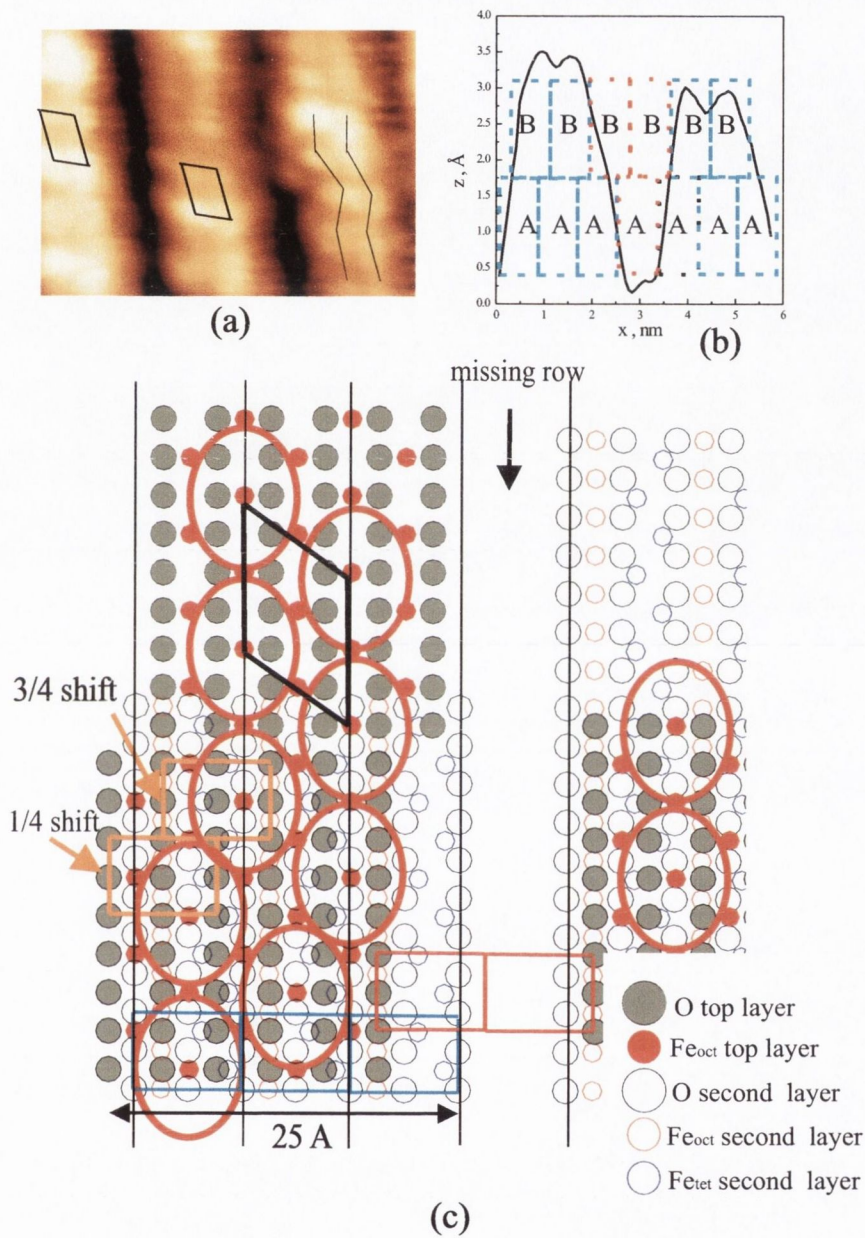**Figure 6.6**. a)STM image of the rows with the structure resolved. The repeat unit is indicated by the parallelepiped. b) Line profile of the rows imaged with a schematic of the model superimposed. The rows are considered to be formed by three unit cells of the A-plane at the bottom and two unit-cell of the B-plane at the top of the row. c) Atomic model of the structures present at the surface which considers the 2 surface layers.

of the structure is 10 Å, and there are 3 aligned irons, which are separated by 5±0.5 Å. This corresponds only to a minor relaxation of the irons from an original separation of 6 Å in the B-plane within the bulk.

The inability to experimentally image the surface atoms can be attributed to charge localisation between the seven nearest neighbours atoms considered within one oval. This would gives rise to the corrugation observed in the STM images but somehow prevents obtaining atomic resolution. However, it is not possible, at this stage, to formulate a more detailed hypothesis to explain why it was not possible to achieve better resolution. More experiments have to be carried out and more results are needed for a complete understanding of the surface reconstruction.

## 6.4   High Temperature Annealing in Oxygen

After annealing in UHV at 850 K, the magnetite sample was placed in the e-beam heater, and annealed in oxygen pressure of $2.67 \times 10^{-6}$ mbar, at 1100±50 K for 2 hours. AES analysis shows an increase of the O/Fe ratio to 1.62. This value still agrees with the presence of a magnetite phase on the surface after oxidation [143].

### 6.4.1   AES and LEED Analysis

Two LEED patterns obtained at 48 eV and 116 eV are shown in figure 6.7. Comparing these mesh with the one obtained for the surface annealed at 850 K in UHV, (at 45 eV), two differences are evident: i) the spots in (±2,0) and (±0,2) are brighter and ii) there are spots, for example in (±1,0) and (1,2), which were not present in the previous case. The first point can be simply attributed to the scattering of oxygens on the surface, due to their larger volume compared to the iron atoms. However, the appearance of a spot in (±1,0), and (1,2) for example, agrees with the possibility that the surface reconstruction contains both the A-

(a)  (b)
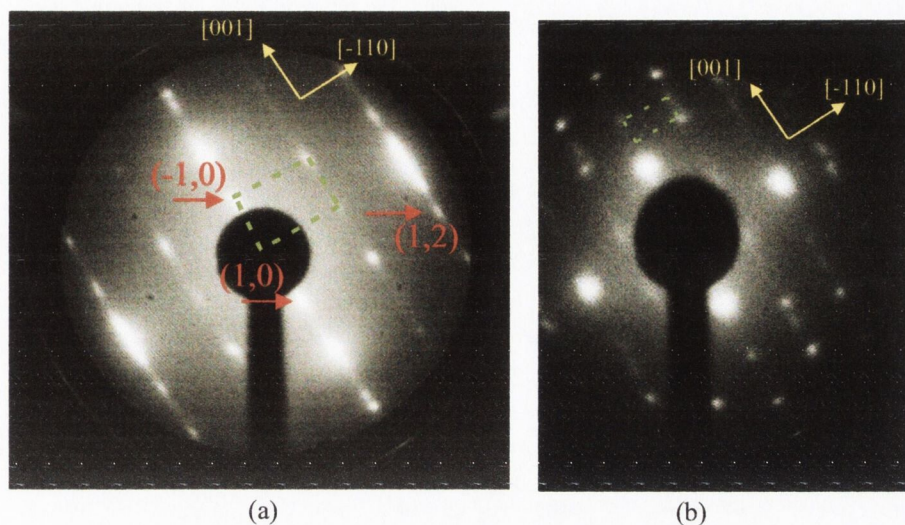
**Figure 6.7**. a) LEED meshes of the single crystal sample after annealing in $O_2$ at 1100 K, obtained at an energy of 48 eV. b) LEED pattern obtained with an energy of 116 eV. The unit cells are indicated in green. The 2 spectra show the presence of spots for example in $(\pm 1,0)$ and $(1,2)$ as indicated by the red arrows.

and the B-termination (see section 5.2).

## 6.4.2  STM Measurements

STM experiments on this surface were carried out using W tips. Terraces elongated along the $[\bar{1}10]$ direction were, once again, found to cover the surface, see figure 6.8. Consecutive terraces were most often separated by 3 Å, or integer multiples. However, the smallest step found corresponds to 1.5 Å, even though in this case, the terraces were always found to be very narrow, as shown in figure 6.9. In this figure, the terrace indicated A is smaller than the terraces indicated with B. In general, larger areas corresponding to the B-plane were found, which would suggest that annealing in oxygen results in one of the two terminations, the areas labelled B in the figures, being more favorable than the other.

In figure 6.9b, a zoom-in on one of the terrace is shown. The corrugation of these terraces is very small, $\sim 0.75$ Å, indicating a flat terrace. On this, rows are resolved, which are oriented along the $[\bar{1}10]$ direction and are regularly separated
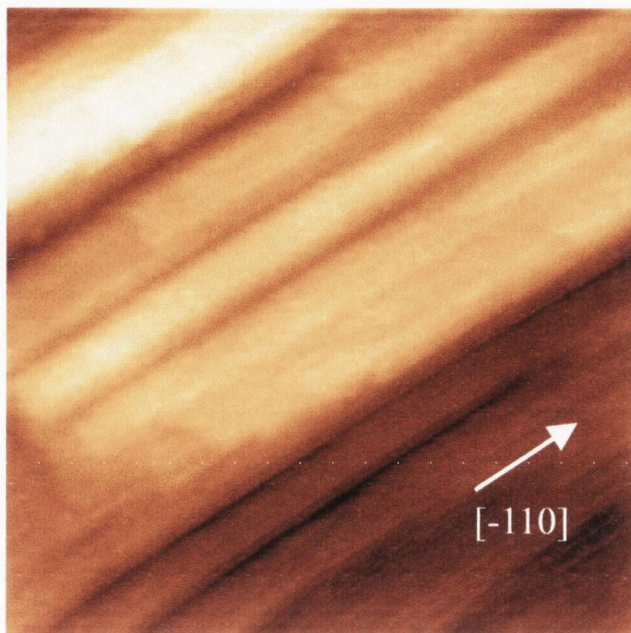
**Figure 6.8**. a) STM image 500x500 nm$^2$ of the single crystal sample taken at I$_t$=0.05 nA and V$_b$=-1.5 V. Large terraces are found on the surface elongated along the [$\bar{1}$10] direction

by 4.5±0.5 Å.

The terraces labelled A, even if smaller, also show rows parallel to the [$\bar{1}$10] direction, but these rows are separated by $\sim$ 8.2 Å, as indicated in figure 6.9b.

The difficulty in imaging the atoms themselves can be attributed to the fact that annealing in oxygen at high temperature, causes most likely the adsorption of oxygen on to the surface. A model for the surface reconstruction is introduced in the next section, after consideration of the experimental results.

### 6.4.3   A Model of the Surface Reconstruction

First of all, as already mentioned, the high temperature annealing of the surface in oxygen, produces a more uniform and flatter surface. Both terminations are present on the surface, but one of them is more favourable than the other. This termination cannot be conclusively determined by LEED measurements, for while the diffraction pattern is similar to what is expected for the A-termination, the
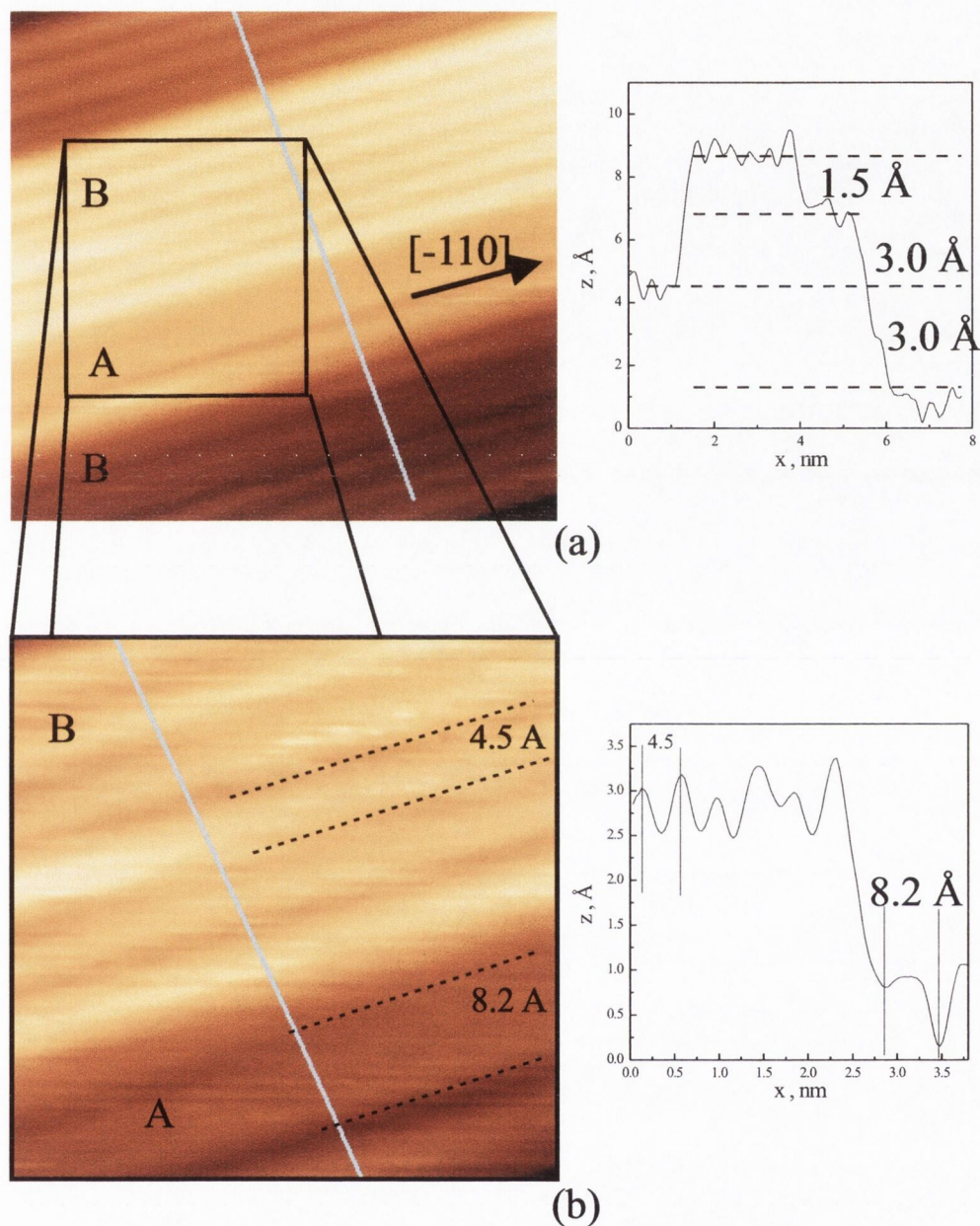
**Figure 6.9**. a) STM image 82x76 $\text{Å}^2$ of the single crystal, obtained at a $I_t$=0.10 nA and $V_b$= -1.0 V, and corresponding line profile that shows that terraces are separated by steps generally equal to 3 Å in height. Terraces separated by 1.5 Å are sometimes found, but, as shown in the figure, they are relatively small. In the figure, A and B indicate the two possible terminations that are imaged on the surface. b) Zoom-in on the previous image and relative line profile that shows that the rows on the top terrace are separated by 4.5 Å. It can also be seen that the periodicity in the small terrace, labeled as B, is 8.2 Å.

observed pattern may also be expected for a combination of the two terminations (as already explained in the section 5.2). However, it is reasonable to assume that annealing in oxygen stabilises the B-termination, which is oxygen rich, (O:Fe = 2:1), better than the A-termination, (O:Fe = 1:1). The rows imaged on the terraces labeled with B, separated by $\sim$4.5 $\pm$0.5 Å, are very similar to each other and this also suggests a B-termination. Only $Fe_{oct}$ can be found in the B-plane unit cell, which are the ones responsible for the electrical conductivity in $Fe_3O_4$. They are aligned in rows parallel to the [$\bar{1}$10] direction, separated by 4.2 Å. This is presented in figure 6.10a, that shows an STM image with the 4.5 Å rows and the model proposed. In the model, it is assumed that the $Fe_{oct}$ are separated by 4.5 Å instead of 4.2 Å. The two values are very close and within the experimental error.

If in the terraces labeled as A, an A-termination is supposed, rows parallel to the [$\bar{1}$10] direction, would also be expected and, since only $Fe_{oct}$ are responsible for conduction, the separation should be closer to 8.4 Å, corresponding to their periodicity in the perpendicular direction. This is shown in figure 6.10b, where the STM image showing the small terrace previously labelled as A, is compared with a model of the possible A-termination. Although this terrace is very small, it shows 2 dark lines separated by $\sim$ 8.2$\pm$ 0.5 Å. These dark lines would correspond, in the model, to the $Fe_{tet}$, because they are expected not to be conducting unlike the $Fe_{oct}$, which are found in the centre of the row.

Furthermore, it is possible, considering the preparation procedure, that oxygen is adsorbed on top of the surface, between the $Fe_{oct}$ or the $Fe_{tet}$, see figure 6.10c. This would explain why it was not possible to achieve atomic resolution. In fact, there are no oxygen bands near the Fermi level, in $Fe_3O_4$ single crystal, as already explained earlier (see section 2.4), which means that tunneling is established between the tip and the Fe states. The presence of the oxygens on top of the surface could result in a hybridisation of the oxygen and iron's orbitals,
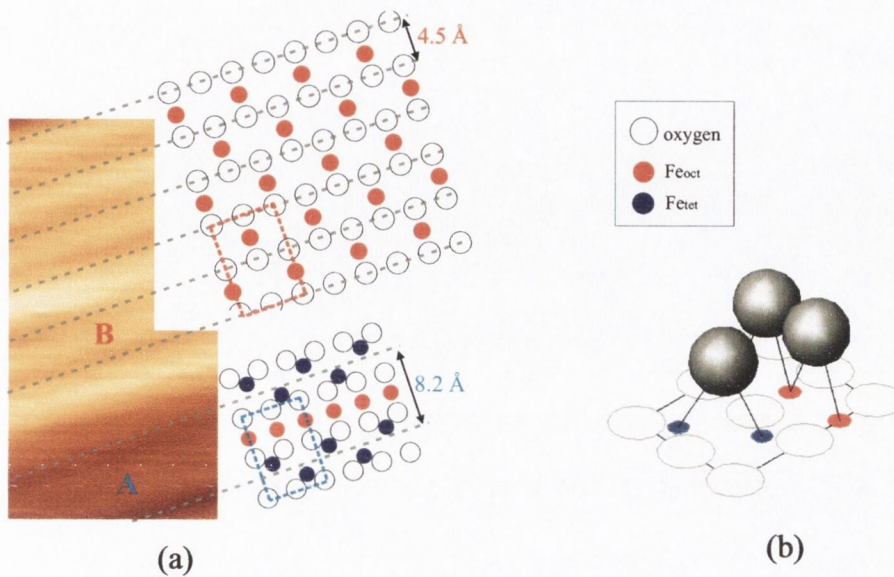
**Figure 6.10.** a) Model proposed for the surface termination observed on the $Fe_3O_4(110)$ single crystal sample after annealing in oxygen at high temperature. The two terminations are found on the surface, and are labeled as A and B. b) 3-D view showing the adsorption of oxygen atoms on top of the rows, which could be responsible for the inability to achieve atomic resolution.

impeding the achievement of atomic resolution.

## 6.5 High Temperature Annealing in UHV

After the annealing in oxygen, the sample was placed in the $e^-$-beam heater and annealed in UHV at $\sim$1x10$^{-9}$ mbar, at a temperature of 1100$\pm$50 K for 30 minutes. This treatment was performed 4 consecutive times giving an annealing time of 2 hours in total.

### 6.5.1 AES and LEED analysis

The AES spectrum is presented in figure 6.11a. It shows the peaks characteristic of an iron oxide but the O/Fe ratio has decreased down to a value of 1.44. This value is below the minimum value of 1.5 expected for a $Fe_3O_4$ phase on the surface [143]. Therefore the possibility that part of the surface, or all of

it eventually, changes from a $Fe_3O_4$ phase to an other iron oxide cannot be ruled out.



(a)                                         (b)
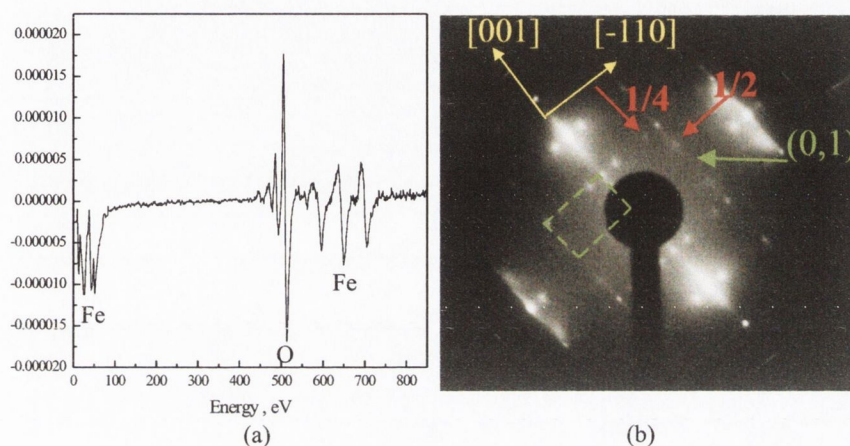
**Figure 6.11**. a) AES spectrum obtained for the magnetite single crystal after high temperature anneal in UHV. The O/Fe is lowered down to 1.44. The spectrum confirms that the surface still consists of an iron oxide. b) LEED pattern obtained for the same case at an energy of the primary bean of 39 eV. The unit cell is indicated in green, and the p(4x2) superstructure in red.

The LEED patterns obtained in the case of annealing in UHV at 1100 K, were found to be very different from those presented in the two previous cases. It can be seen from figure 6.11b, that the (0,1) spots are absent once again, as indicated by the green arrow in the figure. Therefore a reconstruction of the A-termination, or eventually of a combination of both terminations, is expected. The LEED mesh also shows fractional spots present at 1/2 along the $[\bar{1}10]$ direction and 1/4 along the [001]. This p(4x2) pattern suggests that the periodicity along the [001] direction should be equal to 8.4x2=16.8 Å, while the periodicity along the $[\bar{1}10]$ is expected to be equal to 6x4=24 Å.

## 6.5.2 STM-STS Measurements

### W tips

STM images of the surface, following this preparation procedure, show the presence of two different areas on the surface, as evident from figure 6.12. Part of the sample is covered with rows running along the $[\bar{1}10]$ direction, areas indicated with $\alpha$ in the image, while the rest of the sample shows flat terraces, areas indicated with $\beta$ in the image.
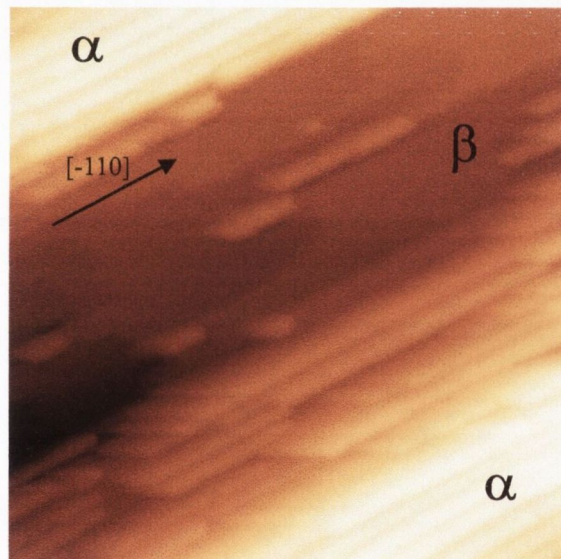


**Figure 6.12**. a) STM image 130x130 nm$^2$ obtained with a tunneling current $I_t$=0.10 nA and $V_b$=-0.83 V, of the single crystal sample after high temperature annealing in UHV. The image shows the presence of two different areas on the surface: areas labeled $\alpha$ display rows running along the $[\bar{1}10]$ direction and areas labeled $\beta$ show the presence of flat terraces.

The areas indicated with $\alpha$ show the presence of rows running along the $[\bar{1}10]$ direction. The corrugation of the surface is very high and multiple steps are often imaged between consecutive rows. This is presented in figure 6.13a, which shows several rows that do not belong to the same terrace; steps of 3 Å, 4.5 Å and 9 Å are measured in the line profile in figure 6.13b, which indicate that both terminations occur on this surface. However, steps equal to or multiple of 3 Å

were most often observed in the areas indicated by $\alpha$. The periodicity of the rows is indicated by the red dashed lines in the figure 6.13b, and is measured to be 35 Å, while the full width at half maximum (FWHM), indicated by the green lines, is found to be 23 Å. The tops of the rows are split into two lines separated by 17 Å, as indicated in the figure by the black lines.



(a)                                     (b)
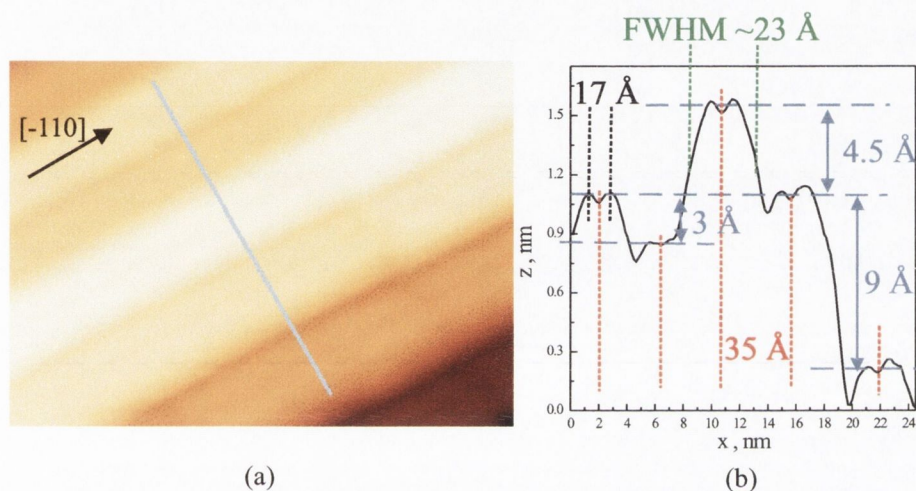
**Figure 6.13**. a) STM image 30x22 nm$^2$ obtained with a $I_t$=0.10 nA and $V_b$=-2.1 V, of the single crystal sample after high-temperature annealing in UHV. b) Line profile showing steps that are a multiple of 1.5 Å. The presence of steps of 1.5 Å, suggests the occurrence of both terminations on the surface. The periodicity of the rows is equal to ~35 Å, the rows split into two lines separated by ~17 Å.

The areas referred to in figure 6.12 as $\beta$ are found to be very flat. This is clear from the figure 6.14a, which presents a STM image showing three different terraces, each of which has corrugation ~0.5 Å. Steps of ~1.5 Å or integer multiples of it, were often imaged, as indicated in figure 6.14b. A zoom in on one of the terraces, is shown in figure 6.15a, with its differential image in figure 6.15b, which shows the presence of some nanostructure resolved on the surface. These nanostructures are elongated along the [001] direction and are separated by 24 Å, as indicated in the line profile in (c). Therefore, they could generate the fractional spots observed in the LEED pattern along the [$\bar{1}$10] direction. Also visible in the image are some atomic lines, perpendicular to these nanostructures

(a)                                                                          (b)
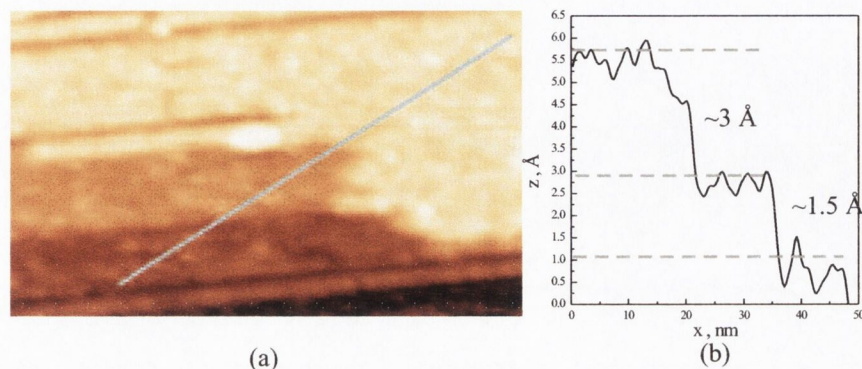
**Figure 6.14**. a) STM image 47x28 nm$^2$ obtained with a W tip, at $I_t$=0.05 nA and $V_b$=-1.3 V. The image shows that areas previously indicated with $\beta$ are generally flat. b) The line profile shows the occurrence of steps of $\sim$1.5 Å and integer multiples of it.

and parallel to the [$\bar{1}$10] direction, shown in the magnified image in (d). These rows are separated by 5.2 Å, as indicated in the line profile in (e).

STS measurements were carried out with W tips on this surface. Figure 6.16 shows in (a) the I/V, in (b) the dI/dV and in (c) the $(dI/dV)/\langle I/V \rangle$ curves of both type of areas, with and without the rows on the surface, as indicated in each graph. From these figures it can be seen that the occupied band of the graphs of the two areas are very similar. A band gap is found for both areas, corresponding to $\sim$0.36 $\pm$0.5 eV and $\sim$0.25 $\pm$0.5 eV for the areas with and without the rows respectively. The band gap expected for $Fe_3O_4$ is $\sim$0.2 V [147]. The unoccupied side of the graphs, exhibits a shoulder for both curves at $\sim$+0.5 V and a shift in the maximum from +2.0 V, or higher, for the area with the rows and +1.25 V for the areas with no rows.

### MnNi tips

STM measurements were also carried out using MnNi tips. The results obtained were found to be broadly similar with those collected with W tips. The two different areas previously indicated with $\alpha$ and $\beta$, were imaged on the surface. In the areas indicated with $\alpha$, rows running along the [$\bar{1}$10] direction were imaged
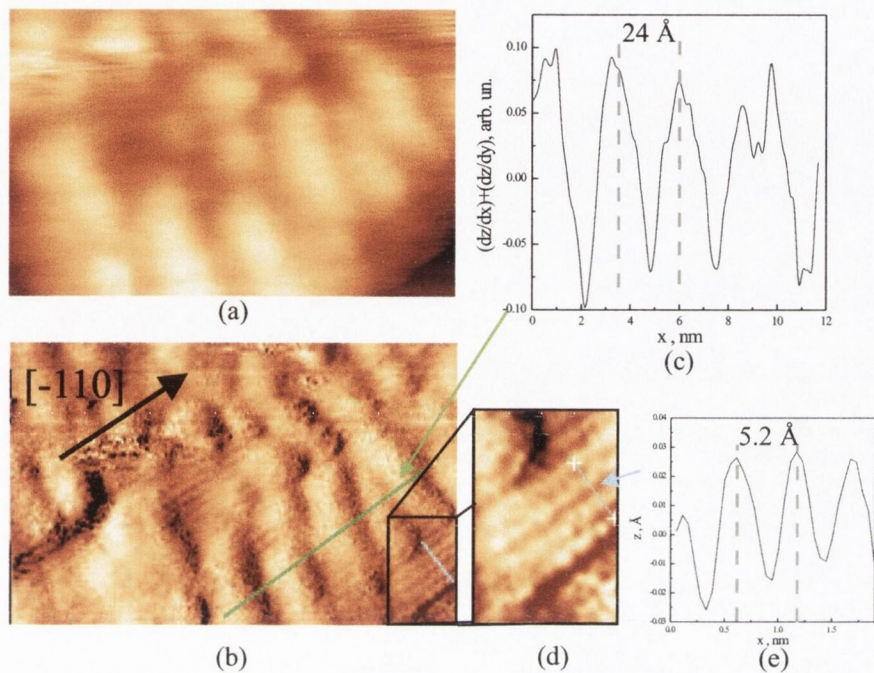
**Figure 6.15**. a) STM image 15x10 nm$^2$ obtained with $I_t$= 0.05 nA and $V_b$=-1.5 V of the $\beta$ areas. b) Differentiated image showing the nanostructures elongated along the [$\bar{1}$10] direction. c) Line profile showing the 24 Å periodicity of the nanostructure elongated along the [$\bar{1}$10] direction. d) Zoom in on the areas with atomic lines. e) Line profile that shows that the atomic lines are separated by 5.2 AA.
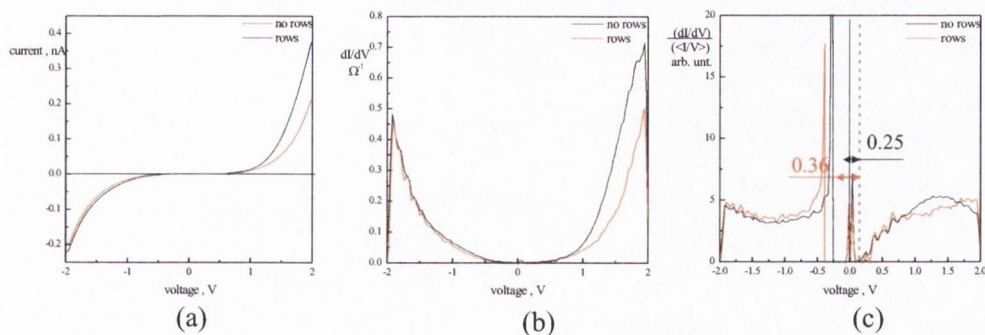


**Figure 6.16**. a) I/V curve of both the areas with and without the rows. It can be seen that the I/V characteristic are very similar in the filled states side and show some differences in the empty states side. b) dI/dV curves that show how both curve maintain the semiconducting character. c) (dI/dV)/⟨I/V⟩ curves that show the different gap of 0.35 ±0.05 eV for the areas with the rows and 0.25 ±0.05 eV for the areas with no rows.

<p align="center">(a)             (b)</p>
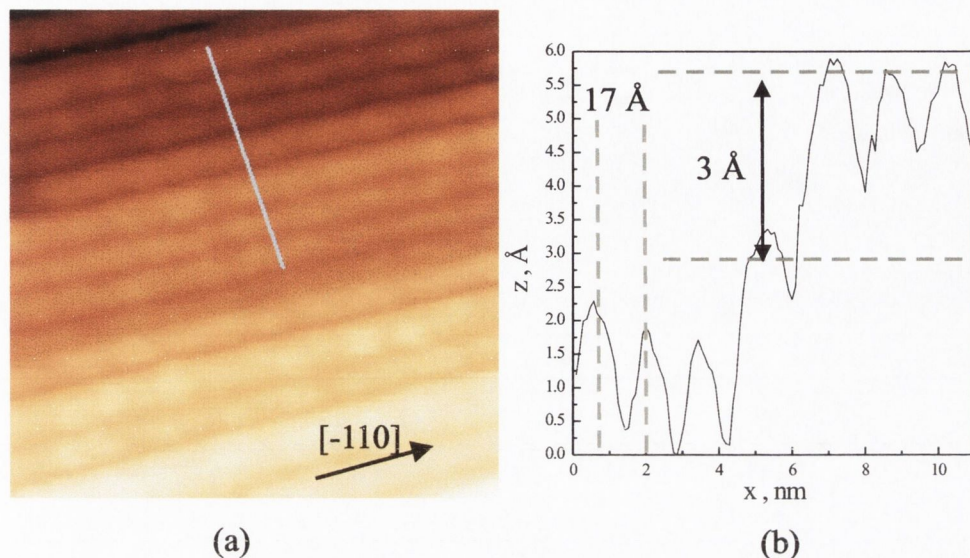
**Figure 6.17**. a) STM image 20x20 nm$^2$ obtained with a $I_t$=0.1 nA and a $V_b$=-1.0 V with a MnNi tip. The image shows the occurrence of rows running along the $[\bar{1}10]$ direction. b) Line profile that shows a step equal to 3 Å between consecutive terraces, as well as a separation of 17 Å between the rows.

and no atomic resolution was achieved, see figure 6.17. A step of 3 Å height is indicated in the line profile in figure 6.17b, as well as the separation between the rows, corresponding to ~17 Å, as in the case of W tips.

### 6.5.3 Discussion of the Surface Reconstruction

Annealing of the surface at high-temperature in UHV induces the desorption of oxygen, with a consequent reduction, of the surface. This is confirmed by AES analysis, which measures an O/Fe=1.44. The LEED pattern shows the appearence of satellite spots corresponding to a p(4x2) superlattice on the surface.

The rows found in the area $\alpha$, somehow resemble those found in the case of annealing of the surface in UHV at 850 K, (described in section 6.3), even if they have different FWHM. This suggests that the atomic structure of the rows is somehow similar in the two cases. As in that case, both terminations are found, even though after annealing at high temperature, the surface is very irregular.
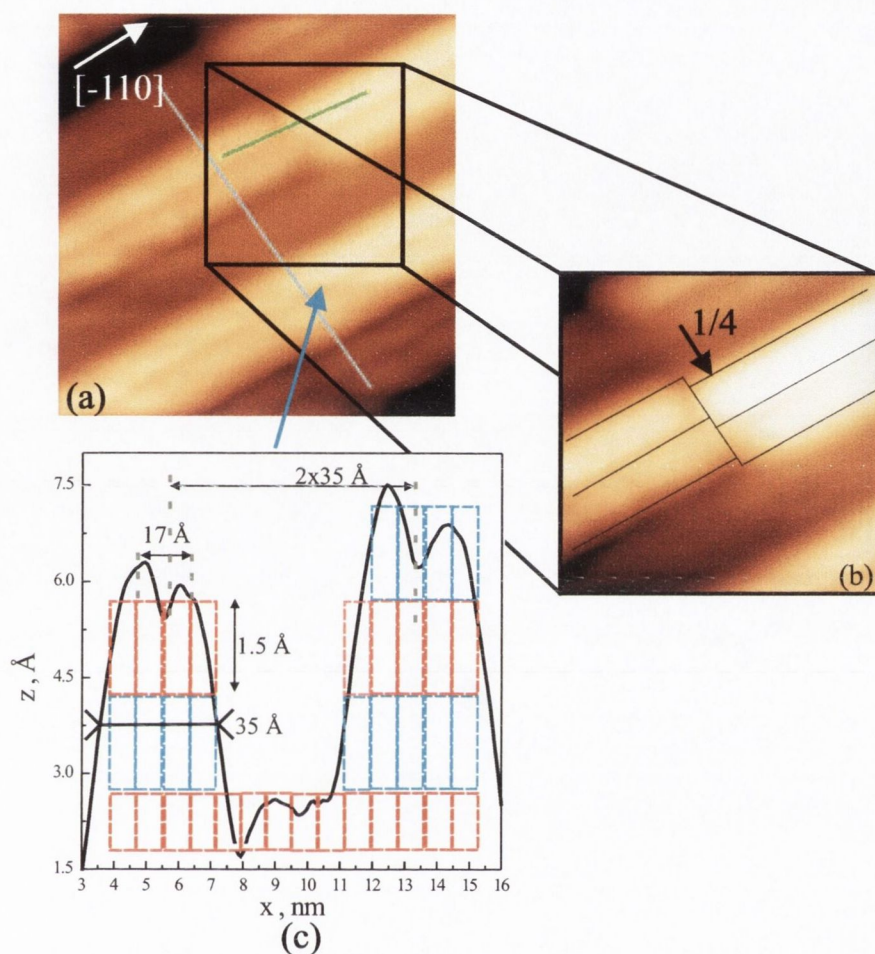
**Figure 6.18**. a) STM image of the area $\alpha$ showing the presence of the rows separated by 17 Å. b) Zoom in on the image in (a) to show that rows separated by a step of 1.5 Å in height, are shifted by 1/4 along the [001] direction. c) Line profile of the rows imaged with a schematic of the model superimposed. The rows' periodicity corresponds to 35 Å, the FWHM is 23 Å. The splitting of the rows into two rows separated by 17 Å is also indicated.

The high corrugation, evident from figure 6.18, suggests that the rows consist of two or three layers. The occurrence of both terminations is clear from figure 6.18b, where rows separated in height by a single step of 1.5 Å are shifted by 1/4 along the direction perpendicular to the rows, i.e. the [001] direction. The line profile in figure 6.18c, has a model superimposed, that considers the rows as constructed form two or three layers. The rectangles represent the unit cells and the different colors refer to different terminations without any particular

preference.

From these considerations, it is reasonable to assume that a breakdown of the reconstruction is induced by the annealing at high temperature in UHV. The occurrence of a high desorption of oxygen, causes the generation of deep valleys between the rows, until some limit is reached and the rows are no longer stable on the surface. When this limit is reached, the surface reconstruction changes and the flat areas, previously indicated with $\beta$, are found on the surface. These areas present some irregular structures, elongated along the [001] direction, but not well resolved. It seems that they grow on top of rows separated by 5.2 Å, as already indicated in figure 6.15. A periodicity of 5.2 Å is not in agreement with any of the separation present in the two planes of the $Fe_3O_4(110)$ surface. The possibility of different iron oxide phases present on the surface, cannot therefore be ruled out, although all the other iron oxide phase have a higher O/Fe ratio than magnetite.

In order to determine what phase could be present in the areas labeled $\beta$, let us consider the various possibilities. There are three known iron oxide other than magnetite: haematite ($\alpha$-$Fe_2O_3$), maghemite ($\gamma$-$Fe_2O_3$) and wüstite (FeO), see the table 2.1 in section 2.2. The only one with a lower O/Fe ratio is FeO, therefore it is reasonable to assume that this is the phase found on the surface.

In conclusion, annealing of the $Fe_3O_4(110)$ surface at high temperature in UHV induces the breakdown of the rows reconstruction of $Fe_3O_4(110)$. There is a possibility of a phase change on the surface, from $Fe_3O_4$ to FeO, but it is not possible to conclusively determine what phase at this stage.

# Chapter 7

# Study of the (110) Surface of Fe$_3$O$_4$ Thin Films

## 7.1   Introduction

In this chapter the STM experiments carried out on the Fe$_3$O$_4$(110) thin film samples are described. Two samples were obtained from a Fe$_3$O$_4$(110) thin film of thickness equal to 50 nm. Two distinct preparation procedures were carried out on the samples, similar to the those described in the previous chapter for the Fe$_3$O$_4$(110) single crystal. Sample S1 was annealed at high temperature, $\sim$1100 K, in oxygen atmosphere while sample S2 was annealed at high temperature, $\sim$1100 K, in UHV. First a characterisation of the thin film in terms of XRD and resistivity measurements is given. Then, AES and LEED analysis together with STM experiments are described in detail for the different cases. The experimental results are, then, compared with the ones obtained for the single crystal and with the model proposed in the previous chapter.

## 7.2 Samples Characterisation

The magnetite film used for this study was grown on an MgO(110) substrate, 0.5 mm thick, purchased from MTI Corporation [148] and had a thickness equal to 50 nm. It was grown in this laboratory in an oxygen plasma assisted molecular beam epitaxy system (MBE)(DCA MBE M600, Finland), at 530 K and oxygen pressure $1.5 \times 10^{-5}$ mbar.
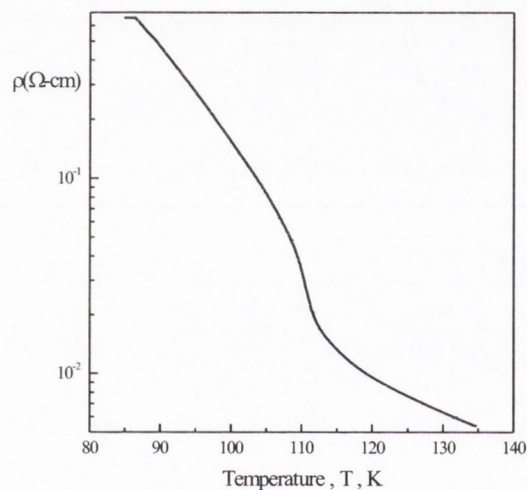


**Figure 7.1**. Resistivity versus temperature curve for the 50 nm $Fe_3O_4$/MgO(110) thin film sample. A Verwey temperature of $\sim 110$ K is measured.

The resistivity versus temperature curve measure a Verwey temperature of $\sim 110$ K, see figure 7.1. It must be noted here that the resistivity of thin film samples is generally higher than that of the bulk crystal even at room temperature, due to the presence of antiphase boundaries (APBs), which increase with decreasing thickness of the films [73]. This results in a higher number of domain boundaries which enhance the scattering of conducting electrons and, therefore, the resistivity [33]. For the samples presented here, the resistivity at room temperature was measured to be 0.16 $\Omega$cm. It is important to know the resistivity of

thin films samples as, at room temperature, it affects both the AES and LEED pattern by decreasing the signal to noise (S/N) ratio as the resistance increases. For this reason, the spectra shown in this chapter contain a relatively high noise.

From the $Fe_3O_4(110)$ thin film, two samples were obtained, which will be indicated as sample S1 and S2 respectively. They were both introduced into the UHV chamber as grown. Inside the UHV system, they were prepared taking into consideration the fact that prolonged annealing of the films at temperatures above 600 K induces the diffusion of Mg from the substrate to the surface, with possible formation of magnesium ferrite, $MgFe_2O_4$ [149, 150, 22].

## 7.3 Sample S1: Annealing in Oxygen at 1100 K

### 7.3.1 AES and LEED Analysis

After the introduction of the sample into the UHV system AES and LEED measurements were taken to check the composition of the surface. The AES spectrum is presented in figure 7.2a. It shows a considerable amount of contaminants such as C and N, and others in lower quantity such as Ca, S and K. The LEED patterns and the STM images at this stage show a disordered surface, as expected for a sample just loaded into the system.

Afterward, the sample was annealed in the e-beam heater in $2.27x10^{-6}$ mbar of $O_2$ pressure for 5 minutes at a temperature of $1100 \pm 50$ K. Four of these cycles were performed in total. AES, LEED and STM measurements were taken between cycles to monitor the changes in the surface composition and reconstruction.

An AES spectrum taken after 2 annealing cycles is shown in figure 7.2b. The spectrum exhibits the oxygen peak at 509 eV, the iron peaks centred on 650 eV, the low energy iron peaks at 43 eV and 52 eV, and the O/Fe = 1.7. It can be seen that the concentration of contaminants, such as Ca and Mg, is negligible.

Figure 7.3 presents a LEED pattern of the film taken at a primary energy
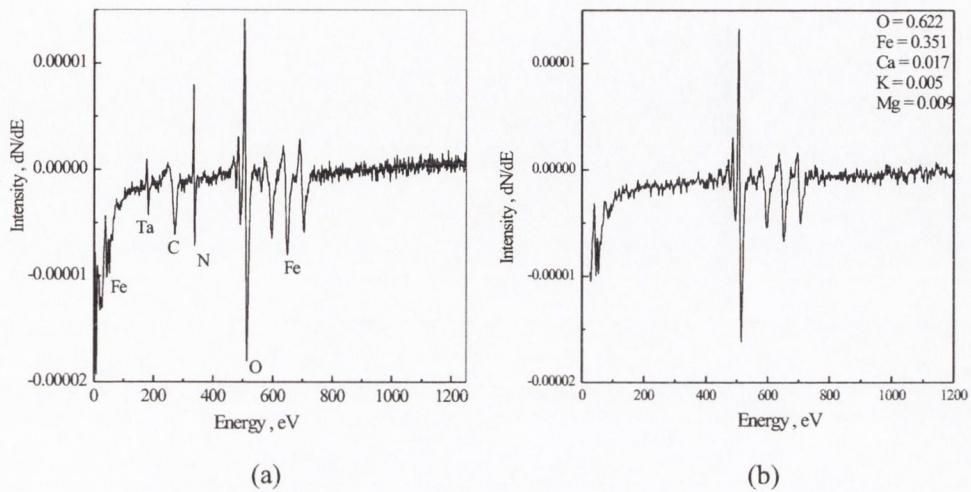
**Figure 7.2**. a) AES spectrum of the sample S1 as loaded in the UHV system showing relatively high concentration of contaminants. b) AES spectrum taken after the first 2 annealing cycles. It can be seen that the majority of contaminants are removed.
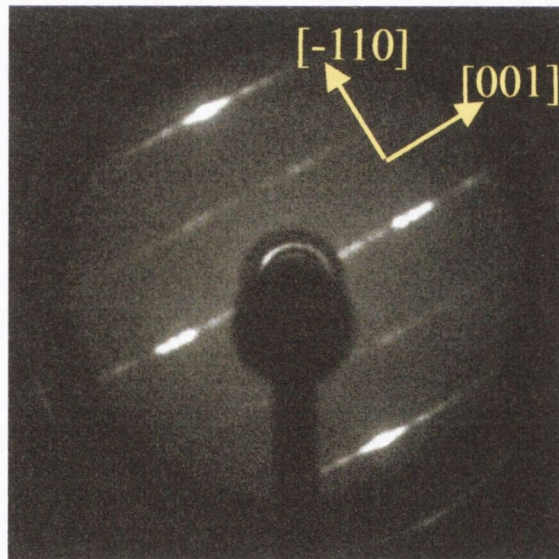


**Figure 7.3**. LEED pattern of the sample S1 taken at a primary energy beam of 47 eV. It shows lines of spots along the [001] direction. The spectrum is blurred due to the high resistance of the sample and it is difficult to indicate accurately the unit cell.

beam of 47 eV . It can be seen that there are five rows of spots running along the [001] direction. The brighter spots are generated by the scattering of the

oxygen ions sublattice, which have half the space of iron cations. Therefore the
$(0,\pm2)$ and $(\pm2,0)$ spots are brighter as expected [131]. The distance between
the rows along the $[\bar{1}10]$ direction corresponds to a separation of $\sim6$ Å in real
space. The irregularity of the spots in the spectra, and the fact that they are
blurred because of the low sample conductivity, impeded the measurement of the
periodicity along the rows with sufficient accuracy.

### 7.3.2 STM Measurements

STM measurements were carried out on this surface with W tips. The occur-
rence of terraces is presented in figure 7.4a, even if the terraces imaged were not
very flat and regular. The separation in height between successive terraces was
found to vary quite substantially and multiple steps were frequently observed.
Although steps of 1.5 Å were occasionally observed, on average, minimum steps
equal to 3 Å were most often measured, as indicated in the figure 7.4 b. This is
in agreement with the fact that one of the two termination is more stable in these
conditions, as the separation between different planes in the bulk is equal to 1.5
Å. On top of the terrace, rows aligned along the $[\bar{1}10]$ directions are imaged. The
line profile of the STM image, presented in the figure 7.4b, shows that the rows
are separated by 25 Å. The row separation of 25 Å is very regular, although it
is clear that some of the rows are missing and other are incomplete. A zoom
in on the rows, is presented in figure 7.5a. This image shows very well how the
rows split into two. The line profile presented in figure 7.5b indicates that the
two smaller rows are separated by 8.4 Å and that the full width at half maximum
of the large rows is $\sim17$ Å. Also indicated in the figure is the periodicity of the
large rows, corresponding to 25 Å. The width of the gap between the large rows,
corresponds to $\sim8$ Å along the [001] direction. This suggests that the gap is
found because one of the small rows is missing. This is evident from figure 7.5a,
where black lines are a guide to the eye to emphasise the occurrence of two line

(a)                                              (b)
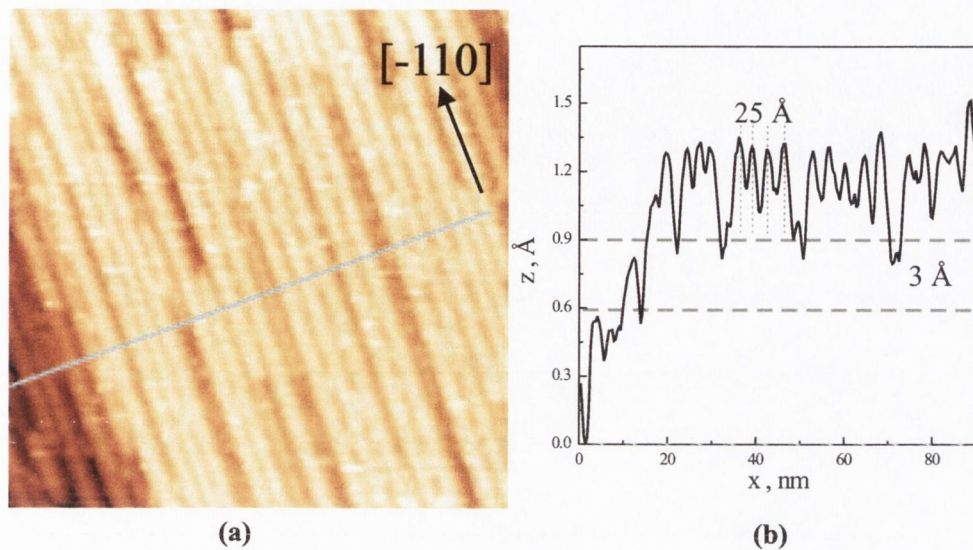
**Figure 7.4**. a) STM picture, 80x80 nm$^2$, of the sample S1 taken at a $I_t = 0.1$ nA and a $V_b = -2.0$ V. The image shows the presence of rows on the terrace, running along the $[\bar{1}10]$ direction. b) The line profile indicates the occurrence of steps equal to 3 Å, as well as the periodicity of the rows, corresponding to 25 Å.



(a)                                              (b)
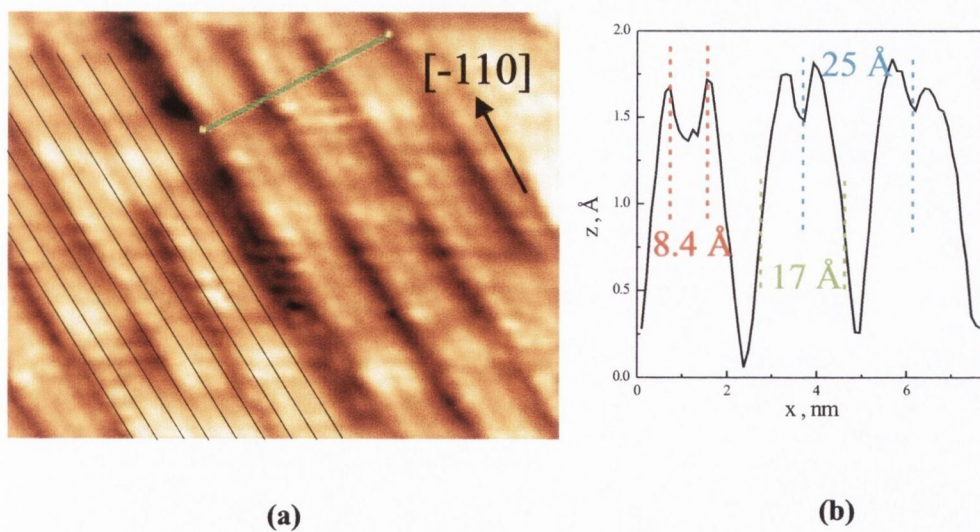
**Figure 7.5**. STM picture 17.3x13.5 nm$^2$ of the sample S1 sample taken with $I_t$=0.1 nA and $V_b$=-2.0 V. The 25 Å rows oriented along the $[\bar{1}10]$ direction are clearly visible, as well as the occurrence of a missing line between each row. b) Line profile that shows the 25 Å periodicity of the rows, the FWHM of 17 Å and the splitting of the rows into to lines separated by 8.4 Å.

8.4 Å wide every three.

### 7.3.3 A model for the surface reconstruction

AES analysis measures an $O/Fe = 1.7\pm0.15$, which is just at the limit of the expected ratio for a magnetite phase on the surface, [143]. The LEED pattern does not give clear clues about the possible termination of the surface, but is in agreement with the presence of rows on the surface, being responsible for the fractional spots aligned along the [001] direction in figure 7.2c.

STM measurements have shown that both terminations can be found on the surface, as steps equal to 1.5 Å have been measured. However, the majority of steps were found to be equal to or multiple of 3 Å, suggesting that one of the terminations is more stable than the other. Figure 7.5 indicates a FWHM for the rows of 17 Å, corresponding to 2 unit cells. A schematic of a possible model for the surface reconstruction is presented in figure 7.6. In this model, an A-termination is considered for reasons that are explained later. The separation of 8.4 Å between the two lines on top of each row corresponds to the separation between atomic rows consisting of the $Fe_{oct}$ and the dark line in the centre, to the $Fe_{tet}$. This is in agreement with the fact that the conduction electrons in $Fe_3O_4$ are carried by the $Fe_{oct}$, while the $Fe_{tet}$ do not have electronic states at the Fermi energy [63, 9, 10].

Furthermore, let us consider the unit cell of the reconstructed surface as indicated in figure 7.6a by the green rectangle. It is composed of 2 unit cells of the A-plane plus one that is missing. Considering the electrostatic model (EM) for polar surfaces, three unit cells of the A-plane would leave a charge equal to +9. The unit cell of the surface reconstruction consists of 8 oxygen atoms with oxidation state -2, 4 $Fe_{oct}$ with oxidation state +2.5 and 4 $Fe_{tet}$ with oxidation state +3. This results in (-16 + 10 + 12)= +6. Therefore there is a reduction in the charge from +9 to +6. This suggests that the model proposed is more stable
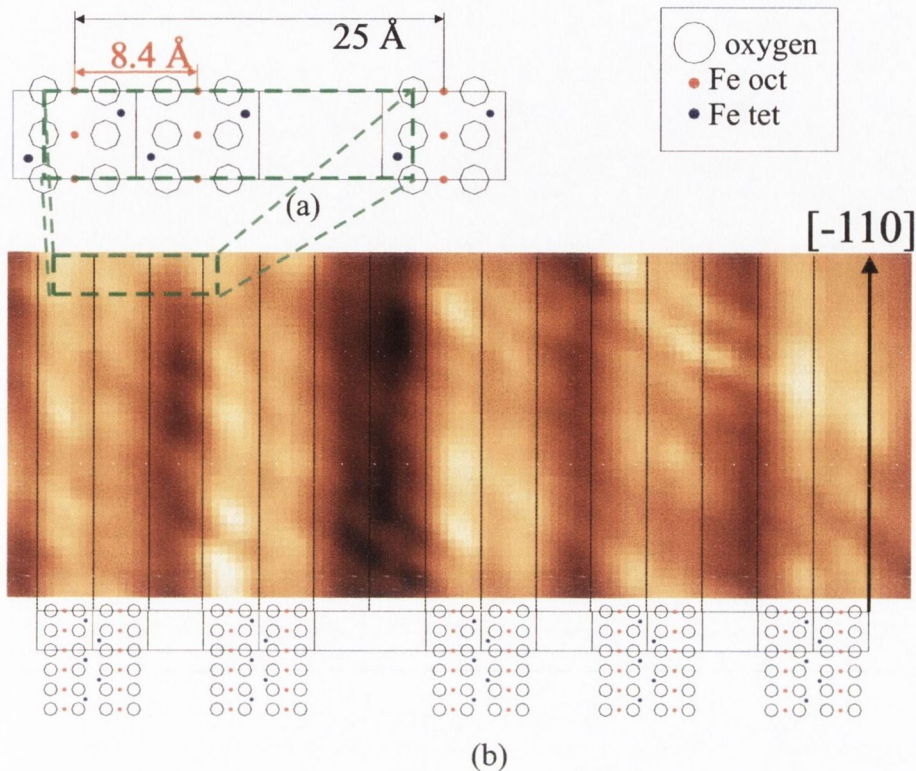
**Figure 7.6**. a) Model proposed for the reconstruction of the sample S1 surface. The unit cell is indicated by the green rectangle. b) The model proposed is compared with an STM image of the surface.

than the bulk-termination.

If the electron counting model (ECM) is considered instead, the three unit cell of the bulk termination would have an excess of $1.5x3= 4.5$ $e^-$. In the unit cell of the reconstructed surface, there are 8 oxygen atoms, all involved in bonds with $Fe_{oct}$. According to what was already introduced in section 5.2.2, this gives a total of $(8x19/12 + 8x5/12 + 4x3/4)= 19$ $e^-$, that can occupy the 8 oxygen's dangling bonds with a residual charge of only 3 $e^-$ per unit cell. This charge in excess is smaller than the expected one of $4.5e^-$, therefore, the ECM model also confirms that the model proposed for the reconstruction is more stable than the possible bulk terminations.

Comparing this reconstruction with the reconstruction obtained in the case of the $Fe_3O_4(110)$ single crystal surface, annealed at high temperature in oxy-

gen described in section 6.4, some similarities can be found. First of all, both terminations are found in both cases and one of them is more favourable than the other. However, the preferred termination in the two cases is different, being the B-termination in the case of the single crystal, and the A-termination in the case of the thin film. The B-termination should be slightly favoured in oxygen annealing, because the O:Fe ratio is higher than in the A termination. However, the occurrence of one termination or the other one could be determined by several factors such as the level of contaminants, which are higher in the thin film, or the stress of the thin films, which could stabilise the A-termination more than the B-termination. Nevertheless, it can be seen that the terraces labeled as A in the section 6.4, are very similar to the terraces imaged in this section, and that the model proposed in this section, is therefore consistent with the one proposed in the previous one.

## 7.4 Sample S2: Annealing in UHV at 1100 K

Sample S2 was introduced into the UHV system and directly annealed in the e-beam heater in UHV environment for 7 min at 1100 ±50 K. Four cycles of this treatment were necessary to remove C and N contaminants.

### 7.4.1 AES and LEED Analysis

The AES spectra, presented in figure 7.7a, shows that annealing in UHV produces the diffusion of contaminants to the surface, evident from the presence of a strong calcium peak at 291 eV and a less evident magnesium peak at 1186 eV. The concentrations calculated for these contaminants are Ca 10±3% and Mg 14±3%, as seen in figure 7.7. The oxygen peak at 509 eV, the iron peaks centred on 650 eV and the low energy iron peaks at 43 eV and 52 eV, are also present in the spectrum and O/Fe = 1.8±0.3% is calculated. It is worth noting here

(a)                                            (b)
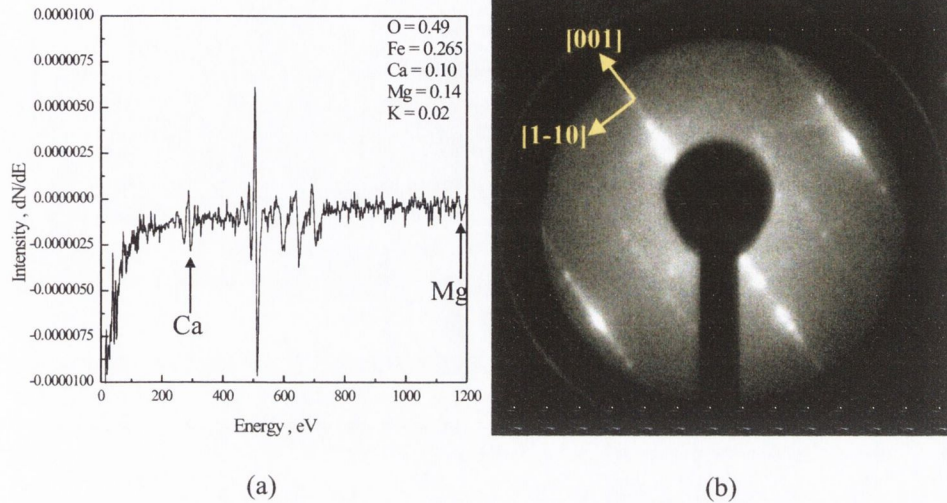
**Figure 7.7**.  a) AES spectrum of the sample S2 showing a high concentration of contaminants as indicated by the elements' concentration reported in the graph. b) LEED pattern taken at a primary beam energy of 44 eV of the sample S2 showing five lines of spots along the [001] direction.

that the large error associated with the contaminants' concentrations and the O/Fe, is due to the high noise of the spectra, which, as previously explained, is due to the high resistivity of $Fe_3O_4$ thin films. Moreover, the high concentration of contaminants, particularly Mg in $\sim 14\%$, could be responsible for a further increase of the resistance of the sample, due to formation of magnesium ferrite ($MgFe_2O_4$) on the surface, which is an insulator [149, 150, 22].

Figure 7.7b, shows that the LEED mesh is very blurred. The pattern, obtained at an energy of 44 eV shows again five lines of spots aligned along the [001] direction, as in the case of sample S1. The separation of these lines corresponds to a periodicity of $\sim 6$ Å along the [$\bar{1}$10] direction in real space. The separation of the spots along the perpendicular direction is not found to be regular, thus not allowing one to determine the unit cell.

### 7.4.2   STM Measurements

STM measurements were carried out on this surface with W tips. Large area scans show the presence of two types of area on the surface, as shown in the figure 7.8. These are similar to what was observed in the case of high temperature annealing of the $Fe_3O_4(110)$ single crystal in UHV, (section 6.5). The two types of area are indicated with $\alpha$ and $\beta$, in analogy with the section 6.5.
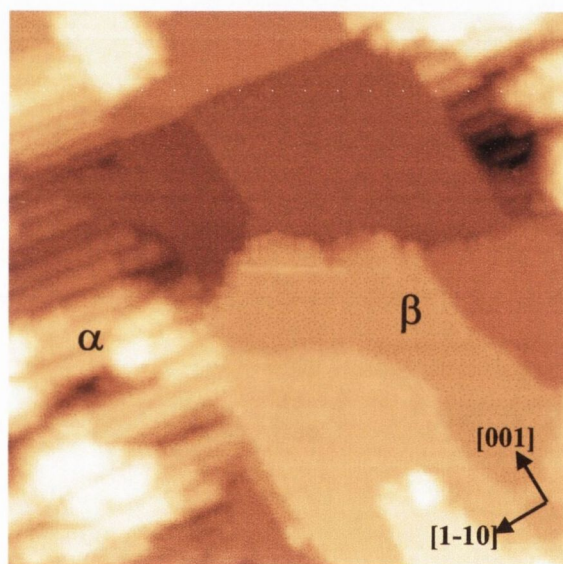


**Figure 7.8**. STM image, 90x90 nm$^2$, of the sample S2 taken at $I_t$=0.05nA and $V_b$=-2.0V. The image shows the existence of two different surface terminations, labeled as $\alpha$ and $\beta$. Areas $\alpha$ show the presence of rows running along the [$\bar{1}$10] direction, while areas $\beta$ consist of flat terraces.

Areas labeled as $\alpha$ present a very high corrugation, which is indicative of a surface not well formed. Such a high corrugation makes impossible the detection of terraces or steps. Rows oriented along the [$\bar{1}$10] direction are found on these areas, separated by a $\sim$35 Å periodicity, see figure 7.9. The FWHM of these rows varies around $\sim$17 Å$\pm$ 5Å.

Terraces labeled as $\beta$ are very flat, see figure 7.10, and display steps equal to or a multiple of 3 Å. The terrace edges are parallel to the [001] and [$\bar{1}$10] directions. No atomic scale reconstruction was imaged on these terraces.

(a)                                          (b)
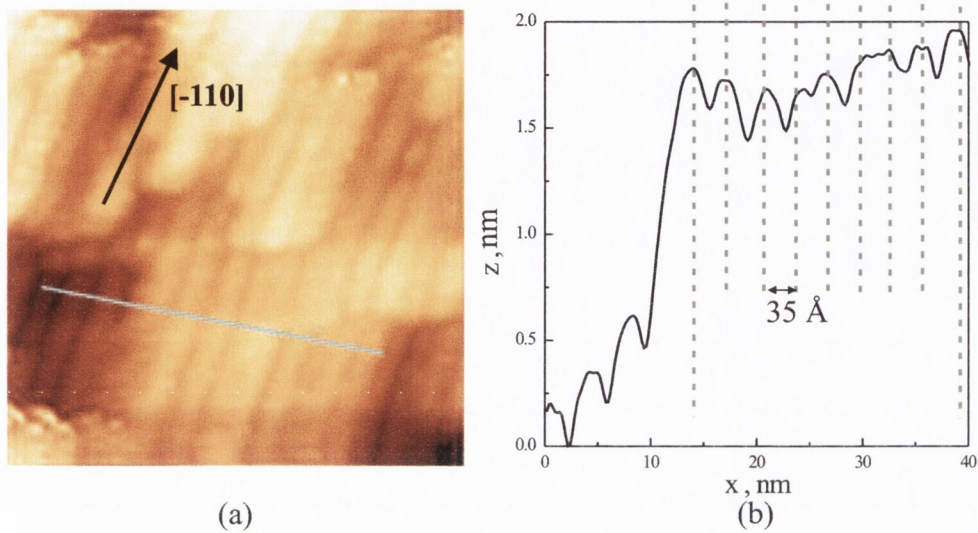
**Figure 7.9**. a)STM image, 45x45 nm$^2$, of sample S2 obtained with $I_t = 0.05$ nA and $V_b = -1.8$ V. The image shows the presence of rows oriented along the [$\bar{1}$10] direction on the surface. b)The line profile shows that the rows are separated by $\sim$35 Å.



(a)                                          (b)
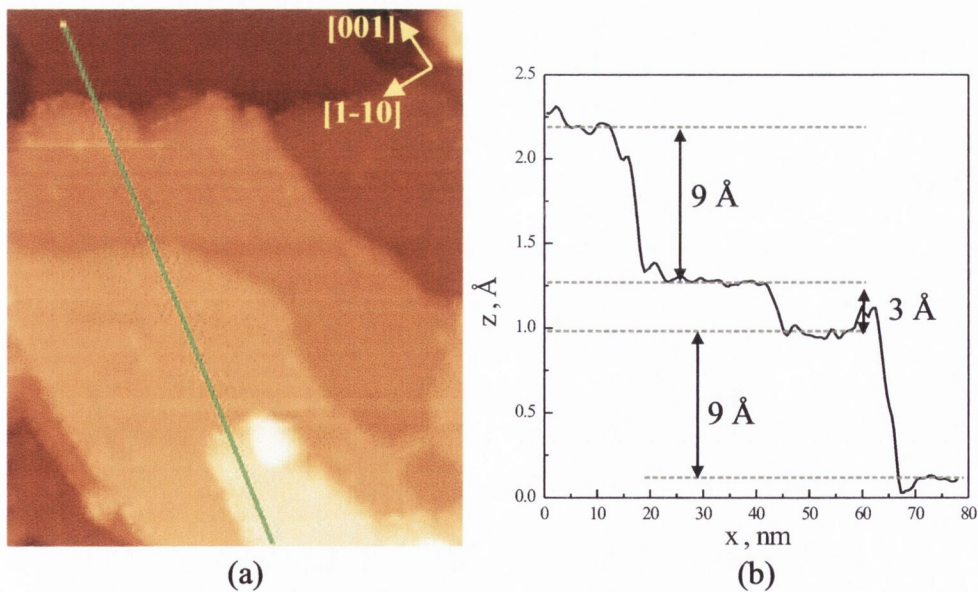
**Figure 7.10**. a) STM image, 55x65 nm$^2$, of the sample S2 taken with $I_t$=0.05 nA and $V_b$=-2.0 V, showing the presence of flat terraces. The terrace edges are parallel to the [001] and [$\bar{1}$10] directions. b) Line profile that shows the occurrence of steps equal to, or a multiple of 3 Å.

### 7.4.3 Discussion of the Surface Reconstruction

It is expected that annealing the $Fe_3O_4(110)$ surface in UHV would induce the desorption of oxygen from the surface, as already explained in section 6.5. In the case of the sample S2, this was not confirmed by the AES analysis, which showed a O/Fe∼1.8, in disagreement with what was found in the case of the single crystal sample. However, the high concentration of Mg on the surface (∼14%), causes, probably, the formation of $MgFe_2O_4$. The substitution of Fe atoms with Mg atoms could be then responsible for the high O/Fe (∼1.8). Furthermore, $MgFe_2O_4$ is an insulator, therefore the resistance of the sample would increase as the concentration of Mg, and therefore $MgFe_2O_4$, increases, resulting in a poor quality of the AES spectra, which carry a relatively high noise. The same considerations can be applied to the LEED patterns, that do not furnish highly accurate information, as they are blurred in general, making the observation of a reconstruction on the surface very difficult.

The STM images of the surface show 2 type of areas very similar to what was observed for the single crystal in section 6.5. The areas labeled as $\alpha$ exhibit the same periodicity of the rows and similar FWHM. The high corrugation found in these areas can be attributed to the annealing of the surface at high temperature in UHV, which seems to favour the desorption of oxygen from the surface with consequent breakdown of the surface reconstruction. The rows are often separated in height by integer multiples of the minimum step height of 1.5 Å, which suggests that both A- and B-terminations can be found in these areas.

Also the areas labeled as $\beta$ are similar to the ones obtained for the single crystal. However, it was not possible to image any ordered structures in the thin film, and the resolution achieved in the case of the single crystal, was much higher.

From these considerations it can be assumed that the desorption of oxygen from the surface, caused by the high temperature UHV annealing, generates a

breakdown of the surface reconstruction. This results in the high corrugation found in the areas labeled as $\alpha$ and in the formation of the areas labeled as $\beta$, in analogy to what was found for the single crystal. The $MgFe_2O_4$ present on the surface is probably gathered in the areas $\beta$ as they were more difficult to image.

# Chapter 8

# Conclusions

The work described in this thesis can be divided into two main parts. The first part consists of the description of a new instrument, the LTTD, designed and built to measure the deformation of $Fe_3O_4/MgO$ thin films when cooled down through the Verwey transition. In the second part, AES, LEED and STM-STS have been used to characterise the surface reconstruction of $Fe_3O_4(110)$ in the case of single crystal and of two thin films deposited on MgO substrate.

## 8.1 The LTTD for the Measurement of the Deformation of $Fe_3O_4/MgO$ Thin Films at the Verwey Transition

The LTTD was designed and built in this lab in order to measure very small deformations, within a few hundreds nanometers range, of a sample along one of its axes. The calibration and testing of the system confirmed a sensitivity of the LTTD equal to 0.25 Å.

The deformations of $Fe_3O_4/MgO$ (001) and (111) thin film samples were measured using the LTTD. The expected sharp change in the curvature radius of the bilayer samples, in correspondence of $T_V$, was not detected, even though the

transition was measured in the resistivity vs temperature curves. The absence
of the signal expected at $T_V$, was attributed to the presence of a high density
of APBs in the thin films. APBs are believed to be responsible for the fact that
epitaxial $Fe_3O_4/MgO$ films are able to accommodate the mismatch strain even
for thicknesses up to ~700nm. The $Fe_3O_4/MgO$ films are strained in-plane by
the substrate and strain relaxation does not occur even for a thickness of about
700 nm. In this situation, the deformation at $T_V$ is favoured in the out-of-plane
direction. If this is the case, there is no mismatch strain developed at the inter-
face due to the Verwey transition and no change in the radius of curvature of the
sample occurs. Therefore, the transition cannot be detected with this method.
This results suggests that the mechanism of the Verwey transition in thin films
and single crystal is different, due to the presence of a high density of APBs,
which prevent strain relaxation of the $Fe_3O_4/MgO$ thin films.

## 8.2   $Fe_3O_4$ (110) single crystal

The $Fe_3O_4$ (110) face of the single crystal sample prepared by $Ar^+$ etching and
UHV annealing cycles at 850 K, showed the formation of rows parallel to the $[\bar{1}10]$
direction. STM measurements showed a periodicity of the rows equal to 25Å, as
well as some features resolved on the top of the rows. The model proposed for
this reconstruction, considers that the rows are formed by two layers, one of type
A at the bottom, and one of type B on top. This is in agreement with the FWHM
of the rows and with the periodicity of the nanostructures, equal to 8.4x10 $Å^2$,
which is consistent with a B-termination.

High temperature annealing in an oxygen atmosphere produces a well-formed
surface structure, which shows the presence of flat terraces characterised by low
corrugation. On the terraces, rows parallel to the $[\bar{1}10]$ direction are found,
showing a different periodicity on different terraces, of 4.5 Å and 8.2 Å. The step

between consecutive terraces and the periodicity of the rows are consistent with both terminations being present on the surface. However, multiple steps of 3 Å in height are more often found on the surface, indicating that the B-termination is dominant. This is due to the fact that annealing in oxygen favours the B-termination, which is richer in oxygen than the A one. Furthermore, the high-temperature annealing in oxygen atmosphere causes the adsorption of oxygens on the surface, which could impede the achievement of atomic resolution.

Annealing of the Fe$_3$O$_4$ (110) single crystal in UHV at high temperature induced the breakdown of the surface reconstruction. The rows present on the surface, parallel to the [$\bar{1}$10] direction, are in some areas replaced by some flat terraces, which show no particular reconstruction. This is due to the fact that annealing in UHV causes a high desorption of oxygen from the surface. The longer the annealing time, the larger the extension of these flat areas. STM data suggest that in these areas, another form of iron oxide could be present, that is FeO. This iron oxide has a lower O/Fe, and could be favoured by the preparation conditions. However, STS experiments measured a smaller band gap for these areas, which is in disagreement with the STM data. More experiments are needed to clarify these points.

## 8.3   Fe$_3$O$_4$/MgO (110) thin films

The Fe$_3$O$_4$/MgO (110) thin film annealed in oxygen at high temperature, showed the formation of flat terraces formed by rows running along the [$\bar{1}$10] direction. Both termination are, once again, found on the surface. However, contrary to what was found in the case of the single crystal, the dominant surface termination is of type A. This was not expected because annealing in oxygen favours the B-termination. Possible explanations are that the films are not strain relaxed and that Mg contaminant, present in the thin film but not in the single

crystal, could favour one of the two terminations. The model proposed considers a missing-row surface reconstruction of the A-termination, where the rows split into two smaller rows made of $Fe_{oct}$ and a row of $Fe_{tet}$ in the centre.

Annealing of the second $Fe_3O_4/MgO$ (110) thin film in UHV produced a very similar surface to that of the single crystal prepared in the same conditions. The UHV annealing induces a high desorption of oxygen from the surface and the rows on the surface are partly replaced by flat areas showing no ordered structure. Moreover, the high-temperature annealing induces a high diffusion of Mg from the substrate, which most likely results in the formation of $MgFe_2O_4$. This compound, which is an insulator, is believed to gather in the flat areas, which were more difficult to image.

The results related to $Fe_3O_4$ (110) are summarised in table 8.1.

## 8.4 Future Work

### 8.4.1 Experiments with the LTTD

The next step in the development of the LTTD will be in the operation of the system at liquid helium temperature, in order to operate the superconducting magnet. The first attempt to cool down the LTTD has already been made, even though, due to the lack of experience together with some technical difficulties, the results were unsuccessful and more work has to be done in this direction.

As regards to future experiments, the LTTD can be used for the measurements of single crystal and thin film magnetostriction. In the case of single crystals, the configuration used for measuring the Verwey transition in the $Fe_3O_4$ rod would be used. For thin films, the cantilever bending technique can be implemented [151].

Another possibility will be the measurement of the Young modulus of thin film samples using the cantilever bending technique. The elastic properties of

| Sample | Preparation | Results |
|---|---|---|
| Fe$_3$O$_4$(110) SC | anneal @ 850 K in UHV $\sim$ 1x10$^{=9}$ | B-termination. Formation of rows of 35 Å periodicity. |
| Fe$_3$O$_4$(110) SC | anneal @ 1100 K in O$_2$ 2.67x10$^{-6}$ | The B-termination is dominant. Rows separated by 4.5 Å are formed |
| Fe$_3$O$_4$(110) SC | anneal @ 1100 K in UHV $\sim$ 1x10$^{=9}$ | Breakdown of the reconstruction with possible formation of FeO |
| Fe $_3$O $_4$/MgO(110) TF | anneal @ 1100 K in O$_2$ 2.67x10$^{-6}$ | The A-termination is dominant. Formation of rows separated by 25 Å. The rows split into two smaller rows separated bt 8 Å, and the surface is stabilised by a missing-row reconstruction. |
| Fe $_3$O $_4$/MgO(110) TF | anneal @ 1100 K in UHV $\sim$ 1x10$^{=9}$ | Breakdown of the reconstruction with possible formation of magnesium ferrite MgFe$_2$O$_4$ |

**Table 8.1**. Summary of the STM results obtained from the measurement of the surface reconstruction of the Fe$_3$O$_4$ (110) surface.

thin films at low temperature are difficult to determine because of the difficulty in measuring all the components of the stress tensor.

## 8.4.2   Fe$_3$O$_4$(110)

Further characterisation of the Fe$_3$O$_4$ (110) surface is necessary for both the single crystal and the thin films samples. STM measurements have shown that the surface generally reconstructs forming rows oriented along the [$\bar{1}$10] direction, however, no agreement is generally found in literature, about the structure of the rows. More STM-STS measurements, possibly at different temperatures, are

necessary in order to conclusively address the reconstruction of the surface.

Currently, our group is collaborating with the Experimental Solid State Physics II group at the University of Nijmegen. We have provided them with some MnNi tips and there has been a mutual exchange of $Fe_3O_4/MgO(110)$ samples. The work in progress involves continuous discussion and is aimed at the characterisation of the $Fe_3O_4/MgO(110)$ samples using STM, STS at different temperatures. These studies will be devoted to the investigation of the topographic properties of the surface using magnetic tips, such as MnNi or Cr tips, in order to measure the spin-polarised properties of the surface at RT and at LT. The possibility of performing experiments in a magnetic field can be also considered. It would be particularly interesting to perform these measurements at LT, in order to study the topographic and spectroscopic properties of this face of magnetite, below and above the Verwey transition. Within this project, the interaction of MnNi tips with the $Fe_3O_4(110)$ surface, are being modeled using DFT calculations.

Furthermore, the models proposed for the surface reconstructions described in this thesis, need to be tested against DFT calculations. This work has been started and is at a very early stage.

The surface reconstructions of this surface could be used for the development of tailored magnetic surfaces. Particularly the regular structures observed after preparation of the surface in an oxygen atmosphere, could be used as a template for evaporation of different metals such as Fe, Co, Ni, Mn, etc.. To this end, some preliminary tests on the evaporation of Fe on the $Fe_3O_4$ single crystal and $Fe_3O_4/MgO(110)$ thin films, have shown that, at low coverage, Fe islands align along particular crystallographic directions of the crystal. This study is at a very preliminary stage and more experiments need to be carried out before any conclusions can be drawn. This work is aimed not only to the study of the films'growth, but particularly at the characterisation of the fundamental structural and electronic properties of the metal/oxide interface.

# Bibliography

[1] G. A. Prinz. *Science*, 282:1660, 1998.

[2] H. Kanai, K. Noma, and J. Hong. *FUJITSU Sci. Tec. J.*, 37(2):174, 2001.

[3] S. A. Fang, G. A. de Wijs, and R. A. de Groot. *J. Appl. Phys.*, 91(10):8340, 2002.

[4] X. W. Li, A. Gupta, G. Xiao, W. Qian, and V. P. Dravid. *Phys. Rev. Lett.*, 73(22):3282, 1998.

[5] P. Seneor, A. Fert, J-L Maurice, F. Montainge, F. Petroff, and A. Vaurès. *Appl. Phys. Lett.*, 74(26):4017, 1999.

[6] T. Kiyomura, Y. Maruo, and M. Gomi. *J. Appl. Phys.*, 88(8):4768, 2000.

[7] S. A. Wolf, D. D. Awschalom, R. A. Buhrman, J. M. Daughton, S. von Molnár, M. L. Roukes, A. Y. Chtchelkanova, and D. M. Treger. *Science*, 294:1488, 2001.

[8] S. Parkin, X. Jiang, C. Kaiser, A. Panchula, K. Roche, and M. Samant. *Proc. of the IEEE*, 91(5):661, 2003.

[9] A. Yanase and K. Sirartori. *J. Phys. Soc. Jpn*, 53:312, 1984.

[10] Z. Zhang and S. Satpathy. *Phys. Rev. B*, 44:13319, 1991.

[11] J. S. Moodera, J. Nassar, and G. Mathon. *Annu. Rev. Mater. Sci.*, 29:381, 1999.

[12] L. B. Freund and S. Suresh. *Thin Film Materials.* Cambridge University Press, 2003.

[13] H. Ibach. *Surf. Sci. Rep.*, 29:195, 1997.

[14] J. H Park, L. H. Tjeng, J. W. Allen, P. Metcalf, and C. T. Chen. *Phys. Rev. B*, 55:12813, 1997.

[15] D. Schrupp, M. Sing, M. Tsunekawa, H. Fujiwara, S. Kasai, A. Sekiyama, S. Suga, T. Muro, V. A. M. Brabers, and R. Claessen. *Europhys. Lett.*, 70:789, 2005.

[16] K. Jordan, A. Cazacu, G. Manai, S. F. Ceballos, S. Murphy, and I. V. Shvets. *submitted to Phys. Rev. B.*

[17] F. Walz. *J. Phys.: Cond. Matter*, 14:R285, 2002.

[18] K. Balakrishnan, S. K. Arora, and I. V. Shvets. *J. Phys. Condens. Matter*, 16:5387, 2004.

[19] S. K. Arora, R. G. S. Sofin, and I. V. Shvets. *submitted to Journ. Appl. Phys.*

[20] R. M. Cornell and U. Schwertmann. *The Iron Oxides.* VCH Verlagsgesellschaft mbH, first edition, 1996.

[21] J. F. Gregg, I. Petej, E. Jouguelet, and C. Dennis. *J. Phys. D: Appl. Phys.*, 35:R121, 2002.

[22] F. Voogt. *Ph. D. Thesis.* Univeristy of Groningen, 1998.

[23] F. C. Voogt, T. Fujii, P. J. M. Smulders, L. Nielsen, and M. A. James ad T. Hibma. *Phys. Rev. B*, 60(15):11193, 1999.

[24] s. Kale, S. M. Bhagat, S. E. Lofland, T. Scabarozi, S. B. Ogale, A. Orozco, S. R. Shinde, T. Venkatesan, B. Hannoyer, B. Mercey, and W. Prellier. *Phys. Rev. B*, 64:205413, 2001.

[25] T. Kado. *Thin Solid Films*, 459:187, 2004.

[26] A. Bollero, M. Ziese, R. Höhne, H. C. Semmelhack, U. Köhler, A. Setzer, and P. Esquinazi. *J. of Magn. Magn. Mater.*, 285(1):279, 2005.

[27] C. A. Kleint, H. C. Semmelhack, M. Lorentz, and M. K. Krause. *I. Magn. Magn. Mater.*, 140:725, 1995.

[28] Y. V. Maksimov, M. V. Tsodikov, M. A. Perederii, O. V. Bukchtenko, I. P. Suzdalev, and J. A. Navio. *Surface and Interface Analysis*, 30(1):74, 2000.

[29] J. Wang, Z. Peng, Y. Huang, and Q. Chen. *J. Cryst. Growth*, 263:616, 2003.

[30] Z. Liu, D. Zhang, S. Han, C. Li, B. Lei, W. Lu, J. fang, and C. Zhou. *J. Am. Chem. Soc.*, 6:127, 2005.

[31] D. T. Margulies, F. T. Parker, M. L. Rudee, F. E. Spada, J. N. Chapman, P. R. Aitchison, and A. E. Berkovitz. *Phys. Rev. Lett.*, 79:5162, 1997.

[32] J. M. D. Coey, A. E. Berkowitz, Ll. Balcells, F. F. Putris, and F. T. Parker. *Appl. Phys. Lett.*, 72:734, 1998.

[33] W. Eerenstein, T. T. M. Palstra, T. Hibma, and S. Celotto. *Phys. Rev. B*, 66:201101(R), 2002.

[34] W. Eerenstein, T. T. M. Palstra, S. S. Saxena, and T. Hibma. *Phys. Rev. Lett.*, 88:247204, 2002.

[35] W. H. Bragg. *Phyl. Mag.*, 30:305, 1915.

[36] P. Weiss and R. Forrer. *J. Phys. Chem.*, 12:279, 1929.

[37] E. J. W. Verwey and P. W. Haayman. *Physica*, 8:979, 1941.

[38] E. J. W. Verwey, P. W. Haayman, and C. W. Romenijn. *J. Chem. Phys.*, 14:181, 1947.

[39] D. Khomskii. *Electronic Structure, Exchange and Magnetism in Oxides.* Springer-Verlag Berlin Heidelberg, 2001.

[40] G. S. Parks and K. K. Kelly. *J. Phys. Chem.*, 30:47, 1926.

[41] C. A. Domenicali. *Phys. Rev.*, 78(4):458, 1950.

[42] M. Iizumi, T. F. Koetzle, G. Shirane, S. Chikazumi, M. Matsui, and S. Todo. *Acta Cryst.*, B38:2121, 1982.

[43] W. C. Hamilton. *Phys. Rev.*, 110(5):1050, 1958.

[44] Jr L. R. Bickford. *Phys. Rev.*, 78:449, 1950.

[45] Jr L. R. Bickford. *Rev. Mod. Phys.*, 25(1):75, 1953.

[46] H. P. Rooksby and B. T. M. Willis. *Acta Cryst.*, 6:565, 1953.

[47] T. Yamada, K. Suzuki, and S. Chikazumi. *Appl. Phys. Lett.*, 13:172, 1968.

[48] K. Chiba, K. Suzuki, and S. Chikazumi. *J. Phys. soc. Jap. Lett.*, 39:839, 1975.

[49] G. T. Rado and J. M. Ferrari. *Phys. Rev. B*, 12:5166, 1975.

[50] G. T. Rado and J. M. Ferrari. *Phys. Rev. B*, 15:290, 1975.

[51] A. A. Hirsch and G. Galeczki. *J. Physique*, 40(C2):320, 1979.

[52] J. R. Cullen and E. R. Callen. *Phys. Rev. B*, 7:397, 1973.

[53] M. Matsui, S. Todo, and S. Chikazumi. *J. Phys. Soc. Jap.*, 42:1517, 1977.

[54] J. García and G. Subías. *J. Phys.: Cond. Matter*, 16:R145, 2004.

[55] G. Kh. Rozenberg, M. P. Pasternak, W. M. Xu, Y. Amiel, M. Hanfland, M. Amboage, R. D. Taylor, and R. Jeanloz. *Phys. Rev. Lett.*, 96:045705, 2006.

[56] S. Iida, K. Mizusuma, M. Mizoguchi, K. Kose, K. Kato, K. Yanai, N. Goto, and S. Yumoto. *J. Appl. Phys.*, 53:2164, 1982.

[57] M. Mizoguchi. *J. Phys. Soc. Jap.*, 44:1501, 1978.

[58] J. M .Zuo, J. C. H. Spence, and W. Petuskey. *Phys. Rev. B*, 42:8451, 1990.

[59] J. P. Wright, J. P. Attfield, and P. G. Radaelli. *Phys. Rev. B*, 66:214422, 2002.

[60] J. García, G. Subías, M. G. Proietti, J. Blasco, H. Renevier, J. L. Hodeau, and Y. Joly. *Phys. Rev. B*, 63:054110, 2001.

[61] G. Subías, J. García, J. Blasco, M. G. Proietti, H. Renevier, and M. C. Sanchez. *Phys. Rev. Lett.*, 93:156408, 2004.

[62] M. Mizoguchi. *J. Phys. Soc. Jap.*, 70(8):2333, 2001.

[63] S. F. Alvarado, M. Erbudak, and P. Munz. *Phys. Rev. B*, 14:2740, 1976.

[64] R. Lad and V. Henrich. *Phys. Rev. B*, 39(18):13478, 1989.

[65] Y. Dedkov, U. Rüdiger, and G. Güntherodt. *Phys. Rev. B*, 65:064417, 2002.

[66] M. Fonin, Y. Dedkov, J. Mayer, U. Rüdiger, and G. Güntherodt. *Phys. Rev.B*, 68:045414, 2003.

[67] M. Fonin, R. Pentcheva, Y. Dedkov, M. Sperlich, D. Vyalikh, M. Schffler, U. Rüdiger, and G. Güntherodt. *Phys. Rev. B*, 72:104436, 2005.

[68] http://www als.lbl.gov/als/compendium/AbstractManager/uploads/00046.pdf.

[69] G.Hu and Y. Suzuki. *Phys. Rev. Lett.*, 89:276601, 2002.

[70] F. C. Voogt, T. T. M. Palstra, L. Nielsen, O. C. Rogojanu, M. A. James, and T. Hibma. *Phys. Rev. B*, 57:R8107, 1998.

[71] S. Parkin, C. Kaiser, A. Panchula, A. Panchula, P. M. Rice, M. Samant, and S-H Yang. *Nature Materials*, 3:862, 2004.

[72] S. Celotto, W. Eerenstein, and T. Hibma. *Eur. Phys. J. B*, 36:271, 2003.

[73] W. Eerenstein. *Spin-Dependent Transport Across Anti-Phase Boundaries in Mangnetite Thin Films*. PhD thesis, Univeristy of Groningen, The Netherlands, 2003.

[74] W. Eerenstein, T. T. Palstra, T. Hibma, and S. Celotto. *Phys. Rev. B*, 68:014428, 2003.

[75] C. Julain Chen. *Introduction to Scanning Tunneling Microscopy*. Oxford University Press, New York, 1993.

[76] R. Wiesendanger. *Scanning Probe Microscopy and Spectroscopy*. Cambridge University Press, New York, 1994.

[77] Simmons. *J. Appl. Phys.*, 34:1793, 1963.

[78] Yuri P. Raizer and Iu P. Raizer. *Gas Discharge Physics*. Springer, New York, 1997.

[79] P. Hartmann, Z. Donkó, G. Bánó, L. Szalai, and K. Rózsa. *Plasma Sources Sci. Technol.*, 9:183, 2000.

[80] *Handbook of Cryogenic Engineering*. J. G. Weisend II, 1998.

[81] Guy K. White and Philip J. Meeson. *Experimental Techniques in Low Temperature Physics.* Oxford University Press, 2002.

[82] M. D'Angelo G. Mariotto and I. V. Shvets. *Rev. Sci. Instr.*, 70,9:3651, 1999.

[83] D. Mac Mathúna. *Surface studies of nanomagnetic systems.* Master thesis, Trinity College Dublin, 2002.

[84] Staveley Sensor Inc. http://www.staveleyndt.com/.

[85] Moscow State Steel and Russia Alloys Institute, Moscow.

[86] Lakeshore Cryotronics. www.lakeshore.com.

[87] D. Sander, A. Enders, and J. Kirschner. *Rev. Sci. Instrum.*, 66(9):4734, 1995.

[88] V. B. Braginsky and A. A. Samoilenko. *gr-qc*, v1:0304100, 2003.

[89] W. Fang, H. C. Tsai, and C. Y. Lo. *Sensors and Actuators*, 77:21, 1999.

[90] G. G. Stoney. *Proc. R. Soc. London Ser. A*, 82:172, 1909.

[91] P. H. Townsend, D. M. Barnet, and T. A. Brunner. *J.A.P.*, 62:4438, 1987.

[92] C. H. Hsueh and S. Lee. *Journ. Appl. Phys.*, 91(5):2760, 2002.

[93] C. H. Hsueh, S. Lee, and T. J. Chuang. *Journal of Applied Mechanichs*, 70:151, 2003.

[94] J. C. Vickerman. *Surface Analysis: The Principal techniques.* Wiley, New York, 1997.

[95] D. Briggs and M. P. Seah. *Pratical Surface ANanlysis: Ion and Neutral Spectroscopy.* Wiley, New York, 1992.

[96] M. A. Van Hove, V. H. Wienberg, and C. M. Chan. *Low-Energy Electron Diffraction*, volume 6. Springer Verlag, Berlin, Springer Series in Surface Science.

[97] G. Binning, H. Rohrer, Ch. Gerber, and E. Wiebel. *Phys. Rev. Lett.*, 49:57, 1982.

[98] J. Bardeen. *Phys. Rev. Lett.*, 6:57, 1961.

[99] J. A. Stroscio, R. M. Feenstra, and A. P. Fein. *Phys. Rev. Lett.*, 57(20):2579, 1986.

[100] N. D. Lang. *Phys. Rev. Lett.*, 34:5947, 1986.

[101] A. Quinn. *Developement of an Ultra-High Vacuum Scanning Tunneling Microscope.* PhD thesis, Trinity College Dublin, Ireland, 1996.

[102] J. Osing. *Studies towards spin sensitive scanning tunneling microscopy.* PhD thesis, Trinity College Dublin, Ireland, 1998.

[103] S. Murphy. *Surface Studies of the Fe/Mo(110) and Fe/W(100) Epitaxial Systems.* PhD thesis, Trinity College Dublin, Ireland, 2000.

[104] VAT Vacuum Products Ltd. 235 Regents Park Road, Finchley, London N3 3LG, UK.

[105] Physical Electronics Inc. (formerly Perkin-Elmer. 6509 Flying Cloud Drive, Eden.

[106] Vacuum Generators. Maunsell Road, Catleham Ind. Est. Hastings, East Sussex BN8 6SJ, UK.

[107] Pfeiffer Vacuum GmbH. Emmeliusstrasse, K-35614, Asslar Germany.

[108] Saes Getters G. B. Ltd. 5, Southern Court, South St. Reading, Berkshire RG1 4QS, UK.

[109] Omicron. Limberger Str. 75 D-65232 Taunusstein Germany.

[110] Leybold Inficon Inc. Two Technology Place, East Syracuse, NY 13057-9714 USA.

[111] Ciàran Seoighe. *Surface studies of magnetite (100).* PhD thesis, Trinity College Dublin, Ireland, 1999.

[112] IRCON Inc. 7301 Norh Caldwell Av. Niles, Illinois 60648, USA.

[113] PSP Vacuum Technology. Macclesfield SK11 OLR, UK.

[114] Physical Electronic Inc. (formerly Perkin-Elmer). 6509 Flying Cloud Drive, Eden.

[115] D. P. Woodroof and T. A. Delchar. *Mopdern Techniques of Surface Science.* Cambridge Solid State Series. Cambridge University Press, second edition, 1994.

[116] Stanford Research Systems. 1290-D REamwood Av., Sunnyvale, Caifornia 94089, USA.

[117] Thermo Vacuum Generators. Maunsell Road, Catleham Ind. Est. Hasting TN38 9NN, England.

[118] S. H. Pan. Piezo Electric Motor. International Patent Publication No WO93/19194. International Bureau, World Intellectual Property Organisation.

[119] Nanotec Electronica. Padilla, 3 1. D 28006-Mardid, Spain.

[120] R. Wiesendanger, I. V. Shvets, D. Bürgler, G. Tarrach, H. J. Güntherodt, J. M. D. Coey, and S. Gräser. *Science*, 255:583, 1992.

[121] A. A. Minakov and I. V. Shvets. *Surf. Sci.*, 236:L377, 1990.

[122] S. F. Ceballos, G. Mariotto, S. Murphy, and I. V. Shvets. *Surf. Sci.*, 523:131, 2003.

[123] H. Bourque and R. M. Leblanc. *Rev. Sci. Instrum.*, 66:2695, 1995.

[124] M. Seo, J. B. Lumsden, and R. W. Staehle. *Surf. Sci.*, 50:541, 1975.

[125] Y. Dedkov, M. Fonin, D. V. Vyalikh, J. O. Hauch, S. L. Molodtsov, U. Rüdiger, and G. Güntherodt. *Phys. Rev. B*, 70:073405, 2004.

[126] J. M. D. Coey, I. V. Shvets, R. Wiesendanger, H. J. Güntherodt, and S. Gräser. *J. Appl. Phys*, 73:6742, 1993.

[127] G. Tarrach, D. Bürgler, T. Schaub, R. Wiesendanger, and H. J. Güntherodt. *Surf. Sci.*, 285:1, 1993.

[128] G. Mariotto, S. Murphy, and I. V. Shvets. *Phys. Rev. B*, 66:245426, 2002.

[129] G. Mariotto. *Surface Reconstruction of $Fe_3O_4(001)$*. Ph. D. Thesis, Trinity College Dublin, 2001.

[130] K. Jordan. *Surface Studies of $Fe_3O_4(001)$, $Fe/Ge(001)$ and $Fe_3O_4(001)/Ge(001)$*. Ph. D. Thesis, Trinity College Dublin, 2005.

[131] Y. Oda, S. Mizuno, S. Todo, E. Torikai, and K. Hayakawa. *Jpn. J. Appl. Phys.*, 37:4518, 1998.

[132] P. W. Tasker. *J. Phys. C. Solid State Phys.*, 12:4977, 1979.

[133] C. Noguera. *J. Phys. C. Solid State Phys.*, 12(31):367, 2000.

[134] V. E. Henrich and P. A. Cox. *The Surface Science of Metal Oxides*. Cambridge University Press, Elsevier Science Publisher B. V., 1994.

[135] M. D. Pashley. *Phys. Rev. B*, 40(15):10481, 1989.

[136] J. P. LaFemina. *Crit. Rev. in Surf. Chem.*, 3(3/4):297, 1994.

[137] R. Jansen, B. J. Neilssen, D. J. Abraham, and H. van Kempen. *IEEE Transaction Magnetics*, 30(6):4506, 1994.

[138] R. Jansen, V. A. Brabers, and H. van Kempen. *Surf. Sci.*, 328:237, 1995.

[139] R. Jansen, H. van Kempen, and R. M. Wolf. *J. Vac. Sci. Tech. B*, 14(2):1173, 1996.

[140] G. Maris, L. Jdira anf J. H. H. Hemrsen, S. Murphy, G. Manai, I. V. Shvets, and S. Speller. *J. Phys. Soc. Jpn.*, 45:3B, 2006.

[141] P. K. Boer and R. A. Groot. *J. Phys. Condens. Matter*, 10:10241, 1998.

[142] R. Aragon, R. J. Rasmussen, J. P. Shepherd, J. W. Koenitzer, and J. M. Honig. *J. Magn. Magn. Mater*, 1335:47, 1986.

[143] B. Stanka, W. Hebnstreit, U. Diebolb, and S. A. Chambers. *Surf. Sci.*, 448:49, 2000.

[144] M. G. Ramsey and G. J. Russel. *Phys. Rev. B*, 30(12):6960, 1984.

[145] V. S. Smentkowsky and Jr. J. T. Yates. *Surf. Sci.*, 232:113, 1990.

[146] H. des Daas, O. L. J. Gijzeman, and J. W. Geus. *Surf. Sci.*, 290:26, 1993.

[147] J. Y. T. Wey, N. C. Yeh, R. P. Vasquez, and A. Gupta. *J. Appl. Phys.*, 83(11):7366, 1998.

[148] MTI Corporation. www.fiberopticsonline.com/storefronts/mticorp.html 5327, Jacuzzi St., Building 3H, Richmond, California 94804, US.

[149] J. Anderson, M. Kuhn, U. Diebold, K. Shaw, P. Stoyanov, and D. Lind. *Phys. Rev. B*, 56:9902, 1997.

[150] Y. Gao and S. A. Chambers. *J. Cryst. Growth*, 174:446, 1997.

[151] M. Ciria, J. I. Amadeus, A. del Moral, G. J. Tomka, C. de la Fuente, P. A. J. de Groot, M. R. Wells, and R. C. C. Ward. *Phys. Rev. Lett.*, 75(8):1634, 1995.